Department of Physics
Doctoral Programme In Physics

Photonic Integrated Devices via Femtosecond Laser Micromachining for Quantum Applications

Doctoral Dissertation of:
Giulio Gualandi

Supervisor:
Dr. Giacomo Corrielli

Tutor:
Prof. Andrea Crespi

The Chair of the Doctoral Program:
Prof. Salvatore Stagira

2022-2025 – XXXVIII Cycle

Abstract

The advent of quantum technologies is expected to revolutionize the way information is processed and transmitted. Unlike classical approaches, they exploit the ability to prepare and manipulate genuine quantum states, where phenomena such as entanglement and superposition provide powerful resources for solving problems beyond the reach of classical algorithms. Furthermore, the use of quantum carriers enables intrinsically secure communication and unprecedented sensitivity in probing the physical world. Photons are particularly well suited for this purpose: they are robust carriers of quantum information and, combined with recent progress in integrated optics, support the development of compact and stable platforms for quantum experiments. A major challenge, however, remains the scalability of quantum technologies, which is essential for moving beyond laboratory demonstrations toward widespread deployment. While some applications, such as quantum communication, have already reached the stage of real-world implementation, others are still progressing through intermediate steps that serve as milestones toward large-scale, fault-tolerant systems. Addressing these challenges, research in quantum photonics aims both to enable practical applications and to provide the building blocks for future quantum technologies. In this thesis, we investigate femtosecond laser micromachining as a versatile technique for fabricating integrated photonic devices in glass. This

method allows the rapid prototyping of three-dimensional circuits, allowing the fabrication of photonic components such as waveguides, tunable interferometers, and resonators, without the need for clean-room facilities. The fabricated structures exhibit low propagation losses and can be efficiently interfaced with other optical components. The devices developed in this work cover a broad spectrum of applications in quantum photonics. They include circuits for quantum communication, compact systems for quantum information processing, a source for heralded Bell states, and the implementation of a tunable ring resonator. Together, these results represent concrete steps toward the advancement of photonic quantum technologies.

Contents

Abstract I

List of Figures X

List of Tables XII

I Background 1

1 Integrated quantum photonics 3

1.1 Qubit 4

1.1.1 Photons as qubit 7

1.2 Quantum technologies 8

1.2.1 Quantum computing 9

1.2.2 Quantum communication 10

1.2.3 Quantum metrology 11

1.3 Fundamentals of photonic waveguides 12

1.3.1 Optical waveguide 12

1.3.2 Coupled mode theory 14

2 Femtosecond Laser Micromachining 19

2.1 Femtosecond laser interaction with transparent material 21

2.1.1 Free-electron plasma formation 21
2.1.2 Thermal relaxation and material modification 23
2.2 Waveguide writing parameters 24
2.2.1 Focusing 24
2.2.2 Repetition Rate 25
2.2.3 Writing Geometry 26
2.2.4 Other Parameters 26
2.3 Quantum photonics components with FLM 27
2.3.1 Directional Coupler 29
2.3.2 Mach-Zehnder interferometer 29
2.3.3 Reconfigurability 30
2.4 Comparison with other integrated photonics platforms 32
2.4.1 Silica on silicon 33
2.4.2 Silicon on insulator 33
2.4.3 Silicon nitride 35
2.4.4 Thin-film lithium niobate 35

II Experimental **37**

3 Materials and Methods **39**
3.1 Fabrication of the device 39
3.1.1 Femtosecond laser inscription 41
3.1.2 Post-inscription processes 43
3.1.3 Fabrication of the thermo-optic phase shifters 45
3.1.4 Packaging 48
3.2 Characterization methods 49
3.2.1 Microscope inspection 49
3.2.2 Light coupling 50
3.2.3 Insertion Losses 52
3.2.4 Polarization and birefringence 56
3.2.5 Directional coupler characterization 58
3.2.6 Reconfigurability 60

4 Photonics devices for secure communication systems **63**

4.1 Integrated Time-bin receiver for high-speed integrated QKD system . . . 64
4.1.1 Motivation . . . 64
4.1.2 One-Decoy Three-State BB84 Protocol . . . 65
4.1.3 Design of the time-bin QKD receiver . . . 67
4.1.4 Unbalanced MZI visibility . . . 69
4.1.5 Tuning of birefringence . . . 72
4.1.6 Fabrication and characterization of the device . . . 73
4.1.7 Conclusions and future perspectives . . . 79
4.2 Heterodyne receiver for quantum information processing . . . 80
4.2.1 Motivation . . . 80
4.2.2 Design and fabrication of the circuit . . . 81
4.2.3 Conclusions and future perspectives . . . 83

5 Scalable photonic system for quantum information processing 85
5.1 Direct coupling of a laser-written PIC to a SPAD array . . . 86
5.1.1 Motivation . . . 86
5.1.2 Design and fabrication of the PIC . . . 87
5.1.3 Experimental setup and data acquisition . . . 89
5.1.4 Validation of the PIC–SPAD coupling . . . 91
5.1.5 Conclusions and future perspectives . . . 96
5.2 Reconfigurable Integrated photonic chip to test Born's rule . . . 97
5.2.1 Motivation . . . 97
5.2.2 Testing Born's rule with multi-path interferometry . . . 98
5.2.3 Design and fabrication of the three-arm interferometer . 99
5.2.4 Validation of the device . . . 103
5.2.5 Conclusions and future perspectives . . . 111

6 Photonic integrated circuit for heralded Bell's state generation 113
6.1 Motivation . . . 114
6.2 Preparation of heralded Bell states on photonic integrated circuits 115
6.3 Chip layout and working principle . . . 116
6.4 Chip fabrication and characterization . . . 120
6.4.1 Optical circuit and TOPS . . . 120
6.4.2 P2P converter . . . 121

6.5 Experimental setup 123
6.5.1 Quantum dot and demultiplexing stage 125
6.5.2 PIC and tomography setup 127
6.6 Conclusions and future perspectives 127

7 Tunable ring resonator via Femtosecond Laser Micromachining 129
7.1 Motivation 129
7.2 Design and fabrication 131
7.2.1 Chip layout 131
7.2.2 Chip fabrication 131
7.3 Modeling of single waveguide resonator 134
7.3.1 The coupled-resonator transfer function 137
7.3.2 Coupling matrix for the MZI 138
7.4 Results 139
7.4.1 Device characterization 140
7.4.2 Tunability of Q factor and resonance shift 143
7.5 Conclusions and future perspectives 145

8 Conclusions 147

Publications and Conferences 149

Ringraziamenti 151

Bibliography 153

List of Figures

1.1 Representation of a qubit on the Bloch sphere. 5
1.2 Sinusoidal power transfer between two adjacent waveguides. . 16

2.1 Mechanisms providing seed electrons for plasma generation. . 22
2.2 Thermal phase shifters on FLM waveguides with deep trenches or bridge-like structures to reduce cross-talk and power consumption. 31

3.1 Schematic of the FLM setup. 40
3.2 Micrographs of the waveguides before (**a**) and after (**b**) annealing. Image taken from [1]. 44
3.3 Pigtailing setup with hexapods for alignment and device after fiber attachment. 49
3.4 Main configurations for waveguide characterization. 50
3.5 Schematic representation of a directional coupler. 58
3.6 Schematic of a reconfigurable MZI and corresponding bar-port transmission modulation. 60

4.1 Time-bin QKD: state encoding by Alice and measurement by Bob, and schematic of the experimental setup. 66
4.2 Scheme of the time-bin QKD receiver. 67

4.3 Microphotograph of the stress track. 73
4.4 Waveguide and directional coupler optimization: insertion losses of straight and U-bend waveguides, and normalized bar transmission of the DC. 74
4.5 Insertion losses of a waveguide with underlying stress tracks. . 76
4.6 Photograph of the fully assembled DC-QKD device. 79
4.7 Schematic layout of the FLM-fabricated CV-QRNG and CV-QKD device highlighting mode-mixing, thermal phase shifter, and reconfigurable beam splitters. 81

5.1 Waveguide layout and reconfigurable PIC coupled to the SPAD array, with TOPSs highlighted. 87
5.2 Micrographs of the TOPSs on the reconfigurable MZI and the 8×8 SPAD array with selected detectors highlighted. 89
5.3 Schematic of the optical setup coupling a laser to the PIC and SPAD array, including attenuation and monitoring paths. . . . 90
5.4 Photographs of the automated PIC–SPAD coupling setup from different perspectives. 91
5.5 **a**, **b** Linearity measurements of SPAD 1 and SPAD 4, acquired at different laser intensities. **c** Photon detection efficiency (PDE) as a function of the overvoltage. 91
5.6 PDE maps and profiles for SPAD 1 and SPAD 4, including distance dependence and comparison with simulations. 93
5.7 Normalized output powers, SPAD vs. powermeter comparison, and optical cross-talk measurements. 95
5.8 Layout of Born's chip highlighting the three-arm interferometer, directional couplers, MZIs, and TOPSs controlling the optical paths. 100
5.9 Vertical coupler realized with 3D FLM: side view, transmission vs. interaction distance, and section micrograph. 102
5.10 Micrographs of the TOPS and trenches, and photograph of the fully assembled device. 103
5.11 Extinction ratio measured for MZI 1, MZI 2, and MZI 3. . . . 104

5.12 MZI transmission versus heater current and crosstalk mapping using the normalized $\hat{\beta}$ matrix. 107
5.13 Transmission of MZIs 1–3 for each switch configuration, showing high extinction ratio after calibration. 108
5.14 Phase-space map of the three-arm interferometer showing output intensity and the optimal operating point. 108
5.15 Calibration curves of the three-arm interferometer for the three two-arm interference configurations, showing output intensity versus heater current squared. 109
5.16 Normalized three-path interference term $\kappa^{(3)}$ measured over 100 consecutive repetitions, showing mean and standard deviation. 110

6.1 Scheme of Bell-state generation with qubit outputs, heralding channels, and a phase-controlling TOPS. 117
6.2 Layout of the fully assembled device showing the integrated circuit and the path-to-polarization converter. 119
6.3 Spatial mode characterization of the two P2P modules, showing outputs for different input qubit pairs and their overlap. . . 123
6.4 Schematic of the experimental setup with source/demultiplexer, PIC for heralded entanglement, and state tomography stage. 124
6.5 Schematic of the source and demultiplexer stage producing four spatially separated photons. 125

7.1 Layout of the resonator showing the racetrack waveguide, MZI with TOPSs, and U-trenches. 132
7.2 Two concentric resonators illustrating the geometry for multi-resonator fabrication. 133
7.3 Micrographs of Cr+Au resistors and contact pads, and photograph of the fully assembled device. 134
7.4 Schematic of the FLM racetrack resonator with a reconfigurable MZI controlling coupling between waveguide and ring. 135
7.5 Spectral characterization of the resonator: resonance dips, zoomed fringe details, and transmission versus coupling tuning. 140

7.6 Characterization of resonators versus ring radius: round-trip losses, FSR compared to theory, and quality factor at critical coupling. 141
7.7 Q factor versus dissipated power P_1, showing the transition from overcoupling to undercoupling and highlighting the maximum Q in the undercoupled regime. 143
7.8 Resonance shift versus dissipated power P_2, showing a linear trend with linear fit. 144

List of Tables

4.1 Measured birefringence and phase before and after stress track inscription. Waveguide 1 corresponds to a 1 cm track, while Waveguide 2 corresponds to a 2 cm track. For each case, the effect of bottom and top tracks is reported separately. 77

4.2 Measured visibility before and after stress-track inscription entering with polarized light at 45°. Values in brackets indicate the estimated phase-compensation degree. 78

4.3 Inscription parameters for low-loss, single-mode waveguides at 1550 nm. The inset shows the waveguide mode profile. Scalebar is 5 μm. 82

4.4 FLM-written PIC specifications. Summary of insertion losses for IN1 and IN2 (see Fig. 4.7), reflectivity of the directional couplers for horizontal (H) and vertical (V) polarization, and electrical power required to induce a 2π phase shift. 83

4.5 Comparison of commercial and PIC-based hybrid devices . . 84

5.1 Inscription settings yielding low-loss, single-mode waveguides at 561 nm. Inset: guided mode of the waveguide. Scalebar is 3 μm. 89

5.2 Comparison with state-of-the-art photonic detector technologies. 96

6.1 Inscription parameters for the fabrication of the photonic chip. 120

7.1 Inscription parameters for low-loss, single-mode waveguides at 1550 nm for the integrated ring resonator. In the inset a microscope image of the cross-section of the waveguide. The scalebar corresponds to 30 μm. 131

Part I

Background

CHAPTER 1

Integrated quantum photonics

The works presented in this thesis are ultimately aimed at enabling future quantum technologies. To this end, this chapter introduces their context and underlying principles. I begin by presenting the concept of the qubit, the fundamental unit of quantum information, and then focus on how photons can serve as its physical realization. Next, I discuss the main quantum technologies that motivate the development of the integrated photonic devices described in this thesis. Finally, I provide an overview of the fundamental principles of photonic waveguides, which constitute the basic building blocks of integrated circuits. Throughout the chapter, I emphasize the integrated approach, as it uniquely offers the compactness, scalability, and stability required to advance quantum photonics from proof-of-principle demonstrations to practical technologies.

1.1 Qubit

The essential unit of quantum information is the quantum bit, or qubit. Unlike a classical bit, which can exist only in one of the two states 0 or 1, a qubit can occupy a coherent superposition of both basis states, usually denoted as $|0\rangle$ and $|1\rangle$ [2]. Mathematically, a generic pure qubit state can be written as

$$|\psi\rangle = \alpha\,|0\rangle + \beta\,|1\rangle\,, \qquad \alpha, \beta \in \mathbb{C}, \quad |\alpha|^2 + |\beta|^2 = 1. \tag{1.1}$$

The complex coefficients α and β are probability amplitudes. The probabilities of obtaining the outcomes $|0\rangle$ or $|1\rangle$ upon measurement are given by $|\alpha|^2$ and $|\beta|^2$, respectively. This probabilistic behavior is at the heart of the power of quantum information.

As illustrated in Fig. 1.1, the Bloch sphere provides a convenient way to represent a qubit state. By writing $\alpha = \cos(\theta/2)$ and $\beta = e^{i\phi}\sin(\theta/2)$, any pure state can be visualized as a point on the surface of a unit sphere parameterized by the polar and azimuthal angles θ and ϕ. The north and south poles correspond to the computational basis states $|0\rangle$ and $|1\rangle$, respectively, whereas all other points describe coherent superpositions of these two states. In particular, equal superpositions, such as $(|0\rangle + |1\rangle)/\sqrt{2}$, lie along the equator. Within this representation, the action of a single-qubit quantum gate corresponds to a rotation of the state vector on the Bloch sphere, implemented by a unitary operation [3]. For example, the Pauli-X gate (or NOT gate) flips the logical states $|0\rangle$ and $|1\rangle$, and is represented by the matrix

$$X = \begin{pmatrix} 0 & 1 \\ 1 & 0 \end{pmatrix}. \tag{1.2}$$

The Hadamard gate, on the other hand, creates a superposition from a computational basis state and is defined as [4]

$$H = \frac{1}{\sqrt{2}} \begin{pmatrix} 1 & 1 \\ 1 & -1 \end{pmatrix}. \tag{1.3}$$

In order to achieve universal quantum computation, however, single-qubit

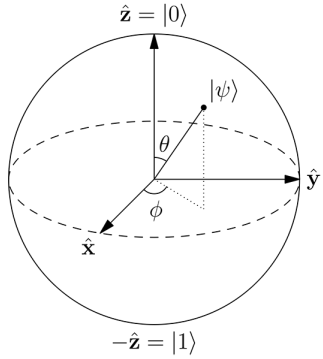

Figure 1.1: *Representation of a qubit by a Bloch sphere.Any pure state $|\psi\rangle$ can be visualized as a point on the surface of the sphere, defined by the polar angle θ and the azimuthal angle ϕ. The north and south poles correspond to the computational basis states $|0\rangle$ and $|1\rangle$, respectively, while all other points represent superpositions of these two states.*

gates are not sufficient: at least one two-qubit gate is also required, allowing for the implementation of conditional operations [2]. A well-known example is the controlled-NOT (CNOT) gate, which flips the target qubit if and only if the control qubit is in the state $|1\rangle$:

$$\text{CNOT} = \begin{pmatrix} 1 & 0 & 0 & 0 \\ 0 & 1 & 0 & 0 \\ 0 & 0 & 0 & 1 \\ 0 & 0 & 1 & 0 \end{pmatrix}. \tag{1.4}$$

An example of a universal gate set is composed of the rotation operators $R_x(\theta)$, $R_y(\theta)$, $R_z(\theta)$, the phase-shift gate $P(\phi)$, and the CNOT gate.

However, the power of quantum computation does not rely solely on superposition, but also on another uniquely quantum phenomenon: entanglement [2]. Entanglement enables correlations between qubits that have no classical counterpart and plays a central role in quantum information processing. Entanglement arises when two or more qubits are correlated in such a way that their joint quantum state cannot be factorized into individual states. In this case, the state of one qubit cannot be described independently of the state of the others, even when the qubits are spatially separated. This intrinsi-

cally nonlocal property represents a fundamental resource for both quantum communication and quantum computation. Thanks to entanglement, it is possible to implement protocols that would be impossible with classical correlations alone. A paradigmatic example is quantum teleportation, where the state of an unknown qubit can be faithfully transferred from one location to another by exploiting shared entanglement and the exchange of classical information. Similarly, entanglement enables superdense coding [5], in which two classical bits of information can be transmitted by sending only a single qubit, and forms the basis of entanglement-based quantum key distribution schemes such as the Ekert protocol [6]. In the context of quantum computation, entanglement is also essential for creating correlations across different qubits, which allow quantum algorithms to achieve exponential speed-ups over their classical counterparts [7].

The physical implementation of a qubit requires the fulfillment of several requirements. These were formalized by David DiVincenzo in 2000 in what are now known as the DiVincenzo's criteria [8]. According to these guidelines, a physical qubit must:

1. be well-defined as a two-level quantum system and scalable to many qubits,

2. allow reliable initialization to a known reference state,

3. exhibit coherence times long enough to complete the computation,

4. support a universal set of gates, including both single-qubit rotations and entangling two-qubit operations,

5. be measurable with high fidelity.

These criteria, while seemingly straightforward, are notoriously difficult to satisfy simultaneously, and they provide a roadmap for evaluating the various quantum hardware platforms.

Several physical systems have been explored for qubit implementations. Among the most advanced are superconducting qubits [9], trapped ions [10],

semiconductor quantum dots [11], neutral atoms [12], spin qubits in solid-state systems [13] and photons [14]; each with its own trade-offs between coherence, controllability, and integration potential.

1.1.1 Photons as qubit

Among the various candidates, photons occupy a particularly unique position. Thanks to their weak interaction with the environment, photons offer exceptional robustness against decoherence, making them ideal carriers of quantum information across long distances. In addition, photons are relatively easy to generate, manipulate, and detect using well-established optical components such as directional couplers and phase shifters, which makes them particularly convenient for the realization of quantum protocols. A further advantage lies in the fact that photonic integrated circuits can be fully characterized with classical light, allowing one to optimize and test devices without the need for single-photon sources. This greatly simplifies the development and validation of photonic platforms for quantum technologies.

A key advantage of photons is the flexibility in the choice of the logical basis, since multiple encoding schemes can be employed to define a two-level system [15]. The most common encodings include:

- **Polarization encoding**, where the logical states are associated to two orthogonal polarization modes, e.g. $|H\rangle$ and $|V\rangle$ [16].
- **Path (dual-rail) encoding**, in which a single photon is distributed over two spatial modes or waveguides, with $|0\rangle$ corresponding to the photon being in one path and $|1\rangle$ in the other [14].
- **Time-bin encoding**, where the qubit states are defined by the photon arrival time in two well-separated temporal bins, commonly referred to as “early” and “late” [17].
- **Frequency-bin encoding**, where logical states are associated with photons at two distinct optical frequencies [18].

Each encoding has specific advantages and challenges: polarization is natural in free-space experiments but suffers from drifts in fiber; time-bin

is particularly robust for long-distance fiber communication; path encoding, instead, is intrinsically compatible with integrated photonics and therefore widely used in on-chip implementations.

On the other hand, the very same weak interaction that protects photons from decoherence poses challenges for realizing deterministic two-qubit gates, which typically rely on nonlinear interactions [19] or probabilistic schemes involving measurement [14]. Nevertheless, photons are especially well suited to applications in quantum communication and, more generally, to any context where information needs to be transmitted or processed in a low-noise environment. Furthermore, the availability of multiple encoding schemes and their interconversion in integrated circuits strengthens the role of photons in quantum technologies. Depending on the application, one can choose the most suitable encoding, while hybrid approaches further increase flexibility. This versatility also supports scalability, enabling modular architectures where, for example, information is processed on-chip in dual-rail encoding, transmitted through fiber using polarization or time-bin encoding, and then interfaced with another chip for further operations [20, 21]. In this way, integrated photonics offers a unique platform to build compact, stable, and scalable quantum technologies [22].

1.2 Quantum technologies

The development of quantum technologies is often contextualized by distinguishing two major "quantum revolutions" [23]. The first quantum revolution took place in the early 20th century, when the principles of quantum mechanics were established. This period was characterized by groundbreaking discoveries such as wave-particle duality, quantization of energy levels, and the uncertainty principle, which provided a radically new description of nature at the microscopic scale. These discoveries not only reshaped our understanding of physics but also enabled the invention of devices such as the transistor, the laser, and the semiconductor industry, which underpin today's information society.

The second quantum revolution, currently underway, builds on these fundamental concepts and exploits quantum phenomena as resources to develop

disruptive technologies. In this context, uniquely quantum properties such as superposition and entanglement are harnessed to process, transmit, and secure information in ways that are impossible within classical physics. This shift marks the transition from studying quantum mechanics as a scientific theory to engineering quantum systems for practical applications. The most prominent areas of this revolution are quantum computing [24], quantum communication [25] and quantum metrology [26], each of which leverages different aspects of quantum physics to unlock new functionalities and performance levels.

1.2.1 Quantum computing

The first proposals for photonic quantum computing were inspired by the gate-based model, in direct analogy with classical digital computation. In this paradigm, single-qubit and two-qubit gates are combined into circuits that implement arbitrary unitary transformations. Photons, however, interact only very weakly with one another, which makes the realization of deterministic two-qubit gates extremely challenging. Nonlinear optical effects such as the Kerr nonlinearity are far too small at the single-photon level, rendering direct gate-based approaches impractical [27–29]. A major breakthrough was achieved with the work of Knill, Laflamme, and Milburn (KLM) [14], who demonstrated that efficient quantum computing is, in principle, possible using only linear optical components (beam splitters and phase shifters), single-photon sources, and single-photon detectors. In their proof-of-principle scheme, two-qubit gates are realized probabilistically by exploiting entanglement and projective measurements, effectively transferring the nonlinearity to the measurement stage. While conceptually groundbreaking, the KLM result still required extremely large resources and phase stability, which limited its scalability. Nevertheless, it was a decisive step forward, showing that quantum computing with photons was feasible and opening the door to more practical approaches. Building on this idea, measurement-based quantum computing (MBQC) was developed [30], where computation proceeds by performing adaptive measurements on a highly entangled resource state, known as a cluster state. In this paradigm, the desired algorithm is encoded in the measurement pattern, rather than in the unitary gates of a circuit. Al-

though powerful in theory, MBQC faces the practical challenge of generating large cluster states with high fidelity, which remains experimentally demanding. A promising refinement of this idea is fusion-based quantum computing (FBQC) [31, 32], where large entangled resource states are constructed step by step by fusing together smaller entangled states using linear optics and photon detection. This modular approach not only makes the generation of large-scale cluster states more feasible, but also provides a natural framework for implementing quantum error correction, a key ingredient for fault-tolerant quantum computation [33–35]. For these reasons, fusion-based schemes are today considered one of the most promising routes toward building practical and scalable photonic quantum computers [36].

1.2.2 Quantum communication

As mentioned before, photons are the natural carriers of quantum information, as they can propagate over long distances in optical fibers or through free-space channels with minimal decoherence. A central application is Quantum Key Distribution (QKD) [21], which enables two parties to establish a shared secret key with security guaranteed by the laws of physics. The first and most widely known protocol is BB84, proposed by Bennett and Brassard in 1984 [37]. In BB84, quantum states are prepared in one of two mutually unbiased bases (e.g., linear $\{|H\rangle, |V\rangle\}$ and diagonal $\{|+\rangle, |-\rangle\}$ polarization states). The sender (Alice) encodes each bit in a randomly chosen basis, while the receiver (Bob) measures in a randomly chosen basis as well. After transmission, Alice and Bob publicly compare their chosen bases and keep only the cases where they match. The security arises from the fact that any eavesdropper (Eve) attempting to measure the qubits necessarily introduces detectable errors, due to the no-cloning theorem [38] and the incompatibility of non-orthogonal states.

Another seminal protocol is Ekert's scheme (E91) [6], which instead exploits entanglement. In this approach, entangled photon pairs are distributed between Alice and Bob. Each party measures their photon in randomly chosen bases, and the correlations between their outcomes are then analyzed. If the measured correlations violate a Bell inequality [39], they demonstrate the presence of genuine quantum entanglement and guarantee the security of the

key distribution. In this way, security is certified by the fundamental nonlocality of quantum mechanics, rather than by assumptions about the devices used.

An additional key ingredient for quantum communication is the availability of high-quality Quantum Random Number Generators (QRNGs) [40, 41]. Randomness is a fundamental resource in cryptography: it is required for choosing the quantum states to be transmitted, for selecting measurement bases, and for post-processing steps such as error correction. Classical pseudo-random number generators, based on deterministic algorithms, cannot provide the level of unpredictability needed for unconditional security. In contrast, QRNGs exploit the intrinsic indeterminism of quantum measurements, for instance, the detection of single photons after a balanced beam splitter [40], or the fluctuations of the vacuum field in continuous-variable implementations [42]. Thanks to their relatively easy implementation, QRNGs have become one of the most mature quantum technologies and have already reached commercialization.

Beyond these protocols, other important developments include quantum teleportation [43], entanglement swapping [44], and the development of quantum repeaters [45], all aimed at extending communication distances and laying the foundation for a future quantum internet [46].

1.2.3 Quantum metrology

Another important branch of quantum technologies is quantum metrology, which aims at exploiting quantum resources to enhance the precision of measurements beyond the limits achievable with classical strategies. In conventional interferometry, the sensitivity in estimating a parameter, such as a phase shift, scales as $1/\sqrt{N}$, where N is the number of photons employed, a limit known as the standard quantum limit. By using quantum states of light, such as entangled or squeezed states, it is possible to surpass this scaling and approach the ultimate bound imposed by quantum mechanics, the Heisenberg limit, which scales as $1/N$ [47]. Quantum metrology has a wide range of potential applications, from gravitational wave detection [48] to spectroscopy [49] and biomedical imaging [50].

1.3 Fundamentals of photonic waveguides

Two key phenomena underpin the operation of integrated photonic circuits: light confinement within waveguides and mode coupling between adjacent channels. These mechanisms govern the guiding properties of individual structures and enable the implementation of functional components such as directional couplers, and consequently, linear interferometers. A clear understanding of waveguide theory and coupling models is therefore crucial for the accurate design and characterization of integrated circuits.

1.3.1 Optical waveguide

An optical waveguide is a structure engineered to confine and guide light along a preferred direction through refractive index contrast and electromagnetic boundary conditions. In the simplest and most common configuration, it consists of a core of refractive index n_1 embedded in a cladding with index n_2, with $n_1 > n_2$ so that total internal reflection occurs at the core-cladding interface. Under this condition, electromagnetic waves are bound to the core and can propagate along the guide axis [51, 52].

In a linear, isotropic, source-free and non-magnetic dielectric medium, the propagation of electromagnetic fields is governed by Maxwell's equations, which in terms of the electric and magnetic fields $\mathbf{E}(\mathbf{r}, t)$ and $\mathbf{H}(\mathbf{r}, t)$ read

$$\nabla \times \mathbf{E}(\mathbf{r}, t) = -\mu_0 \frac{\partial \mathbf{H}(\mathbf{r}, t)}{\partial t}, \tag{1.5a}$$

$$\nabla \times \mathbf{H}(\mathbf{r}, t) = \epsilon(\mathbf{r}) \frac{\partial \mathbf{E}(\mathbf{r}, t)}{\partial t}, \tag{1.5b}$$

$$\nabla \cdot \Big(\epsilon(\mathbf{r})\mathbf{E}(\mathbf{r}, t)\Big) = 0, \tag{1.5c}$$

$$\nabla \cdot \mathbf{H}(\mathbf{r}, t) = 0. \tag{1.5d}$$

with $\epsilon(\mathbf{r}) = \epsilon_0 n^2(\mathbf{r})$, assuming $\mu_r = 1$. By combining the curl equations and eliminating the magnetic field, one obtains the vector wave equation for the electric field

$$\nabla^2 \mathbf{E}(\mathbf{r}, t) = \frac{n^2(\mathbf{r})}{c^2} \frac{\partial^2 \mathbf{E}(\mathbf{r}, t)}{\partial t^2}, \tag{1.6}$$

with $c = 1/\sqrt{\mu_0 \epsilon_0}$ the speed of light in vacuum. For a guided monochromatic solution, the field can be written as

$$\mathbf{E}(\mathbf{r}, t) = \mathbf{e}(x, y)\, e^{\,i(\beta z - \omega t)}, \tag{1.7}$$

where $\mathbf{e}(x, y)$ is the transverse mode profile, β is the propagation constant along z, and ω the angular frequency. Substituting this ansatz into Eq. (1.6) yields the Helmholtz equation:

$$\nabla^2 \mathbf{E}(\mathbf{r}) + k_0^2 n^2(\mathbf{r}) \mathbf{E}(\mathbf{r}) = 0, \tag{1.8}$$

with $k_0 = \omega/c$ the free-space wavenumber.

Equation (1.8) is general: it describes the spatial distribution of fields in any dielectric profile $n(\mathbf{r})$. The actual solutions depend on geometry and boundary conditions. In a homogeneous medium with constant n, Eq. (1.8) admits plane-wave solutions with $\beta = nk_0$; in stratified media it yields reflected and transmitted modes at interfaces; and in confined geometries such as optical fibers or integrated waveguides, it produces a discrete set of guided modes with distinct propagation constants β [53].

A paradigmatic case is the step-index circular waveguide, consisting of a core of radius a and index n_1, surrounded by a cladding of index $n_2 < n_1$. In cylindrical coordinates, the longitudinal field components satisfy Bessel-type equations, yielding oscillatory solutions within the core and exponentially decaying ones in the cladding.

$$\begin{aligned} r < a: &\quad E_z, H_z \propto J_\ell\left(\tfrac{ur}{a}\right) e^{i\ell\phi}, \\ r > a: &\quad E_z, H_z \propto K_\ell\left(\tfrac{wr}{a}\right) e^{i\ell\phi}, \end{aligned}$$

where J_ℓ and K_ℓ are the Bessel and modified Bessel functions. The parameters

$$\begin{aligned} u^2 &= a^2\,(n_1^2 k_0^2 - \beta^2), \\ w^2 &= a^2\,(\beta^2 - n_2^2 k_0^2), \\ V^2 &= u^2 + w^2 = (k_0 a)^2 (n_1^2 - n_2^2). \end{aligned} \tag{1.9}$$

define the normalized frequency V, which controls the number of supported modes.

Imposing boundary conditions at $r = a$ gives rise to families of hybrid modes, TE, TM, HE and EH, with the fundamental HE_{11} mode existing for any $V > 0$ and thus without cutoff. In the weakly guiding regime, where $\Delta = (n_1 - n_2)/n_1 \ll 1$, the full vectorial problem reduces to nearly linearly polarized solutions $\mathrm{LP}_{\ell m}$ obtained from a scalar Helmholtz equation. The HE_{11} mode reduces to the LP_{01} mode, with circularly symmetric, node-free intensity, while higher-order LP modes appear only above specific cutoffs of V. Single-mode operation is ensured for $V < 2.405$.

In femtosecond-laser-written waveguides, where $\Delta n \sim 10^{-3} - 10^{-2}$, the weakly guiding approximation is fully valid. These structures therefore operate essentially in the LP_{01} mode, unlike higher-contrast or asymmetric waveguides where distinct TE or TM modes may also appear [52].

1.3.2 Coupled mode theory

The ability to exchange optical power between adjacent waveguides, and thereby implement interferometric networks, can be rigorously described using the framework of coupled-mode theory (CMT) [54]. This formalism provides an accurate description of how the evanescent tails of neighboring guided modes overlap, enabling the transfer of energy between distinct channels.

When two waveguides are brought close enough that their evanescent fields overlap, the total field of the composite structure can be expressed as a superposition of the fundamental modes of the isolated guides. Under the weak-coupling approximation, where the modal distributions and propagation constants of each waveguide are only slightly perturbed, the electric field may be written as

$$E(x,z,t) = A(z)\,E_a(x,y)\,e^{i(\omega t-\beta_a z)} + B(z)\,E_b(x,y)\,e^{i(\omega t-\beta_b z)}, \qquad (1.10)$$

where $E_a(x,y)$ and $E_b(x,y)$ are the normalized modal profiles of the individual waveguides, β_a and β_b their propagation constants, and $A(z)$ and $B(z)$ are slowly varying amplitudes that describe the longitudinal power evolution.

By substituting this ansatz into Maxwell's equations and accounting for the mutual perturbation of the dielectric environment, one obtains the coupled-mode equations [54]:

$$\frac{dA}{dz} = -i\kappa_{ab}\,B(z)\,e^{i\Delta\beta z} - i\kappa_{aa}\,A(z), \qquad (1.11)$$

$$\frac{dB}{dz} = -i\kappa_{ba}\,A(z)\,e^{-i\Delta\beta z} - i\kappa_{bb}\,B(z), \qquad (1.12)$$

where $\Delta\beta = \beta_a - \beta_b$ is the propagation constant mismatch, κ_{ab} and κ_{ba} represent the coupling between the two guides, and κ_{aa}, κ_{bb} are small self-correction terms. The coupling coefficients can be explicitly written as overlap integrals between the modal fields and the perturbation of the refractive index distribution [51]:

$$\kappa_{ij} = \frac{k_0}{2n_i} \iint E_i(x,y)\,\Delta n_j^2(x,y)\,E_j(x,y)\,dx\,dy, \qquad (1.13)$$

where $E_i(x,y)$ and $E_j(x,y)$ are the modal profiles of the i-th and j-th waveguides, n_i is the effective index of mode i, and $\Delta n_j(x,y)$ is the index perturbation due to the presence of waveguide j. Equation (1.13) highlights that coupling is stronger when the evanescent tails of the modes overlap significantly in the interstitial region between the guides.

In the case of two identical, phase-matched waveguides ($\beta_a = \beta_b, \Delta\beta = 0$), the self-coupling terms κ_{aa} and κ_{bb} are negligible compared to the cross-coupling κ_{ab} and are thus set to zero in the simplified model. Only $\kappa_{ab} = \kappa_{ba} = \kappa$ governs the power exchange:

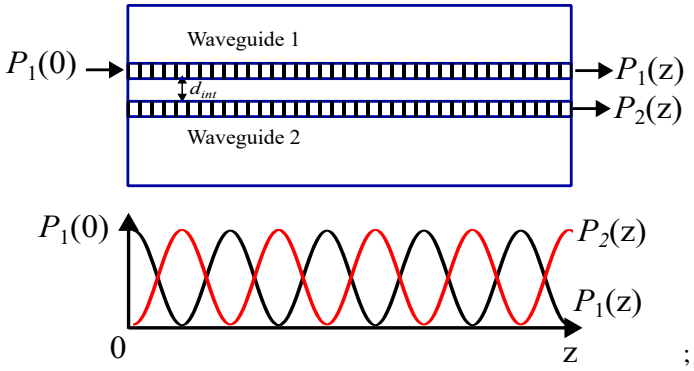

Figure 1.2: *Power exchange between two adjacent waveguides. An optical power $P_1(0)$ is launched into Waveguide 1, and as the field propagates along the z-axis, a sinusoidal transfer of power occurs between the two waveguides. Image adapted from [55].*

$$\frac{dA}{dz} = -i\kappa B(z), \tag{1.14a}$$

$$\frac{dB}{dz} = -i\kappa A(z). \tag{1.14b}$$

If light is injected only into one channel at $z = 0$ (e.g. $A(0) = A_0$, $B(0) = 0$), the solution is

$$A(z) = A_0 \cos(\kappa z), \tag{1.15a}$$

$$B(z) = -iA_0 \sin(\kappa z). \tag{1.15b}$$

so that the corresponding optical powers are

$$P_a(z) = |A(z)|^2 = P_0 \cos^2(\kappa z), \tag{1.16a}$$

$$P_b(z) = |B(z)|^2 = P_0 \sin^2(\kappa z). \tag{1.16b}$$

where $P_0 = |A_0|^2$ is the injected power. Equations (1.16) show that power is exchanged sinusoidally between the two waveguides (Fig. 1.2) along the propagation direction, with full transfer occurring after a coupling length

$L_c = \pi/(2\kappa)$. This coupling length, and therefore the splitting ratio of a directional coupler, can be engineered by adjusting the waveguide separation and the interaction length. In practice, the coupling coefficient κ decays approximately exponentially with the distance between waveguides [51], making precise fabrication control essential for designing photonic circuits.

CHAPTER 2

Femtosecond Laser Micromachining

Over the past twenty years, Femtosecond Laser Micromachining (FLM) has become a widely adopted and versatile technique for the direct writing and fast prototyping of integrated photonic components. Its unique ability to produce localized, permanent modifications within a broad range of materials, including glasses [56–58], crystals [59], polymers [60], and resins [61], has made it an enabling platform for numerous applications, from integrated optics and quantum photonic circuits to optofluidic systems and micro-mechanical devices.

The technique relies on the nonlinear interaction between ultra-short laser pulses and a transparent dielectric substrate. When such pulses are tightly focused into the bulk of the material, they can reach intensities high enough (up to $1 \times 10^{19}\,\mathrm{W\,m^{-2}}$) to trigger nonlinear absorption mechanisms such as multiphoton absorption and avalanche ionization. These interactions are highly confined to the focal volume, producing permanent modifications in a micrometric region (voxel) without affecting the surrounding material. By

translating the sample relative to the laser focus with high-precision motion stages, it becomes possible to define arbitrary three-dimensional structures within the material volume.

The origins of FLM can be traced back to 1994, when Du et al. [62] first demonstrated the possibility of using femtosecond laser pulses to ablate micrometric features in fused silica and metallic surfaces. This pivotal result, achieved using a Chirped Pulse Amplification system, established the feasibility of FLM. A few years later, in 1996, Davis et al. [63] reported the formation of buried optical waveguides in glass by inducing a localized refractive index increase through femtosecond laser exposure, thus introducing a new approach to fabricating integrated optical circuits.

FLM distinguishes itself from conventional photolithographic fabrication through a series of key advantages that make it highly attractive for integrated photonic applications. One of the most significant advantages of FLM lies in its simplicity and fast prototyping.

The fabrication process involves first designing the waveguide path using dedicated software. The resulting layout is then sent to a control system that drives the 3D translation stages, which move the sample relative to the laser focus to perform the actual inscription. Since the entire process is single-step and fully software-controlled, it requires no photomasks, multistep procedures, or cleanroom facilities, significantly reducing both complexity and cost, making FLM a practical solution for research and development environments.

Another unique feature of FLM is its ability to directly inscribe three-dimensional structures within the bulk of a transparent substrate. Owing to the tight spatial confinement associated with nonlinear absorption, material modifications are localized to the focal region of the laser, allowing precise 3D patterning that goes beyond the planar constraints of traditional lithographic techniques. FLM is also characterized by a high degree of material flexibility. By adjusting irradiation parameters such as pulse energy, repetition rate, and writing speed, the technique can be optimized for various classes of transparent materials.

However, some limitations remain. A major drawback is the relatively low refractive index contrast achievable in most glass substrates, typically on

the order of $\Delta n \sim 10^{-3}$–10^{-2}. This limits optical confinement and imposes a lower bound on the minimum achievable bending radius, beyond which bending losses become significant. As a result, this translates into larger chip dimensions compared to other integrated photonic platforms. Additionally, since FLM is a serial fabrication method, each structure being inscribed point by point, it inherently scales less efficiently than parallel techniques used in semiconductor manufacturing.

Despite these constraints, FLM remains a reliable and versatile approach for a broad range of photonic applications. Its capability to rapidly prototype and reconfigure low-loss optical components within a monolithic, transparent substrate provides significant advantages in terms of flexibility and development speed. As such, FLM continues to play an important role in advancing integrated photonic technologies.

2.1 Femtosecond laser interaction with transparent material

Although a complete description of the physical mechanisms underlying FLM is still not fully established [64], the process is generally described in two main stages. First, the interaction of the intense femtosecond laser pulse with the transparent material leads to the generation of a free-electron plasma within the focal volume. This is followed by the thermal relaxation phase, during which the absorbed energy is transferred from the excited electrons to the lattice, ultimately resulting in a permanent material modification.

2.1.1 Free-electron plasma formation

Since FLM relies on nonlinear absorption, the laser photon energy given by $h\nu$ (where h is Planck's constant and ν is the optical frequency), must be lower than the material's bandgap energy E_g. Under these conditions, the excitation of electrons from the valence band to the conduction band occurs via nonlinear photoionization processes. Two main mechanisms contribute to this: multiphoton absorption and tunneling ionization.

In multiphoton absorption, an electron simultaneously absorbs multiple m photons whose combined energy exceeds the bandgap, allowing its promotion to the conduction band (i.e $mh\nu > E_g$). Alternatively, at high laser intensities

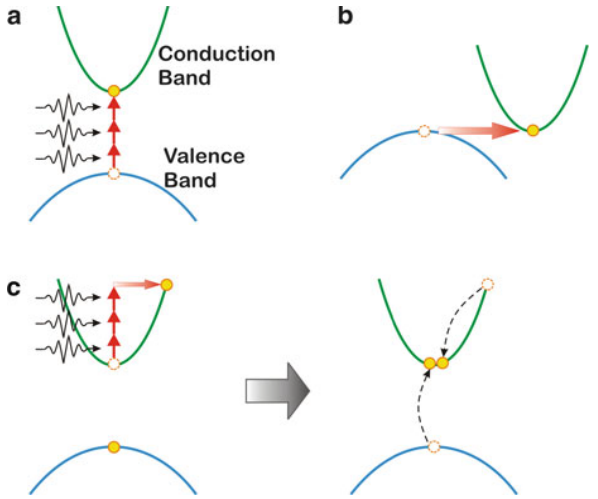

Figure 2.1: *Physical mechanisms that provide seed electrons for plasma generation. An electron initially in the valence band (blue) can be excited to the conduction band (red) through* **a** *multiphoton absorption,* **b** *tunneling ionization, or* **c** *impact ionization, the latter triggering an avalanche process.*

tunnel ionization occur. The strong electric field of the laser pulse distorts the energy bands, increasing the probability that electrons tunnel through the reduced potential barrier into the conduction band. The relative contribution of these two processes is typically evaluated through the Keldysh parameter γ [65], defined as:

$$\gamma = \frac{\omega}{e}\sqrt{\frac{m_e c n \varepsilon_0 E_g}{I}},$$

where ω is the laser frequency, e the elementary charge, m_e the electron mass, n the refractive index of the material, ε_0 the vacuum permittivity, E_g the material bandgap, and I the laser intensity. Multiphoton ionization dominates when $\gamma \gg 1.5$, while tunneling ionization prevails for $\gamma \ll 1.5$. In FLM, the process typically operates in the intermediate regime ($\gamma \sim 1$), where both multiphoton and tunneling ionization contribute significantly to the excitation process.

Once a seed electron is promoted to the conduction band, it can absorb additional photons through linear absorption, gaining enough kinetic energy to ionize other valence electrons via impact ionization in a process known as avalanche ionization. In this way, every excited electron becomes a seed for

further ionizations, triggering an avalanche ionization process that rapidly increases the density of free carriers in the focal volume. This exponential growth continues until the electron density reaches the critical plasma density, defined as

$$n_c = \frac{m_e \varepsilon_0 \omega^2}{e^2}$$

At this point, the plasma, initially transparent to the incoming radiation, becomes strongly absorbing [66], confining the energy within the focal region.

This regime is what makes FLW both deterministic and versatile. If the process were driven solely by multiphoton or tunneling ionization, the outcome would be highly sensitive to parameters such as laser frequency and bandgap energy, making the process less reproducible and harder to generalize across different materials.

It becomes clear why the use of sub-picosecond pulses is a fundamental requirement for femtosecond laser micromachining. The peak intensities required to initiate nonlinear ionization and trigger avalanche ionization can only be achieved with ultrashort pulses. For longer pulses, which exhibit lower peak intensities, the formation of plasma remains possible, however, in this case, the seed electrons required to initiate the avalanche ionization process are typically supplied by thermally excited impurities or defect states within the material. These initial carriers are generally few in number and randomly distributed, resulting in a stochastic and spatially non-uniform activation of avalanche ionization. As a result, material modification becomes less precise and uniform.

2.1.2 Thermal relaxation and material modification

After the plasma is generated within the focal volume, its energy is transferred to the surrounding lattice through electron-phonon interactions, typically over a timescale of approximately 10 ps [67]. Since femtosecond laser pulses are much shorter than this relaxation time, absorption and energy dissipation are temporally decoupled. This separation allows the laser energy to remain confined to a micrometric volume, enhancing the spatial precision and localization of the material modification.

Depending on the deposited energy, three main regimes of modification can be identified. At low pulse energies, a smooth and isotropic refractive index increase occurs, which is ideal for fabricating low-loss optical waveguides. This change can result from rapid quenching of a transiently molten region, leading to increased density [68], or from the formation of color centers [69] and ion migration [70], depending on the substrate. As the deposited energy increases, periodic nanostructures known as nanogratings can form due to the interference between the laser field and the free-electron plasma. These structures induce birefringence and are highly sensitive to selective chemical etching, enabling the fabrication of microfluidic channels [71], hollow waveguides [72], or crystal nanostructuring [59]. At even higher energies, the sudden release of energy from the plasma to the lattice can trigger a shockwave, resulting in the formation of voids within the material [73]. These micro-explosions can be exploited for applications such as 3D memories [74] or the development of photonic bandgap materials [75].

2.2 Waveguide writing parameters

As discussed in previous sections, FLM enables the fabrication of a wide range of structures within transparent materials. Since this thesis focuses on integrated photonic circuits, we now analyze the most relevant parameters involved in the fabrication of optical waveguides using FLM.

2.2.1 Focusing

To induce nonlinear absorption, the laser is tightly focused inside the transparent substrate to achieve high intensities in a micrometric volume. Assuming the linear propagation of a Gaussian beam in a dielectric of refractive index n [64], and neglecting aberrations, the minimum waist radius w_0 (half the spot size) and the Rayleigh range z_0 (half the depth of focus) are given by:

$$w_0 = \frac{M^2\lambda}{\pi \mathrm{NA}}, \tag{2.1}$$

$$z_0 = \frac{M^2\lambda n}{\pi \mathrm{NA}^2}, \tag{2.2}$$

where λ is the wavelength, NA is the numerical aperture of the focusing objective, and M^2 is the beam quality factor.

Aberrations, such as spherical or chromatic, can distort the intensity distribution. Microscope objectives are used to minimize these effects, and in particular, water- or oil-immersion objectives are preferred when writing deep inside the substrate to reduce spherical aberrations caused by the refractive index mismatch at the air-glass interface. Since the ratio w_0/z_0 is proportional to NA$/n$, it follows that the shape of the focal spot depends on the NA. Typically, since NA $< n$ (with $n \approx 1.5$ for most glasses), the focal volume is axially elongated.

Furthermore, at high intensities, the nonlinear refractive index n_2 comes into play. If the laser power exceeds the critical power for self-focusing: $P_c = 3.77\lambda^2/(8\pi n_0 n_2)$, Kerr self-focusing occurs. The resulting increase in intensity may lead to plasma formation, which introduces a defocusing effect. The interplay between Kerr self-focusing and plasma defocusing gives rise to filamentary propagation, resulting in an axially extended modification.

2.2.2 Repetition Rate

The repetition rate (number of pulses per second) significantly affects the waveguide properties. Three regimes are typically distinguished [76]:

- **Low repetition rate (< 250 kHz)**: The time between pulses is longer than the heat diffusion time, so no thermal accumulation occurs. Each pulse acts independently, leading to asymmetric modifications similar to the focal spot [77]. While widely used due to the availability of high-energy Ti:sapphire lasers, this regime suffers from low scan speeds (a few $\mu\mathrm{m\,s^{-1}}$) and limited fabrication throughput.
- **High repetition rate (MHz regime)**: Thermal accumulation occurs because the subsequent pulse arrives before heat has diffused. This results in more uniform and symmetric waveguides and allows higher scan speeds ($50\,\mathrm{mm\,s^{-1}}$ to $100\,\mathrm{mm\,s^{-1}}$), improving the fabrication rate. However, due to the lower pulse energies, tight focusing is needed.
- **Intermediate regime (100 kHz–1 MHz)**: Combines the advantages of the two previous regimes. The pulses are energetic enough to avoid

tight focusing, while thermal accumulation improves waveguide quality. This regime is commonly used in modern Yb-based laser systems [78].

2.2.3 Writing Geometry

Two main configurations exist for translating the sample with respect to the laser beam:

- **Longitudinal writing**: The sample is translated along the propagation direction of the beam. This geometry yields symmetric waveguides but is limited by the short working distance of high-NA objectives.
- **Transverse writing**: The sample moves perpendicular to the beam. This enables the fabrication of complex 3D structures throughout the substrate thickness. However, the resulting focal volume is elliptical due to the w_0/z_0 ratio, leading to elliptical waveguide cross-sections and potentially birefringent modes. Beam shaping and multiscan strategies can be used to mitigate this effect.

2.2.4 Other Parameters

Additional parameters influencing waveguide performance include:

- **Scan speed**: Affects the energy density deposited. Slower scans increase modification strength.
- **Number of scans**: Multiple passes increase the refractive index contrast and reduce the ellipticity of the waveguide cross-section, thereby lowering birefringence.
- **Writing direction**: The direction of scanning relative to the beam propagation influences the final waveguide properties due to the so-called quill effect (referred to as the asymmetric phase front tilt of the incoming ultrafast pulses) [79].

Careful optimization of these parameters is essential for achieving high-quality waveguides suitable for integrated photonic circuits.

2.3 Quantum photonics components with FLM

The optical performance of laser-written waveguides is strongly influenced by the choice of substrate and the energy deposition regime. Borosilicate glasses, such as *Corning EAGLE XG®* and *Schott AF32®*, are widely used due to their suitability for high-repetition-rate writing regimes (from 500 kHz to 5 MHz), which promote thermal accumulation and result in symmetric waveguide profiles with low birefringence, typically on the order of 10^{-5}. Post-fabrication thermal annealing can further reduce birefringence to nearly 10^{-6} and enhance mode confinement, allowing tight bending radii below 10 mm [1].

Typically, waveguides exhibit cross-sectional dimensions on the order of a few μm^2, with a low refractive index contrast between the core and the cladding region, usually in the range of 10^{-2} to 10^{-3}. This refractive index modification, which is similar to that of a single-mode fiber, enables very efficient fiber-to-chip coupling, with coupling losses typically in the range of 0.1 dB to 0.5 dB. Additionally, propagation losses have been reported to be as low as 0.1 dB cm^{-1}.

One of the key advantages of FLM lies in its versatility: such low loss values can be achieved for waveguides operating across a broad spectral range, from the visible to the telecom wavelengths. This is achievable by adjusting laser parameters such as writing power, scan speed, and repetition rate. In general, higher deposited energy, achieved through higher writing power or lower scan speeds, results in a larger modified volume and a stronger refractive index contrast, which improves confinement. However, the waveguide geometry must remain within specific dimensional limits to support only the fundamental mode, since multimode propagation can introduce instability and mode-dependent behavior in integrated components, such as directional couplers, which are typically optimized for single-mode operation.

Among the distinctive features of FLM, the ability to fabricate truly three-dimensional photonic structures and to precisely control polarization properties represents a major technological advantage over traditional planar platforms, such as lithography-based fabrication. These two aspects are particularly valued in the field of integrated quantum photonics.

From a structural perspective, FLM enables the realization of 3D circuit layouts that are physically impossible to replicate with planar approaches. This capability allows waveguides to pass over each other without intersections, avoiding the need for complex planar workarounds. A direct application of this feature was demonstrated in multi-layer interferometric schemes for assessing photon indistinguishability [80], where two vertically stacked layers of beam splitters and phase shifters implemented a cyclically symmetric interferometer design. Furthermore, the inherent 3D flexibility of FLM has enabled the realization of advanced quantum circuits such as the Quantum Fast Fourier Transform (QFFT) [81], implemented in a compact interferometric structure where waveguides are placed on the vertices of a projected hypercube and connected via 3D directional couplers. Passive phase shifts are introduced through geometric deformation of S-bends, allowing for controlled phase manipulation without active elements. Another peculiarity is related to the inscription of continuously coupled waveguide arrays. Unlike lithographic platforms, which are limited to nearest-neighbor coupling in one dimension, FLW allows the fabrication of 2D arrays with independently tunable second-order coupling [82–84].

The other important feature of FLM lies in the fine control over birefringence, making it suitable for polarization-encoded quantum information processing. While birefringence in laser-written waveguides can be minimized to support polarization-insensitive operation, it can also be deliberately engineered to create polarization-selective components. This includes directional couplers that preserve interference between polarization-entangled photons [85], enabling the manipulation of hyperentangled and cluster states. Integrated waveplates have been demonstrated by inscribing stress-inducing tracks or by writing waveguides with a slanted optical axis, thereby enabling the realization of on-chip single-qubit gates [86]. For two-qubit gates, partially polarizing beam splitters have been developed by exploiting the polarization-dependent coupling behavior [87]. Additionally, polarization-insensitive circuits can be achieved either through structural compensation (e.g., laser-induced stress track placed near the interaction region) or via post-fabrication thermal annealing [88].

In the following sections, I will present the key components that constitute

the fundamental building blocks required to construct an integrated photonic circuit.

2.3.1 Directional Coupler

A directional coupler (DC) is a fundamental photonic component consisting of two waveguides brought into close proximity over a specific interaction length, allowing optical power to be transferred between them through evanescent field coupling. This light transfer mechanism, based on the overlap of the evanescent fields of the guided modes, has been described in detail in Section 1.3.2. By adjusting the interaction distance or the interaction length, it is possible to control the power splitting ratio at the outputs. In the context of integrated photonics, the DC serves as the on-chip analogue of a bulk optical beam splitter.

The first realization of a DC realized in FLM dates back to 2001 and is credited to Streltsov and Borrelli [89]. The device was inscribed in a glass substrate using the focused output 400 nm output of a 25 fs laser oscillator. It operated in a single-mode regime and exhibited a power splitting ratio of 1.9 dB at a wavelength of 633 nm. The performance of DC is intrinsically dependent on both wavelength and polarization. These dependencies can be strategically exploited to engineer devices with tailored functionalities. For example, DC can be designed for wavelength-division multiplexing applications [90], enabling selective routing of different spectral components. On the other hand, broadband DC can be implemented to provide a stable splitting ratio across a wide wavelength range [91]. Moreover, by controlling polarization-dependent coupling, it is possible to fabricate polarizing DC that separate orthogonal polarization states [92]. Alternatively, polarization-insensitive couplers can be realized, either through structural compensation, such as introducing stress tracks or via post-processing techniques like thermal annealing [88], as previously discussed.

2.3.2 Mach-Zehnder interferometer

A Mach-Zehnder interferometer (MZI) is an integrated photonic device composed of two directional couplers connected by two optical paths. The first

coupler splits the incoming light into two separate branches, which then recombine at the second coupler. Before recombination, the light traveling in each arm accumulates a relative phase shift, which can arise from a difference in physical path length or from a refractive index variation in one of the arms. This phase difference determines the interference pattern observed at the output ports.

The first demonstration of an integrated MZI fabricated by FLM is attributed to Minoshima et al. in 2002 [93]. In this work the MZI was realized by cascading two X-couplers, i.e., directional couplers formed by waveguides crossing on different planes. The two couplers were sequentially arranged with a precisely engineered optical path difference of approximately 10 µm between the interferometer arms. This asymmetry introduced a wavelength-dependent phase shift, enabling the device to act as a spectral filter.

Passive MZI have found applications in areas such as biosensing, where phase shifts induced by external perturbations reveal information about the surrounding medium [94], as well as quantum optics [95, 96]. However, a key advancement in the field of integrated quantum photonics lies in the transition from passive to active operation. This enables the realization of reconfigurable MZIs, an approach that will be discussed in the following sections.

2.3.3 Reconfigurability

As mentioned earlier, the development of reconfigurable MZI is a key step in integrated quantum photonics. These devices are fundamental for information processing, and are widely used in applications such as programmable circuits, optical switching, and quantum state control.

Reconfigurability is typically achieved by integrating a tunable phase shifter into one of the interferometer arms, enabling precise phase control. In the context of FLM, the main effects investigated for this purpose are the electro-optic, elasto-optic and thermo-optic effects, which are based on the modulation of the refractive index of a material in response to electric fields, mechanical stress or temperature variations, respectively. However, due to the inversion symmetry of glass, the electro-optic effect is extremely weak, and even when a non-negligible $\chi^{(2)}$ is artificially induced, high voltages are

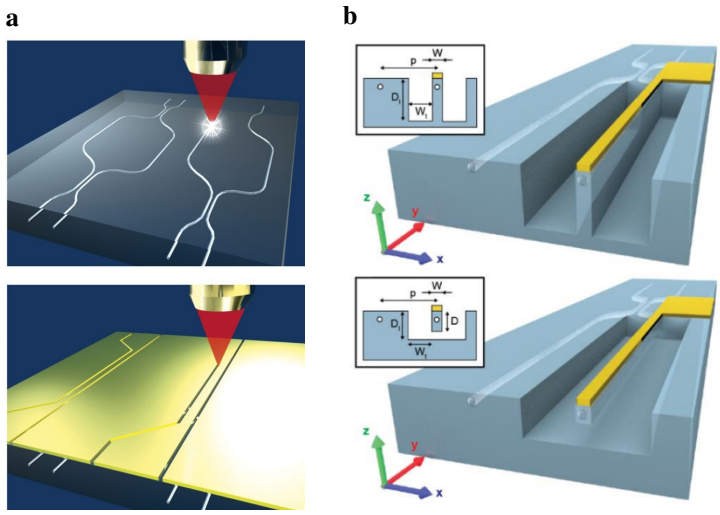

Figure 2.2: *Reconfigurable FLM circuits. Following the inscription of the optical circuit (***a** *top), thermal phase shifters are realized on the glass surface by depositing a thin gold layer, subsequently patterned with a femtosecond laser to define the conductive tracks (***a** *bottom). Image taken from [97]. The implementation of deep trenches between waveguides (***b** *top), or the inscription of waveguides on bridge-like structures (***b** *bottom), minimizes both thermal cross-talk and the required dissipated power, enabling scalable integration of thermal phase shifters in FLM platforms. Image taken from [98].*

typically required to obtain meaningful phase shifts [99]. Elasto-optic modulators have been successfully demonstrated using piezoelectric actuators to modify the birefringence of shallow waveguides [100, 101], but their scalability to large circuits is limited by the complexity of integrating mechanical components.

As a result, nearly all reconfigurable FLM photonic circuits reported to date exploit the thermo-optic effect, owing to its simplicity of integration and compatibility with standard glass substrates. In these implementations, a resistive microheaters, typically made from a thin metal film, are deposited on the chip surface above the waveguides. When a voltage is applied, heat is generated by Joule dissipation, increasing the local temperature and thereby changing the refractive index in the underlying region. If the waveguide lies sufficiently close to the surface, this index change alters the propagation constant of the guided mode, enabling precise phase control.

The first realizations date back to 2015, when two independent works demonstrated this approach [97, 102]. In particular, in the former work,

microheaters were created by depositing a nanometric gold layer onto a glass substrate with pre-inscribed waveguides (Fig.3.6a). The same femtosecond laser, after precise realignment, was then used to define the resistor pattern by selectively ablating the metal layer. This approach has been used to implement various reconfigurable quantum devices, including a three-arm interferometer for multiphase estimation [103] and a four-mode universal photonic processor [104].

However, scaling the number of phase shifters within a chip introduces new challenges. In particular, the non-negligible thermal conductivity of glass leads to thermal cross-talk, where heaters intended to act on a specific waveguide unintentionally affect neighboring ones. To mitigate this issue, advanced geometries have been proposed, such as the selective removal of substrate material between adjacent waveguides using water-assisted laser ablation (Fig.3.6b) [98]. These techniques significantly reduce heat diffusion, yielding an order of magnitude reduction in cross-talk and in the power required for a full 2π phase shift, reaching values as low as 20 mW to 30 mW. Additional improvements can be obtained by operating the device in vacuum conditions, which further enhances thermal isolation.

However, the main trade-off is in the modulation speed. The introduction of thermal isolation structures increases the thermal time constant, leading to slower dynamics: from a few milliseconds up to tens of milliseconds to achieve a full 2π phase shift. More generally, the frequency response of standard thermo-optic FLW phase shifters is currently limited to tens-of-Hz, which constrains their use in applications requiring high-speed modulation. Nonetheless, some strategies have been proposed to improve speed, such as using optimized voltage driving signals or placing the waveguides extremely close to the surface, just beneath the heaters.

2.4 Comparison with other integrated photonics platforms

After an extensive explanation of the fabrication technology used in this thesis, is dutiful give an overview of the other possible technology for integrated photonics. In the last decades integrated photonics has seen extraordinary progress. Today, photonic integrated circuits (PICs) are capable of hosting

hundreds of components, such as modulators, phase shifters, filters, and even on-chip light sources and detectors, making them suitable for large-scale classical and quantum information processing [105–107]. This section reviews the most relevant platforms for the realization of integrated photonic circuits, highlighting their key properties.

2.4.1 Silica on silicon

The silica-on-silicon platform relies on a well-established, CMOS-compatible fabrication process, where a doped silica layer is typically deposited onto a silicon substrate. This layer is then patterned using photolithography and etched to define the waveguide structures. A silica cladding layer is subsequently added, resulting in a low refractive index contrast, generally between 1% and 2%. These waveguides offer exceptionally low propagation losses (reaching values as low as 0.05 dB/cm) and allow for highly efficient coupling to standard optical fibers, due to the well-matched guided mode dimensions. These characteristics made the platform suitable for the first demonstration of a quantum photonic integrated circuit (PIC) [108], where minimizing losses is critical for successful quantum photonics applications. Recent developments in this technology include the realization of single photon source arrays [109], and further reduction in propagation losses, down to 0.009 dB/cm, as well as the fabrication of polarization-insensitive waveguides with compact bending radii of approximately 1 mm [110]. However, the platform faces certain limitations: the relatively low refractive index contrast limits integration density and results in larger bending radii, and fast modulation is not readily achievable, as phase control relies primarily on the thermo-optic effect.

2.4.2 Silicon on insulator

The silicon-on-insulator (SOI) platform is considered one of the most mature and widely adopted technologies for integrated photonics, particularly within the telecom wavelength range (1.3–1.55 μm), as silicon's limited transparency prevents its use in the visible and near-infrared regions, restricting its applicability outside this spectral window. In this platform, waveguides consist of

a silicon core embedded in a silica cladding, resulting in a high refractive index contrast. This strong optical confinement enables ultra-compact bending radii (down to the micrometer scale), the implementation of ring resonators with large free spectral ranges [111], and, more broadly, high integration density for photonic circuits.

This high index contrast results in a significant mode mismatch with standard optical fibers, leading to substantial coupling losses. Despite these limitations, recent advancements in grating coupler design have significantly improved fiber-to-chip coupling efficiency, reducing losses to below 1 dB per facet, with reported values around 0.5 dB [112]. Regarding propagation losses, state of the art SOI waveguides have demonstrated values as low as 0.3 dB/cm. Nevertheless, propagation losses strongly depend on the specific silicon waveguide geometry and fabrication process. Non-optimized or fully etched strip waveguides may exhibit losses in the range of 2–3 dB/cm, primarily due to fabrication-induced imperfections such as sidewall roughness at the core–cladding interface [113]. In contrast, shallow-etched (rib) waveguides typically achieve lower losses, commonly in the range of 0.7–1 dB/cm, owing to reduced modal overlap with etched sidewalls.

Reconfigurability in SOI is achieved by using TOPS, but also with faster phase shifters exploiting the plasma dispersion effect, capable of operating in tens of GHz regime, albeit at the cost of phase-dependent insertion losses during operation [114]. Additionally, electro-absorption modulators (EAMs) can be employed to achieve high-speed modulation through carrier-induced changes in optical absorption, providing an alternative mechanism for reconfigurable and dynamic control. Moreover, the platform supports a variety of integrated components to enhance circuit functionality, including single-photon sources based on spontaneous four-wave mixing (SFWM) [115, 116] and superconducting single-photon detectors [117], making it a promising candidate for quantum photonic applications.

Nonetheless, SOI presents several intrinsic limitations. Silicon exhibits strong two-photon absorption at telecom wavelengths, which introduces nonlinear losses and restricts power handling. Furthermore, due to its centrosymmetric crystal structure, silicon lacks second-order ($\chi^{(2)}$) nonlinearity, rendering it unsuitable for electro-optic modulation or second-harmonic generation

without hybrid integration. Lastly, the platform is prone to free-carrier dispersion and thermal effects, which can lead to instabilities under high-speed or high-power operation.

2.4.3 Silicon nitride

Silicon nitride (SiN) offers a lower refractive index contrast ($n \approx 2.0$) compared to silicon, yet enables exceptionally low linear losses, with values below 2 dB/m demonstrated in optimized waveguides [107]. This material platform is fully CMOS-compatible and features a broad transparency window spanning from the visible to the mid-infrared range (approximately 400—2350 nm), making it highly suitable for broadband applications, including nonlinear optics.

SiN is also immune to two-photon absorption at telecom wavelengths and exhibits moderate third-order nonlinearity ($\chi^{(3)}$), which enables efficient SFWM and related nonlinear processes. Owing to these properties, SiN has been successfully employed in the realization of integrated single-photon sources based on SFWM [107, 118–121]. It has also been used for the on-chip integration of superconducting single-photon detectors, supporting the development of compact quantum photonic circuits [107, 122].

On the downside, SiN lacks both second-order ($\chi^{(2)}$) nonlinear effects and intrinsic electro-optic properties, limiting its ability to support direct high-speed modulation. However, hybrid integration strategies can be employed to introduce fast modulation functionalities [107].

Traditionally, SiN waveguides suffered from relatively high coupling losses with standard single-mode fibers due to mode size mismatch. Nevertheless, recent progress in edge-coupling techniques and spot-size converters has significantly improved fiber-to-chip coupling efficiency, with demonstrated losses as low as 0.13 dB per facet [107].

2.4.4 Thin-film lithium niobate

The thin-film lithium niobate (TFLN) platform consists of a thin $LiNbO_3$ layer on an insulating substrate such as SiO_2. This platform has emerged as a leading photonic integration technology that combines low optical loss with

strong electro-optic and nonlinear responses. Lithium niobate possesses a large second-order ($\chi^{(2)}$) nonlinearity and a high Pockels coefficient, enabling efficient, high-speed electro-optic modulation without relying on thermal or free-carrier effects typical of silicon-based platforms [123]. Compared to bulk lithium niobate, TFLN provides higher refractive index contrast and tight optical confinement, which supports compact waveguides and dense photonic integration while maintaining broad transparency from visible to mid-infrared wavelengths [124].

Recent advances have demonstrated TFLN waveguides with state-of-the-art propagation losses [124, 125] and electro-optic modulators with bandwidths exceeding tens of GHz and low half-wave voltage-length products, indicating both high speed and modulation efficiency [123]. The coexistence of strong $\chi^{(2)}$ nonlinearity and efficient electro-optic modulation makes TFLN especially attractive for quantum photonic integrated circuits, where on-chip photon-pair generation, frequency conversion, and fast tuning are essential [126]. Nevertheless, optimizing fiber-to-chip coupling and overcoming fabrication complexity remain ongoing challenges for broader industrial adoption.

Part II

Experimental

CHAPTER 3

Materials and Methods

All of the PICs discussed in this thesis were fabricated using FLM technology. This chapter aims to provide a comprehensive overview of the fabrication process employed for device realization, as well as the characterization technique used to assess the performance of the PICs.

3.1 Fabrication of the device

The fabrication of a PIC usually involves four main steps: the inscription of the optical circuits, the subsequent post-inscription processes, the realization of the thermal phase shifters required to enable reconfigurability and finally the packaging. All fabrication steps are carried out at the Physics Department of Politecnico di Milano, with the exception of metal deposition, which is performed at PoliFab, the university's cleanroom facility.

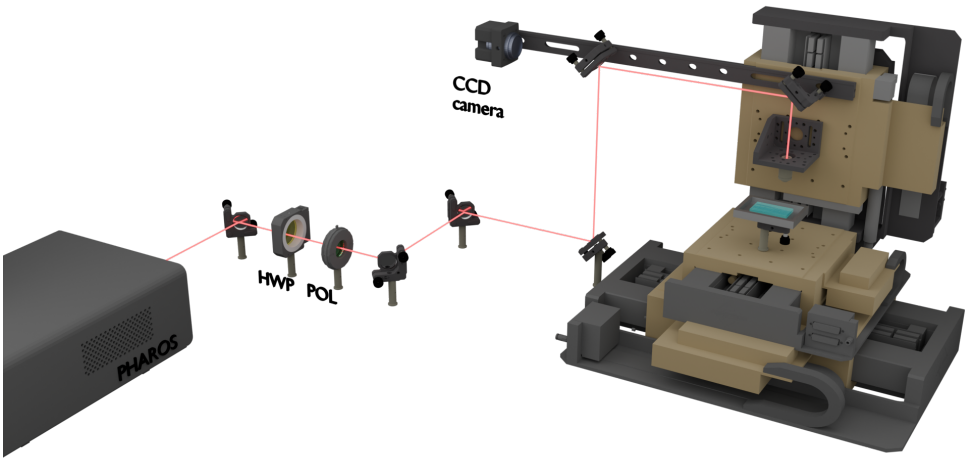

Figure 3.1: *Schematic of the FLM setup. The output of a 1030 nm fs laser is adjusted in power by a software-controlled half-wave plate (HWP) combined with a linear polarizer (POL), and subsequently guided to the sample by dielectric mirrors. The beam is tightly focused through a microscope objective, while the translation of the sample (in-plane) and of the objective (along the vertical axis) enables three-dimensional structuring within the material.*

3.1.1 Femtosecond laser inscription

The fabrication setup adopted for the devices realization presented in this thesis is depicted in Figure 3.1.

The laser pulses used for fabrication is generated by a commercial Yb-based femtosecond laser source. In order to enable precise and automated control of the laser power the beam is attenuated using a combination of a half-wave plate (HWP) and a polarizer (POL) positioned in series immediately after the laser output. This setup allows fine tuning of the transmitted power by rotating the polarization direction of the linearly polarized beam via the HWP, followed by intensity filtering through the polarizer. The HWP is mounted onto a gear-driven rotary stage (Aerotech MPS75GR) with a minimum resolution of $1''$ ($0.00028°$), enabling high-precision control over the laser power. Moreover, a mechanical shutter is placed in the beam line to enable fast on–off switching, with a response time of approximately 10 ms. Then, the laser beam is directed into the substrate through a sequence of dielectric mirrors and focused using a microscope objective. In this work, a Zeiss W N-Achroplan 20×/0.5 water-immersion objective was employed. Its design minimizes spherical aberrations caused by refractive index mismatch at the glass–water interface. The moderate numerical aperture makes it suitable for multi-scan waveguide inscription, while the 2.6 mm working distance ensures compatibility with 1 mm-thick substrates.

The objective is mounted on a high-precision vertical motion stage, while the glass sample is fixed to a custom-designed holder using acetone-soluble glue, immersed in deionized water, and positioned on high-precision xy planar motion stages. The coordinated movement of the objective along the vertical axis and the substrate in the horizontal plane enables the fabrication of arbitrary three-dimensional geometries.

Alignment between the laser focus and the sample surface is achieved by imaging the back-reflected light from the glass surface onto a CCD camera (Edmund Optics), placed behind a partially transmissive mirror along the beam path. The laser power before the focusing optics is monitored with a handheld powermeter (Ophir Nova II), ensuring accurate and repeatable irradiation conditions.

All experiments reported in this thesis were carried out on commercial-grade Alkaline Earth Boro-Aluminosilicate glass (EAGLE XG®, Corning Inc.), selected for its excellent flatness, high surface quality, and low thickness tolerance, enabled by the fusion draw manufacturing process. The material also provides good thermal stability, low density, and high chemical resistance. Glass substrates with dimensions 100 mm × 50 mm × 1 mm were used for waveguide inscription.

Laser source

The fabrication system employs a compact ytterbium-based femtosecond laser (PHAROS, Light Conversion), composed of a Kerr-lens mode-locked oscillator, a regenerative amplifier, and a stretcher/compressor module, all enclosed in a sealed, thermally-stabilized housing to ensure operational stability under varying environmental conditions. The oscillator generates a pulse train at 76 MHz with sub-80 fs duration. To obtain high peak intensities, the system uses the chirped pulse amplification technique: pulses are initially stretched in time, amplified through a Yb:KGW crystal and finally recompressed.

The stretcher/compressor unit is based on a single high-efficiency transmission grating that can be adjusted to introduce either positive or negative chirp, enabling pulse duration tuning from approximately 170 fs to 10 ps. The system delivers pulses at a central wavelength of 1030 nm (± 5 nm), with energies up to 0.2 mJ and a maximum average output power of 10 W. The repetition rate is tunable from single-shot up to 1 MHz, while an internal pulse-picker maintains constant pulse energy across different output rates. A low-loss β-Barium Borate (BBO) Pockels cell integrated into the amplifier allows fast optical gating of the beam with microsecond-scale response times.

Translational stages

To achieve precise spatial control of the laser focus inside the substrate during fabrication, a high-precision, computer-controlled motion platform is employed. The system consists of three independent air-bearing linear stages (Aerotech ABL1500 series), driven by brushless linear servomotors that provide smooth motion. The vertical axis (z), which adjusts the focal

position of the objective, has a travel range of 50 mm, with a nominal resolution of 1 nm and maximum speed and acceleration of 300 mm/s and 20 m/s^2, respectively. The planar (x–y) motion is handled by two stages with travel ranges of 200 mm (x) and 100 mm (y), both offering the same resolution and acceleration capabilities, and a maximum speed of 2 m/s.

The motion system is controlled by the Aerotech A3200 software-based CNC controller, which accepts G-code input with update rates up to 1 kHz. Real-time feedback is provided by high-resolution optical encoders. A Transistor Transistor Logic (TTL) output from the stage controller can be fed into the laser electronics, allowing for precise synchronization between sample motion and laser shuttering, an essential feature for accurate fabrication of 3D photonic structures.

3.1.2 Post-inscription processes

After waveguide inscription, the sample undergoes a thermal annealing process to enhance the waveguide quality. Subsequently, the glass slab is cut to the desired shape using a precision diamond wire saw or diamond tip cutter. Finally, the facets are polished to ensure efficient light coupling. These post-processing steps are described in detail in this subsection.

Thermal annealing

Thermal annealing has been shown to improve the performance of femtosecond laser-inscribed waveguides, as demonstrated by Arriola et al. in 2013 [1]. The technique involves heating the glass substrate to a temperature range between its annealing and melting points. At the annealing temperature, the glass becomes sufficiently soft to allow internal stress relaxation through microscopic rearrangements of its molecular structure, while still maintaining its shape without deformation due to gravity. The sample is then cooled gradually, allowing uniform heat dissipation and structural stabilization. Once cooled below the strain point, the glass rigidifies and can be safely returned to room temperature. This controlled thermal treatment leads to a homogenization of the refractive index profile and a transition of the guided mode from a non-Gaussian shape to a Gaussian-like distribution. Additionally, thermal annealing eliminates the cladding-like region that forms between the

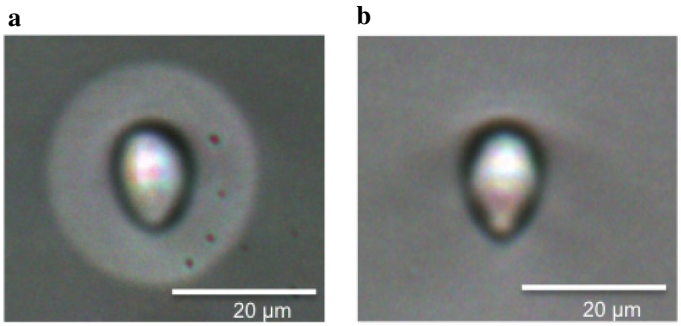

Figure 3.2: *Micrographs of the waveguides before (***a***) and after (***b***) annealing. Image taken from [1].*

laser-modified core and the surrounding unmodified material, as visible in Figure 3.2, resulting in a more confined and well-defined waveguide core.

This, in turn, reduces propagation and bending losses, enabling waveguiding at smaller radii of curvature. Finally, the process also mitigates birefringence within the waveguide structure, paving the way for polarization-insensitive photonic devices.

Cut and polish

After the annealing process, the sample undergoes a final preparation stage consisting of cutting and polishing. Typically, 1–2 mm are removed from both the input and output ends to eliminate edge effects or waveguide tapering, the latter referring to a gradual narrowing of the waveguide that can occur during the initial stage of laser writing, prior to plasma formation, thereby slightly modifying the material and impairing light propagation. The cutting process is performed using a Well 3241 diamond wire saw (Well Diamantdrahtsägen GmbH). Post-cutting, the facets often present surface roughness, leading to scattering and hindering characterization. Polishing can be performed manually or using an automatic system such as the KrellTech FLex Waveguide Polisher, following a procedure based on circular motions and the use of progressively finer abrasive discs, from coarse (30 μm) to fine (3 μm), until an optically smooth surface is obtained. Alternatively, controlled cleaving may be used, wherein a microfracture is initiated with a diamond-tipped tool, followed by the application of tensile stress to produce a pre-polished facet.

3.1.3 Fabrication of the thermo-optic phase shifters

Reconfigurability is obtained by fabricating thermo-optic phase shifters (TOPS) following the procedure described in [98]. The process begins with the creation of trenches through water-assisted laser ablation, followed by metal deposition, and concludes with the patterning of the resistor shape using the femtosecond laser.

Insulation trenches

The insulation trenches are made to confine heat within the target waveguide, thereby reducing the power required to operate the TOPS compared to structures without trenches [98], and minimizing thermal crosstalk with adjacent waveguides.

These are fabricated by means of a water-assisted femtosecond laser ablation process, which enables the carving of micrometric structures and the selective removal of glass with the precision, stability, and reproducibility inherent to the FLM platform. The process is carried out using the same W N-Achroplan 20×/0.5 Zeiss water-immersion objective employed for waveguide inscription (Section 3.1.1), allowing both operations to be performed in the same fabrication session or in separate sessions with proper re-alignment. The glass substrate, with the photonic circuit already inscribed, is mounted upside down on a sample holder so that the waveguides face downward, and is then covered with deionized water. This configuration enhances debris removal through the combined action of water flow and gravity. The laser beam is focused 15–20 μm below the bottom surface, initiating localized vaporization of the water and generating micro-explosions on the glass surface, which promote selective ablation.

Fabrication begins by ablating the sidewalls in successive horizontal planes separated by $\delta z = 1$ μm, proceeding from bottom to top to maintain the focal spot at the water–glass interface. The base of the trench is then machined, and once the final cut is complete, the detached glass portion falls away under its own weight. For large or non-convex geometries, the structure is divided into smaller sections to facilitate detachment. Accurate positioning is essential, as the spacing between neighboring waveguides is

typically around 100 μm; thus, alignment marks inscribed near the photonic circuit are located using the imaging system, and any rotation relative to the original inscription is corrected in software.

The machining parameters have been optimized to produce well-defined trench borders and high-quality surfaces. The optimum results were achieved with a laser wavelength of 1030 nm, pulse duration of 1 ps, repetition rate of 20 kHz, pulse energy of 1 μJ, and a translation speed of 4 mm/s. Furthermore, to increase the success rate, the total depth of 300 μm was achieved by sequentially detaching four smaller segments of 75 μm each, slightly increasing processing time but significantly improving fabrication yield and surface quality.

Metal deposition

The gold film deposition on the glass substrate is performed following the procedure reported in [127]. The process begins with a thorough cleaning of the glass surface to ensure proper adhesion of the metallic layers. The sample is first immersed in a piranha solution to remove organic contaminants; in some cases, an additional hydrofluoric acid bath is carried out to eliminate residual silica dust. The surface is then treated for 5 minutes in a plasma asher (PVA Tepla 300 AL), where exposure to oxygen plasma, generated by a 500 W microwave source, further removes impurities.

After cleaning, the sample is transferred into a sputtering system (Leybold LH Z400). In this process, energetic ions bombard a metallic target, ejecting atoms that redeposit on the sample surface. A 4 nm chromium layer is deposited first to promote adhesion, followed by a 96 nm gold layer. Gold is chosen as the conductive layer for its excellent electrical conductivity and high resistance to oxidation.

To improve the long-term stability of the conductive film, a thermal annealing step is performed. Gold deposited via sputtering is predominantly polycrystalline, an energetically less favourable state compared to the single-crystal form. Without annealing, the resistance of the phase shifters would drift over time [128], requiring frequent recalibration. The annealing consists of heating the sample at a rate of 10 °C/min up to 470 °C, holding this temperature for 1 hour, and cooling down to room temperature with-

out active thermal control. This treatment is carried out in a Nabertherm LT 9/11 SKM furnace under a controlled N_2 atmosphere. The maximum temperature remains well below the strain point of Eagle XG glass, ensuring that the waveguides are not structurally affected.

As the final step, the sheet resistance of the gold film is measured using a Jandel 4-point probe. This characterization provides the necessary data to precisely calibrate the subsequent laser ablation of the resistive heaters.

Resistor patterning

The last stage in the fabrication of the thermo-optic phase shifters consists in shaping the conductive paths on the gold layer. A 10×, 0.25 NA microscope objective is employed to focus the femtosecond laser beam (wavelength 1030 nm, repetition rate 1 MHz, pulse energy 200 nJ) onto the metal surface, with a pulse duration of 180 fs. The relatively low magnification allows the fabrication of tracks approximately 4 μm wide; additionally, multiple adjacent scans are performed to enhance electrical isolation from neighbouring structures. During the process, the sample is translated at a constant speed of 2 mm/s, while alignment with the existing waveguide pattern is achieved through markers previously written on the surface.

Since both the resistive elements and the contact pads are fabricated from the same gold layer, their electrical properties can be described in terms of the sheet resistance $\rho_\square$, which is the resistance of a square portion of the film and is given by $\rho_\square = \rho/t$, where ρ is the bulk resistivity of gold and t is the film thickness. This parameter is then used to design the geometry of the phase shifter. In particular, its total resistance is defined as:

$$R = \rho_\square \frac{l}{w}, \tag{3.1}$$

where l and w are the length and width of the conductive path, respectively. As ρ and t are fixed by the deposition process, the resistance can only be tuned by adjusting l and w. Increasing the length and reducing the width concentrates the power dissipation in the active region, thus enhancing the local heating effect. In practice, to achieve significant phase shifts with low electrical power, l is typically in the millimeter range, while w is kept to a

few micrometers. The exact dimensions are selected for each circuit based on the target performance and the measured sheet resistance of the gold layer.

3.1.4 Packaging

The final stage of the fabrication process is the packaging. This involves designing custom-made metallic holders to provide mechanical stability and electrical interfacing. The PIC is then attached to the metallic base using a thermally conductive adhesive. Electrical connections to custom-designed Printed Circuit Boards (PCBs) are made using a two-component, electrically conductive epoxy (Chemtronics CW2400-ND), as conventional soldering techniques would irreversibly damage the thin metallic film.

The final step in the fabrication process is the permanent attachment of optical fibers to the PIC, a procedure known as *pigtailing*. This method is employed not only to ensure robust and consistent device performance, but also to simplify interfacing with external systems and to facilitate efficient light injection. In practice, pigtailing provides a compact, connectorized assembly that can be directly coupled to standard optical sources, detectors, and instrumentation. The procedure comprises two main phases: precise alignment of the fibers with the inscribed waveguides, followed by fixation using a UV-curing adhesive that hardens upon exposure to ultraviolet light. The pigtailing setup used in this work is shown in Fig. 3.3. Fiber alignment is carried out using two computer-controlled, 6-axis hexapods (H-811.F2, PI–Physik Instrumente) driven by brushless DC motors, enabling highly accurate and repeatable positioning in all six degrees of freedom. The three translation axes have a resolution of 100 nm, while the three rotation axes can be adjusted with a minimum increment of 2 μrad. The PIC is mounted on a sample holder that combines motorized linear motion (M-110, PI) in the plane perpendicular to the propagation direction with manual control of the three rotational axes. Visual monitoring of the alignment and gluing steps is performed with a CCD camera (Edmund Optics 1312M) equipped with an optical zoom module (Opto 100-ZOS7-25). Once optimal coupling between the fibers and waveguides is achieved, the UV-curing stage is initiated. The adhesive, chosen for its strong bonding properties on glass and its refractive index matching that of the substrate to minimize Fresnel losses, is applied to

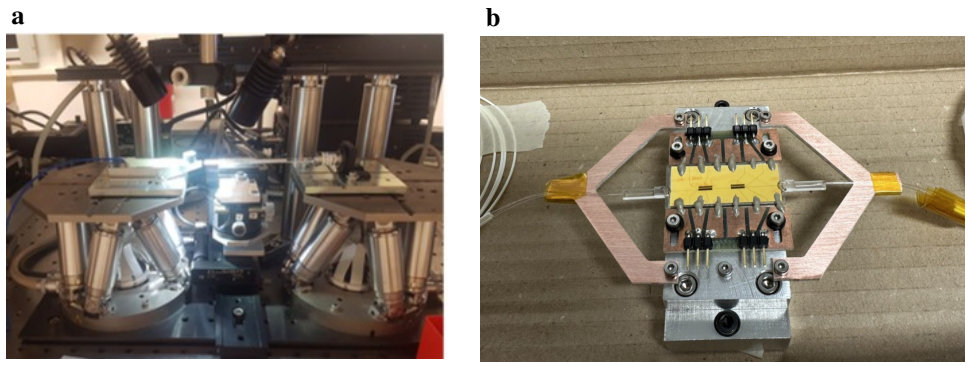

Figure 3.3: *Pigtailing setup.* **a** *The two side hexapods and the central sample holder enable precise control over the alignment between the fiber arrays and the waveguides.* **b** *Device after the pigtailing process. To enhance the mechanical robustness of the fibers, custom-designed metallic holders can be employed.*

the fiber facet. After confirming that alignment remains optimal, the adhesive is cured using a UV-LED source (L14310, Hamamatsu), achieving solidification within a few tens of seconds. When necessary, custom-made brackets are added to further enhance the mechanical robustness of the connectorized fibers.

3.2 Characterization methods

Following fabrication, the device is characterized. This section aims to provide an overview of the procedures used to evaluate the specifications of our PICs.

3.2.1 Microscope inspection

The first evaluation consists of inspecting the PIC with an optical microscope. For this purpose, a Nikon ME600 microscope equipped with a high-resolution CCD camera (PixeLINK B871) is used for image acquisition. Top-view inspection allows verification of the circuit layout, the quality of the induced refractive index contrast, and the absence of interruptions caused by dust during fabrication. Cross-sectional imaging is performed to ensure that no scratches are present on the coupling region of the waveguide, which could hinder light injection. Microscopic inspection is also carried out after trench fabrication to confirm proper detachment, and after resistor patterning to

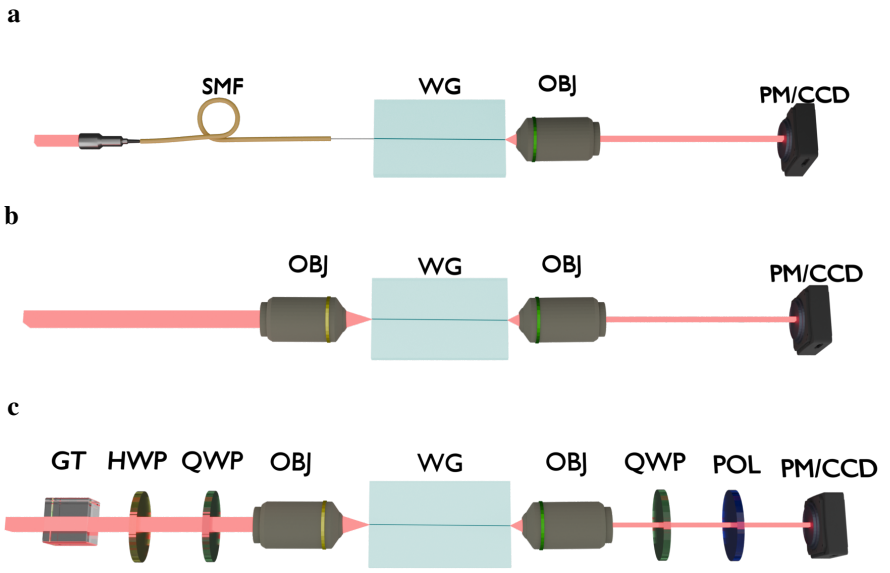

Figure 3.4: *Main configurations for waveguide characterization.* **a** *Fiber-butt coupling configuration: laser light delivered through a single-mode fibre (SMF) is coupled into the waveguide (WG), and the transmitted signal is focused by a microscope objective (OBJ) onto either a powermeter (PM) head or an imaging camera (CCD), enabling measurements of output power or inspection of the output mode profile.* **b** *End-fire coupling configuration: a free-space laser beam is coupled into the waveguide by means of an objective, while the output is collected in the same way as in the fibre-coupled case.* **c** *Polarization measurements, where a Glan–Thomson polarizer (GT), half-wave plate (HWP) and quarter-wave plate (QWP) are used at the input, while an additional QWP together with a linear polarizer (POL) are placed at the output, allowing manipulation of both input and output polarization states for polarization-dependent characterization and birefringence analysis.*

verify gold adhesion, check for the absence of interruptions in the resistors, and measure the dimensions of the final patterned structures.

3.2.2 Light coupling

To evaluate the optical properties of the fabricated PIC, laser light is injected into the waveguides at the desired operating wavelength. For this reason, the characterization laboratory is equipped with several laser sources covering both the visible and near-infrared spectral regions, including diode and solid-state lasers. Light injection into the waveguides can be performed using two main coupling configurations. The first configuration, *fiber-butt coupling*,

visible in Fig. 3.4a, consists of bringing the cleaved tip of a single-mode optical fiber, designed for the operating wavelength, into close proximity with the input facet of the waveguide. In this arrangement, coupling is typically more efficient and reproducible, making it the preferred method for quantitative measurements such as propagation loss characterization. The fiber selection should again match the modal properties of the waveguide to ensure optimal injection.

The second, known as *end-fire coupling* (Fig. 3.4b), consists of focusing the laser beam directly onto the input facet of the waveguide using a microscope objective or an aspheric lens. The selected focusing element must match both the mode field diameter and the NA of the waveguide, which is typically around 0.1 for FLM waveguides. This configuration is particularly suited for polarization-dependent measurements, as the polarization state of a free-space laser beam can be precisely controlled with polarization optics (e.g., half- and quarter-wave plates) placed before the objective. Such control is not straightforward when injecting light through a standard optical fiber. While arbitrary polarization states can in principle be prepared using fiber polarization controllers and monitored with a polarimeter, the procedure is more cumbersome and less stable than in free-space implementations. Even when polarization-maintaining fibers are used, the range of accessible polarization states remains practically constrained.

Precise and stable alignment is essential for both coupling schemes. The coupling element (objective or fiber) is mounted on a three-axis translation stage (Melles Griot NanoMax or Thorlabs MAX313D) with sub-micrometric resolution, while the sample is fixed on a four-axis micropositioner (Thorlabs MBT402D) that provides translation in the plane perpendicular to the light propagation and two-axis tilt adjustment. In fiber-butt coupling, the fiber-to-sample distance can be visually monitored with a Leica M125C bench-top microscope, offering up to 10× magnification.

At the output facet, light is collected using a higher-NA objective (0.4–0.6), to maximize light collection. The output signal is directed either to a powermeter (Ophir Nova II) for quantitative transmission measurements or to an imaging system for mode analysis. The latter employs an Edmund Optics EO-1312M CCD sensor for wavelengths below 1 μm, and a Xenics Bobcat-640

InGaAs camera for longer wavelengths.

3.2.3 Insertion Losses

Insertion losses represent one of the key figures of merit in the evaluation of waveguide performance, particularly in quantum photonics applications where minimizing loss is crucial. The overall attenuation of the optical signal propagating through an integrated device can be quantified by the *Insertion Losses (IL)*, expressed in decibels (dB) as

$$IL_{\mathrm{dB}} = -10 \log_{10}\left(\frac{P_{\mathrm{out}}}{P_{\mathrm{in}}}\right), \tag{3.2}$$

where P_{in} and P_{out} denote the optical powers injected into and collected from the device, respectively. In the case of devices featuring multiple output ports, the total output power P_{out} is obtained by summing the contributions from all ports. The Insertion losses are measured using the fiber-butt configuration depicted in 3.4a. First, the transmitted power is recorded by focusing the output light onto the power-meter head. Subsequently, the glass sample is removed, and the reference power from the fiber is measured using the same objective.

The total insertion losses of a photonic device generally arise from four distinct contributions: *Coupling Losses (CL)*, *Bending Losses (BL)*, *Fresnel Losses (FL)* and *Propagation Losses (PL)*.

Coupling Losses and mode profiling

Coupling losses originate from the mismatch between the input optical field, $E_{\mathrm{in}}(x, y)$, and the guided mode of the waveguide, $E_{\mathrm{wg}}(x, y)$. This mismatch is quantified through the overlap integral O, which represents the fraction of input power coupled into the guided mode. The expression of the overlap efficiency is

$$O = \frac{\left|\iint E_{\mathrm{wg}}(x, y)\, E_{\mathrm{in}}(x, y)\, dx\, dy\right|^2}{\left(\iint |E_{\mathrm{wg}}(x, y)|^2\, dx\, dy\right)\left(\iint |E_{\mathrm{in}}(x, y)|^2\, dx\, dy\right)}, \tag{3.3}$$

and the coupling losses in decibels are given by

$$CL_{\mathrm{dB}} = -10\,\log_{10}(O). \tag{3.4}$$

The determination of coupling losses requires an accurate evaluation of both input and output mode profiles. To this end, the output facet of the device is imaged onto a CCD or high-sensitivity camera, ensuring operation within the full dynamic range of the sensor while avoiding pixel saturation. The measured intensity distribution of the waveguide mode, $I_{\mathrm{wg}}(x, y)$, can then be used to reconstruct the spatial electric field distribution. For a waveguide operating in the single-mode regime, the field can be retrieved as

$$|E_{\mathrm{wg}}(x, y)| \propto \sqrt{I_{\mathrm{wg}}(x, y)}, \tag{3.5}$$

since the fundamental mode does not exhibit sign inversions across its profile.

To obtain the input field distribution, the device is removed from the setup, and the fiber tip is imaged directly under identical optical conditions, maintaining the same objective-detector distance to preserve magnification. Given that the fiber mode dimensions are typically well known, this procedure enables a consistent comparison between input and output profiles. Both sets of images are then post-processed numerically (e.g., via MATLAB or Python routines) to compute the overlap integral and, consequently, estimate the coupling losses.

Bending Losses

Bending losses arise when the waveguide follows a curved trajectory instead of a straight path. In this case, the guided mode $E_{\mathrm{wg}}(x, y)$ undergoes a distortion during propagation, leading to a partial coupling of optical power into radiation modes on the outer side of the bend. This phenomenon can be understood by considering the wavefront rotation along the osculating circle that locally approximates the bent section of the guide. As the distance from the center of curvature increases, the local phase velocity of the guided mode also increases, and beyond a critical distance x_r, it reaches the velocity of light in the cladding, causing the corresponding field portion to leak out as radiation.

The attenuation factor due to bending, α_B, exhibits an exponential dependence on the local radius of curvature $R(z)$ [129, 130] and can be expressed as

$$\alpha_B = \frac{a}{|R(z)|^{1/2}} \exp\Big(- b\,|R(z)|\Big), \tag{3.6}$$

where a and b are parameters that depend on the waveguide geometry and the mode profile. The total bending loss accumulated along a curved path of length l_c is then obtained by integrating the local attenuation factor:

$$BL_{\mathrm{dB}} = \int_0^{l_c} \alpha_B(z)\, dz. \tag{3.7}$$

It is evident from Eq. 3.6 that bending losses increase dramatically as the radius of curvature decreases, with stronger effects observed in weakly confined modes (i.e., in waveguides with low index contrast).

A comprehensive treatment of bending losses should also account for *transition losses*, which occur at the interface between straight and curved segments due to the shift of the guided mode towards the outer bend and the resulting index profile distortion [130].

Experimentally, bending losses are characterized by comparing straight reference waveguides with curved ones of equal total length. Assuming other loss contributions are the same across devices, the bending loss contribution per unit length can be extracted as

$$BL_{\mathrm{dB/cm}} = \frac{IL_{\mathrm{BWG}} - IL_{\mathrm{SWG}}}{l_c}, \tag{3.8}$$

where IL_{BWG} and IL_{SWG} are the measured insertion losses of a bent and a straight waveguide, respectively, and l_c is the curved path length.

Fresnel Losses

Fresnel losses originate from the discontinuity of the refractive index at the interface between the waveguide material, with refractive index n_1, and the surrounding medium, typically air, with refractive index n_2. At such interfaces, a fraction of the incident optical power is reflected, thus reducing the amount of power transmitted through the device. Under the assumption

of normal incidence and approximating the guided mode as a plane wave impinging orthogonally on the facet, the transmittance of the interface can be written as

$$T = 1 - \left(\frac{n_2 - n_1}{n_2 + n_1}\right)^2. \tag{3.9}$$

The corresponding Fresnel losses (FL) are then expressed in decibels as

$$FL_{\mathrm{dB}} = -10 \log_{10}(T). \tag{3.10}$$

In an end-fire coupling configuration, two air-glass interfaces are present (input and output facets), and therefore the Fresnel contribution must be considered twice in the total insertion losses. Conversely, in fibre butt-coupling arrangements the effect of Fresnel reflections can be strongly reduced, or even suppressed, by applying index-matching oil between the fibre tip and the glass surface, thereby eliminating the air interface and ensuring better power transmission.

Propagation Losses

Propagation losses describe the attenuation of light along the waveguide caused by intrinsic and extrinsic imperfections. In an ideal, perfectly homogeneous waveguide, the guided mode would propagate without coupling to radiative modes. In practice, however, several mechanisms contribute to power attenuation: absorption due to material impurities or intrinsic effects, Rayleigh scattering from random density fluctuations in the dielectric, and scattering induced by fabrication imperfections. The latter may originate from volume effects, such as non-uniform refractive index modifications, or surface effects, like residual roughness at the waveguide boundaries.

If the losses are uniformly distributed along the propagation direction, the transmitted optical power decays exponentially with distance:

$$P(z) = P(0)e^{-\alpha z}, \tag{3.11}$$

where $P(0)$ and $P(z)$ are the optical powers at the input and at a distance z, respectively, and α is the attenuation coefficient. After a propagation length

l, the losses can be expressed in dB/cm as

$$PL_{\mathrm{dB/cm}} = -\frac{10}{l}\log_{10}\left(\frac{P(l)}{P(0)}\right). \tag{3.12}$$

A standard method to experimentally determine the propagation losses in optical waveguides is the cut-back technique. This method consists in measuring the *IL* of a straight waveguide for several different lengths, obtained by successively cutting the same waveguide and repeating the measurement after each cut. The measured *IL* values, measured in dB, are then plotted as a function of the waveguide length, typically showing a linear relationship. A linear regression of these data provides two key parameters: the slope of the line, corresponding to the propagation loss coefficient α (in dB/cm), and the intercept at zero length, which represents the coupling plus Fresnel losses between the waveguide and the input/output fibers. This approach therefore allows for the separate accurate estimation of coupling and propagation losses in waveguides.

Alternatively, propagation losses can also be estimated indirectly from the measured *IL*, subtracting the contributions of coupling and Fresnel reflections, and normalizing over the propagation length l:

$$PL_{\mathrm{dB/cm}} = \frac{IL_{\mathrm{dB}} - CL_{\mathrm{dB}} - 2\,FL_{\mathrm{dB}}}{l}. \tag{3.13}$$

Here the Fresnel losses are counted twice, once at the input facet and once at the output facet of the waveguide.

3.2.4 Polarization and birefringence

When characterizing integrated waveguides, it is essential to investigate how the device responds to different input polarization states of light. Indeed, in some applications, such as quantum information processing where polarization encodes a qubit, the photonic circuit should ideally behave in a polarization-insensitive manner. In other contexts, however, the polarization dependence of the guided light can significantly influence device performance, for example by affecting the guided mode size, the propagation and bending losses, or the splitting ratios in directional couplers.

The polarization state of the guided beam can be conveniently described by the *Stokes vector*:

$$\mathbf{S} = \begin{pmatrix} S_0 \\ S_1 \\ S_2 \\ S_3 \end{pmatrix} = \begin{pmatrix} 1 \\ \frac{I_H - I_V}{I} \\ \frac{I_D - I_A}{I} \\ \frac{I_R - I_L}{I} \end{pmatrix}, \tag{3.14}$$

where I_i denotes the intensity measured after projection onto a given polarization basis (horizontal/vertical, diagonal/antidiagonal, right/left circular), and I is the total transmitted power.

The effect of the waveguide on the polarization state can be described by a *Müller matrix* M, relating the output and input Stokes vectors:

$$\mathbf{S}_{\text{out}} = M\,\mathbf{S}_{\text{in}}. \tag{3.15}$$

For FLM waveguides, the Müller matrix corresponds to that of a birefringent medium with a single fixed optical axis. This is because the laser-induced index modification is asymmetric, producing a well-defined linear birefringence along the propagation direction:

$$M = \begin{pmatrix} 1 & 0 & 0 & 0 \\ 0 & \cos^2 2\delta + \sin^2 2\delta \cos\phi & \sin 2\delta \cos 2\delta (1 - \cos\phi) & \sin 2\delta \sin\phi \\ 0 & \sin 2\delta \cos 2\delta (1 - \cos\phi) & \sin^2 2\delta + \cos^2 2\delta \cos\phi & -\cos 2\delta \sin\phi \\ 0 & -\sin 2\delta \sin\phi & \cos 2\delta \sin\phi & \cos\phi \end{pmatrix}, \tag{3.16}$$

where δ is the angle of the optical axis with respect to the horizontal, and ϕ is the phase delay between the ordinary and extraordinary components. The phase ϕ is related to the waveguide birefringence $\Delta n = n_e - n_o$ and its length l by

$$\phi = \frac{2\pi}{\lambda} \Delta n\, l. \tag{3.17}$$

Thus, the measurement of ϕ allows one to retrieve the birefringence of the

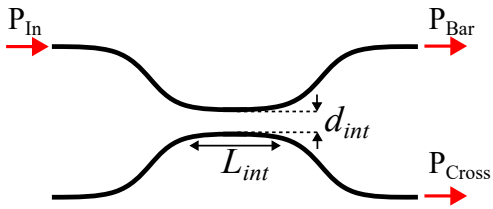

Figure 3.5: *Schematic representation of a directional coupler. Two waveguides, initially separated, are brought closer together to a spacing of d_{int} through S-shaped curved sections. They remain in close proximity and interact over a coupling length L_{int}, after which they are gradually separated again.*

waveguide and the corresponding rotation induced on the polarization state.

This characterization is experimentally implemented by the optical setup sketched in Fig. 3.4c. The input beam first passes through a Glan–Thompson polarizer, which ensures a well-defined horizontal polarization. A half-wave plate (HWP) and a quarter-wave plate (QWP), mounted on motorized stages, are then used to prepare an arbitrary input polarization state that is coupled into the waveguide. At the output facet, the emerging light passes through a second quarter-wave plate followed by a linear polarizer, enabling projective measurements of the output Stokes vector. By fitting the measured $\mathbf{S}_{\text{out}}$ to Eq. 3.15, both the birefringence Δn and the optical axis orientation δ can be retrieved. To remove ambiguities due to the 2π periodicity of the phase ϕ, the same measurement should be repeated for waveguides of different lengths.

3.2.5 Directional coupler characterization

The operation of directional couplers is based on the evanescent coupling of the optical modes supported by two adjacent waveguides. The theoretical description of this effect has already been presented in Chapter 1 within the framework of coupled-mode theory. For two identical waveguides interacting over a length L_{int}, the transmission T (or splitting ratio) can be expressed as

$$T(L) = \sin^2(kL_{int} + \phi), \tag{3.18}$$

where k is the coupling coefficient and ϕ accounts for the interaction that already occurs in the bent approach regions. The coupling coefficient is proportional to the overlap between the two guided modes,

$$k \propto \iint E_1(x,y)\, E_2(x,y)\, dx\, dy, \tag{3.19}$$

and, in practice, its dependence on the interaction distance d can be empirically described as

$$k(d) = a\, e^{-bd}, \tag{3.20}$$

with a and b constants determined by parameters such as the index contrast and the wavelength.

In FLM waveguides, an accurate analytical modelling is complicated by the weak confinement and the nontrivial mode profile. Moreover, coupling already takes place in the curved regions preceding the straight interaction section, further limiting the accuracy of theoretical predictions. For this reason, the design of a compact directional coupler is therefore based on exploiting the evanescent coupling occurring in the curved approach regions, by setting the straight interaction length to $L = 0$. In this case, the main design parameter is the interaction distance d, while the bending radius of the curved sections is chosen as a compromise between reducing bending losses and keeping the device footprint small. The characterization is carried out by fabricating a series of couplers with different values of d and no straight interaction region. Light is injected into one input arm, and the output powers at the bar port (P_{bar}) and cross port (P_{cross}) are recorded, where bar port refers to the case in which light exits from the same arm where the light is injected while cross port corresponds to the opposite arm (see Fig. 3.5). The transmission is then defined as

$$T(d) = \frac{P_{\text{bar}}}{P_{\text{bar}} + P_{\text{cross}}}, \tag{3.21}$$

and the corresponding coupling coefficient k is extracted by fitting the experimental transmission data assuming the functional dependence given by Eq. 3.20. The fitting procedure is carried out by numerically solving the coupled mode equations (Eq. 1.14) and iteratively adjusting the parameters a and b until the simulated transmission curve best reproduces the measured one. The entire procedure is implemented via a custom Matlab script. In

this way, the functional dependence $k(d)$ can be reconstructed, providing a direct means of selecting the optimal interaction distance for achieving a target splitting ratio.

3.2.6 Reconfigurability

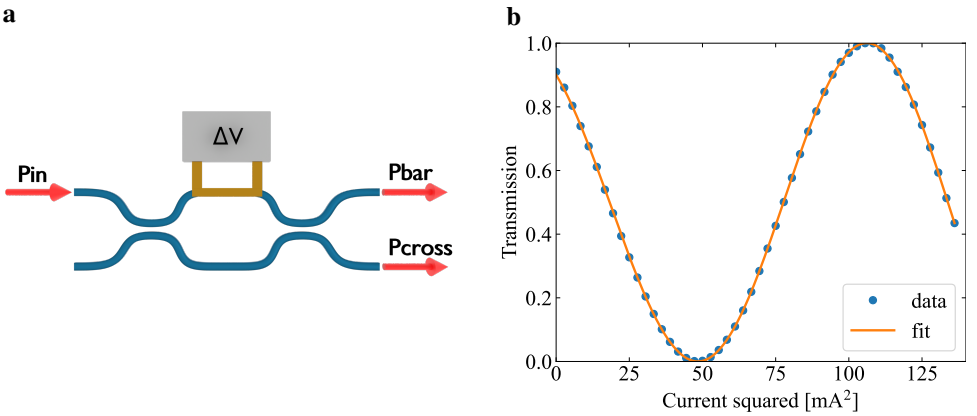

Figure 3.6: **a** *Schematic of a MZI consisting of two balanced directional couplers, with a resistive heater on top of one arm for thermal phase shifting.* **b** *Measured transmission at the bar port (P_{bar}) as a function of the dissipated power, showing the sinusoidal modulation induced by the thermo-optic phase shift.*

Thermal phase shifters are first electrically tested by measuring the resistance R of the fabricated heaters with a digital multimeter. The optical response is then investigated by injecting light into the circuit and recording the output power distribution while gradually tuning the voltage or current applied to the resistor.

A clear example of this procedure is provided by a MZI composed of two balanced directional couplers, where a resistive heater is patterned on top of one arm (see Fig. 3.6a). In this configuration, the heater changes the relative phase between the interferometer arms, producing a sinusoidal oscillation of the output transmission (P_{bar}) with the dissipated power (Fig. 3.6b). This behaviour can be described as

$$P_{bar}(\Delta\phi) = \sin^2\left(\frac{\Delta\phi}{2}\right), \tag{3.22}$$

where the phase shift depends linearly on the dissipated power P_{diss}:

$$\Delta\phi = \alpha\, P_{\text{diss}} + \Delta\phi_0. \tag{3.23}$$

The proportionality constant α is determined by the light wavelength λ, the thermo-optic coefficient of glass ($n_T \sim 10^{-5}\,\text{K}^{-1}$), the thermal conductivity ($k \approx 0.9\,\text{W}/(\text{m}\cdot\text{K})$), and by the relative distances r_1 and r_2 between the heater and the two arms of the MZI [97]:

$$\alpha = \frac{2n_T}{\lambda k}\,\ln\!\left(\frac{r_1}{r_2}\right). \tag{3.24}$$

The dissipated power can be expressed as $P_{\text{diss}} = V^2/R$ when operating under voltage control, or as $P_{\text{diss}} = RI^2$ under current control. In this way, the required driving conditions for inducing a desired phase shift can be readily evaluated.

When multiple heaters are present on the same device, Eq. 3.23 generalizes to a matrix form, since each waveguide phase can be affected by all resistors. The off-diagonal elements represent cross-talk contributions, i.e. the effect of a heater on neighbouring arms. Although insulating trenches substantially reduce these terms, they must still be taken into account for correct device operation. In practice, the characterization involves measuring the full set of induced phase shifts for each resistor, thereby reconstructing the linear system. While cross-talk is not inherently detrimental and can be compensated once characterized, an increasing number of heaters makes the calibration process more time-consuming. Moreover, excessive cross-talk may lead to higher power consumption to achieve the desired reconfigurability.

CHAPTER 4

Photonics devices for secure communication systems

In this chapter, we present two research works concerning the realization of integrated photonic devices for quantum communication. The first project was carried out in collaboration with the groups of Prof. Zbinden and Prof. Thew at the University of Geneva, and focuses on the real-world implementation of a time-bin quantum key distribution system. My contribution to this work concerned the fabrication and characterization of an unbalanced Mach–Zehnder interferometer, employed as the time-bin receiver of the QKD setup. The second project was developed in collaboration with the group of Prof. Villoresi at the University of Padova, and involves the realization of a high-performance heterodyne receiver for continuous-variable quantum random number generation and continuous-variable quantum key distribution. In this case, I contributed to the fabrication and characterization of the integrated tunable optical hybrid used in the receiver. The results of this work have been published on arXiv [131] and are currently under peer review.

4.1 Integrated Time-bin receiver for high-speed integrated QKD system

4.1.1 Motivation

As mentioned in Section 1.2.2, the rapid progress of quantum technologies, together with the looming threat of quantum computers to classical cryptography, has made QKD a cornerstone for future secure communications. For practical adoption, QKD systems must be compact, robust, and seamlessly integrable into telecommunication networks. Building on the work of Sax *et al.* [132], who demonstrated an integrated-photonics-based QKD system based on time-bin qubits, the underlying idea is to advance this approach toward prototypes suitable for field deployment. In this context, the receiver plays a central role, as it must combine low optical losses with stable operation under varying conditions. The receiver is realized using FLM in borosilicate glass, with waveguides specifically designed for operation at the telecom wavelength of 1550 nm.

This platform was chosen for its low insertion losses and intrinsic polarization insensitivity. The latter feature is particularly important in our protocol, since photon transmission occurs through optical fiber links. In such fibers, the polarization state of light undergoes random fluctuations due to birefringence, leading to an unpredictable polarization at the receiver. Instead of introducing additional polarizing filters, which would increase system losses, or relying on active polarization compensation, which would complicate the setup, we have engineered the device using FLM to be intrinsically polarization-insensitive. In this platform, directional couplers exhibit polarization-independent splitting ratios, while the residual birefringence is extremely small and, importantly, tunable. It can be adjusted dynamically via temperature or permanently through the inscription of stress tracks, providing a level of control and flexibility not available in other technologies. FLM waveguides also ensure efficient fiber coupling and low propagation losses, enabling the realization of compact and low-loss integrated circuits.

The implemented PIC also incorporates a tunable beam splitter for basis selection, providing adaptability in heterogeneous network scenarios and op-

timization for each transmission distance. Electronic control of the splitting ratio allows the receiver to compensate for different link conditions without hardware modifications and to maintain optimal performance over time, even in the presence of fiber aging or environmental fluctuations. From a manufacturing perspective, this tunability reduces the need for calibration or customization, thereby supporting scalable and cost-effective deployment. Finally, the monolithic nature of glass-based PICs ensures mechanical stability and thermal tolerance, all critical for operation in field environments with limited environmental control.

4.1.2 One-Decoy Three-State BB84 Protocol

The implemented protocol is a three-state BB84 scheme with time-bin encoding and the one-decoy method [133]. In time-bin encoding, the qubit information is carried by the photon arrival time, where the logical states are defined by two well-separated temporal modes, denoted as early (E) and late (L) time bins. In the Z basis, used for raw key generation, Alice encodes bits 0 and 1 as $|0\rangle = |\alpha\rangle_E|0\rangle_L$ and $|1\rangle = |0\rangle_E|\alpha\rangle_L$, respectively, where $|\alpha\rangle$ represents a weak coherent state. In the X basis, employed solely for security estimation, she prepares the superposition state $|+\rangle = \frac{1}{\sqrt{2}}(|0\rangle + |1\rangle)$, (see Fig. 4.1a). Since weak coherent pulses are used, the one-decoy method is adopted to counter photon-number-splitting attacks: the mean photon number is randomly varied between two levels, μ_1 (signal) and μ_2 (decoy).

At the receiver side, Bob measures each qubit in either the Z or X basis, (see Fig. 4.1a). In the Z basis, time-of-arrival detection directly yields the key bits. In the X basis, an unbalanced MZI with the same delay as Alice's interferes the early and late modes. Its relative phase is actively stabilized via a feedback loop, ensuring destructive interference at the monitored output port, where detections in the central time bin correspond to the projection onto $|-\rangle = \frac{1}{\sqrt{2}}(|0\rangle - |1\rangle)$. The complementary port, carrying $|+\rangle$, is not monitored. In the absence of eavesdropping, high-visibility interference gives predictable outcomes, while any disturbance reduces visibility and increases the error rate, providing a direct estimate of Eve's information.

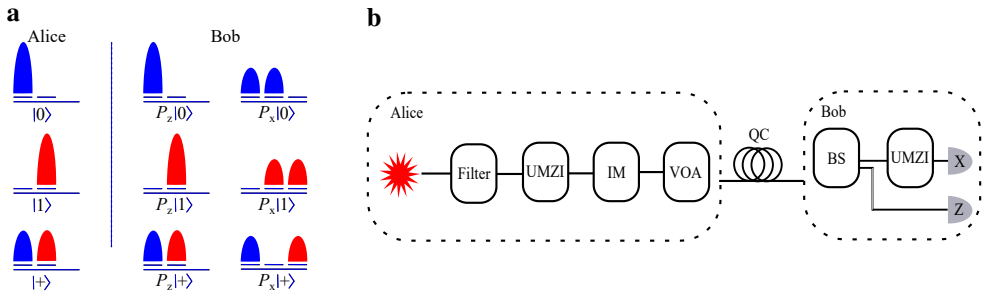

Figure 4.1: **a** *Encoding of the states generated by Alice and measured by Bob in the time-bin protocol, after projection onto the Z or X basis. Figure adapted from [134].* **b** *Schematic of the experimental QKD setup. On Alice's side, laser pulses are filtered, time-bin qubits are generated by an unbalanced MZI (UMZI), encoded with an intensity modulator (IM), and attenuated with a Variable Optical Attenuator (VOA). On Bob's side, a reconfigurable MZI directs one port to Z-basis detection and the other to a UMZI for X-basis projection.*

Experimental setup

The experimental setup is depicted in Figure 4.1b. The system builds on the PIC-based QKD architecture of Sax *et al.* [132], with improvements in stability and performance. By operating at 1.25 GHz instead of 2.5 GHz, the time-bin duration is doubled (400 ps vs. 200 ps), mitigating chromatic dispersion and detector jitter while enhancing state fidelity. The transmitter (Alice) is implemented in silicon photonics, primarily chosen for its capability to support high-speed modulation, making it well suited for high-speed state generation. Furthermore, this platform enables the dense integration of active and passive components within a compact footprint. The optical signal is generated through a sequence of functional blocks: a filter narrows the laser linewidth, an unbalanced MZI creates the time-bin qubits, an intensity modulator encodes the states at high speed, and a variable optical attenuator sets the photon number per pulse. All of these devices are integrated into a single PIC, fabricated using standard silicon photonic technology and designed by Sicoya GmbH. All driving electronics, including clock generation, RF signal distribution, laser control, power supplies, and thermal regulation, are consolidated into a single PCB, further reducing footprint and enhancing stability. The receiver (Bob), as mentioned before, is instead realized in FLM, chosen for its low losses and polarization insensitivity. At its input, a

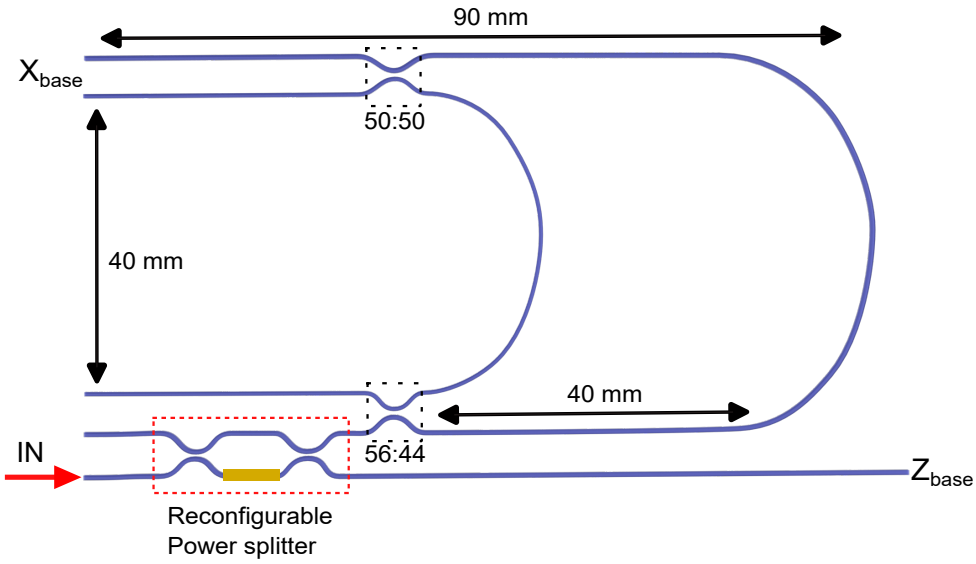

Figure 4.2: *Scheme of the time-bin QKD receiver (not to scale). A reconfigurable MZI acts as a power splitter, sending one output directly to the Z-basis port and the other to an unbalanced MZI (UMZI) for the X-basis measurement. The UMZI, designed in a trombone-like geometry, includes two straight sections of* 40 *mm each, providing a total delay path length of about* 80 *mm, corresponding to a temporal delay of approximately* 400 *ps in borosilicate glass. To maintain high interference visibility, the first coupler of the UMZI is intentionally unbalanced to compensate for the propagation losses in the longer arm, thus ensuring power balance at the second coupler. Only one of the two UMZI outputs is employed during the QKD protocol. The total footprint of the device is approximately* 40×90 mm^2

tunable MZI, with adjustable splitting ratio to match different link lengths, route the amount of photons either to the Z basis for direct detection or to the X basis, where the unbalanced interferometer performs the coherence measurement. Since the receiver constitutes the core subject of this thesis and the main focus of my work, its design and fabrication will be discussed in detail in the following section.

4.1.3 Design of the time-bin QKD receiver

The design of the FLM receiver is shown in Fig. 4.2. The input signal first encounters a reconfigurable MZI, which allows the user to optimize the splitting ratio depending on the link length. To ensure full reconfigurability in a balanced MZI, both DCs are implemented with a 50:50 splitting ratio.

One output of the MZI is routed through a straight waveguide to perform the projection onto the Z basis, while the other output is directed into an unbalanced MZI (UMZI), which implements the projection onto the X basis.

This layout enables the temporal recombination of two consecutive pulses. The delay length is mainly defined by two straight sections of approximately 4 cm each, leading to a total imbalance of about 8 cm. This corresponds to a temporal delay of roughly 400 ps for a photon propagating in borosilicate glass, where the additional length due to the larger bending radius of the second arm is also taken into account.

It is important to note that an error tolerance of ±1 ps, as specified by the Geneva group, is sufficient to guarantee high interference visibility. Since 1 ps in glass corresponds to approximately 0.2 mm, this tolerance is much larger than the sub-nanometer writing precision achievable with FLM.

Another key aspect of the UMZI design is the additional propagation loss introduced by the longer arm, which, if uncompensated, could reduce the interferometer visibility. As shown in Fig. 4.2, this effect is mitigated by using an unbalanced first coupler. The additional loss accumulated by the longer arm can be estimated as $L_{\text{add}} = \alpha \cdot \Delta L \quad [\text{dB}]$, where α is the propagation loss coefficient in dB/cm, and ΔL is the path-length imbalance expressed in cm.

To compensate for these losses and balance the powers at the second coupler, the splitting ratio of the first coupler must satisfy

$$\text{BAR} = \frac{1}{1 + L_{\text{long}}}, \tag{4.1a}$$

$$\text{CROSS} = \frac{L_{\text{long}}}{1 + L_{\text{long}}}, \tag{4.1b}$$

with $L_{\text{long}} = 10^{-\frac{L_{\text{add}}}{10}}$.

Finally, the separation between adjacent waveguides is 127 μm, matching the pitch of a standard fiber array. The overall footprint of the optical circuit is approximately 40×90 mm^2.

4.1.4 Unbalanced MZI visibility

Obtaining an interferometer with high visibility is a fundamental requirement for the correct operation of the device, and therefore this aspect deserves a detailed discussion. Interference with high visibility requires indistinguishability across all relevant degrees of freedom. In the present integrated device, once temporal alignment is ensured and spectral/spatial-mode mismatch is negligible (identical single-mode waveguides and a narrow-linewidth common laser), the dominant factors that determine the visibility are: (i) the differential propagation losses between the two arms and (ii) the polarization mismatch. In what follows, we first derive the loss-compensation condition that equalizes the field amplitudes at the recombination stage; we then address polarization control and its impact on the interferometric visibility.

Unbalanced coupler for loss compensation

To this end, we model the UMZI as the cascade of an unbalanced input coupler, a lossy arm with also the phase term, and a 50:50 recombining coupler. In this representation, the input coupler has amplitude transmission $\sqrt{\varepsilon}$ and reflection $i\sqrt{1-\varepsilon}$, while the longer arm imparts an amplitude factor α and a relative phase ϕ. The building blocks read

$$\begin{aligned} H(\phi,\varepsilon) &= \frac{1}{\sqrt{2}}\begin{bmatrix} 1 & i \\ i & 1 \end{bmatrix}\begin{bmatrix} \alpha e^{i\phi} & 0 \\ 0 & 1 \end{bmatrix}\begin{bmatrix} \sqrt{\varepsilon} & i\sqrt{1-\varepsilon} \\ i\sqrt{1-\varepsilon} & \sqrt{\varepsilon} \end{bmatrix} \\ &= \frac{1}{\sqrt{2}}\begin{bmatrix} \alpha e^{i\phi}\sqrt{\varepsilon} - \sqrt{1-\varepsilon} & i\left(\alpha e^{i\phi}\sqrt{1-\varepsilon} + \sqrt{\varepsilon}\right) \\ i\left(\alpha e^{i\phi}\sqrt{\varepsilon} + \sqrt{1-\varepsilon}\right) & -\alpha e^{i\phi}\sqrt{1-\varepsilon} + \sqrt{\varepsilon} \end{bmatrix}. \end{aligned} \tag{4.2}$$

To equalize the amplitudes at the input of the second coupler (independently of ϕ), we require $\alpha\sqrt{\varepsilon} = \sqrt{1-\varepsilon}$, which gives

$$\boxed{\varepsilon_{\text{opt}} = \frac{1}{1+\alpha^2}}. \tag{4.3}$$

With this choice, $\sqrt{\varepsilon_{\text{opt}}} = \dfrac{1}{\sqrt{1+\alpha^2}}$ and $\sqrt{1-\varepsilon_{\text{opt}}} = \dfrac{\alpha}{\sqrt{1+\alpha^2}}$, thereby recovering (4.1). Substituting into H we obtain

$$H(\phi, \varepsilon_{\text{opt}}) = \frac{1}{\sqrt{2(1+\alpha^2)}} \begin{bmatrix} \alpha\left(e^{i\phi}-1\right) & i\left(1+\alpha^2 e^{i\phi}\right) \\ i\,\alpha\left(1+e^{i\phi}\right) & 1-\alpha^2 e^{i\phi} \end{bmatrix}. \tag{4.4}$$

For an input $\mathbf{E}_{\text{in}} = [1,0]^T$ the output fields are the first column of H.

$$H(0, \varepsilon_{\text{opt}}) = \frac{1}{\sqrt{2(1+\alpha^2)}} \begin{bmatrix} 0 & i(1+\alpha^2) \\ i\,2\alpha & 1-\alpha^2 \end{bmatrix}, \tag{4.5}$$

$$H(\pi, \varepsilon_{\text{opt}}) = \frac{1}{\sqrt{2(1+\alpha^2)}} \begin{bmatrix} -2\alpha & i(1-\alpha^2) \\ 0 & 1+\alpha^2 \end{bmatrix}. \tag{4.6}$$

Hence the dark port swaps between the two outputs when the phase shifts from 0 to π, and both outputs exhibit unit visibility (complementary fringes) while the total signal level is reduced by losses. It is worth noting that, when exciting the other input port, the configuration $\varepsilon = \varepsilon_{\text{opt}}$ no longer balances the amplitudes: this is effectively equivalent to injecting with a non-compensated split, in this case, the (maximum) visibility is no longer unitary but becomes

$$V_{\text{in}\,2} = \frac{2\alpha^2}{1+\alpha^4} \;<\; 1 \qquad (\alpha < 1). \tag{4.7}$$

Polarization alignment

The second important contribution to visibility reduction is the polarization mismatch. As introduced in Sec. 2.3, FLM waveguides exhibit low but non-vanishing birefringence, typically $\Delta n \sim 10^{-5}$–10^{-6}, mainly due to a slight core-shape anisotropy elongated along the focusing writing laser. This can be modeled as a uniaxial medium whose optical axis is perpendicular to the scan direction. If considering input light with a general polarization state (not necessarily aligned to the waveguide optical axis), when both arms are equalized in length, the induced polarization rotation is nominally identical; however, with an imbalance of about 8 cm, the two pulses accumulate different polarization transformations and a polarization mismatch may arise, thus

reducing interference visibility at the UMZI output.

Let n_o and n_e denote the ordinary and extraordinary refractive indices, and define the birefringence $\Delta n = n_e - n_o$. The phase accumulated by the two polarization modes over a length L_k in arm k is

$$\phi_{o,k} = \frac{2\pi}{\lambda} n_o L_k, \qquad \phi_{e,k} = \frac{2\pi}{\lambda} n_e L_k, \tag{4.8}$$

so that each arm acts as a linear retarder with retardance

$$\delta_k \;=\; \phi_{e,k} - \phi_{o,k} \;=\; \frac{2\pi}{\lambda}\,\Delta n\, L_k. \tag{4.9}$$

The differential birefringent retardance at recombination is

$$\Delta\delta \;=\; \delta_2 - \delta_1 \;=\; \frac{2\pi}{\lambda}\,\Delta n\,(L_2 - L_1) \;=\; \frac{2\pi}{\lambda}\,\Delta n\,\Delta L. \tag{4.10}$$

For high-visibility interference, both arms must realize the same polarization transformation. In the worst-case input (linear polarization at 45° to the birefringence axes), the probability of finding the output in the same polarization as the input is

$$P_{\text{same}} = \Big|\langle + |\; U(\Delta\delta)\; | + \rangle\Big|^2 = \frac{1 + \cos\Delta\delta}{2} = \cos^2\!\left(\frac{\Delta\delta}{2}\right). \tag{4.11}$$

Thus, unit visibility is obtained whenever the differential retardance is an integer multiple of 2π:

$$\boxed{\Delta\delta \;=\; 2\pi m, \quad m \in \mathbb{Z}} \quad\Longleftrightarrow\quad \Delta n \;=\; m\,\frac{\lambda}{\Delta L}. \tag{4.12}$$

This condition ensures that both arms impart identical polarization transformations. Even small birefringence can therefore impact visibility over an 8 cm imbalance. Since ΔL is fixed by design, Eq. (4.12) shows that achieving $\Delta\delta = 2\pi m$ implies adjusting the effective birefringence Δn; practical strategies to do so are discussed in the next section.

4.1.5 Tuning of birefringence

An important feature of FLM waveguides is that their birefringence can be trimmed after inscription by writing auxiliary stress-inducing tracks in the cladding near the core with the same femtosecond laser [135–137], as illustrated in Figure 4.3. The stress field modifies the refractive indices through the elasto–optic effect. From a design standpoint it is crucial to place the stress track aligned with one of the birefringence principal axes of the waveguide, so as not to induce unwanted rotation of the optical axes. In addition, the track must be written far enough from the core and with calibrated pulse energy/scan speed to avoid extra propagation loss, while still producing the desired retardance change. The effect of stress tracks on waveguide birefringence is strongly material dependent. In our case, for waveguides inscribed in EAGLE XG® glass, we verified that a track written above or below the core reinforces the native anisotropy, increasing $|\Delta n|$. Conversely, lateral tracks tend to reduce $|\Delta n|$. This means that the strategy of stress-track inscription allows for bi-directional phase mismatch compensation, allowing to both increase or decrease the value of $\Delta\delta$ according to the needs. However, lateral trimming is more challenging, as it requires careful control not only of the lateral distance but also of the depth, to avoid axis rotation. In contrast, top/bottom trimming is generally easier to implement, since it only requires proper alignment with the waveguide and an appropriate vertical spacing, while perturbing the same symmetry plane that defines the original axes.

Besides fabrication-induced anisotropy, it has been observed that birefringence does also exhibit a dependence on temperature, since the thermo-optic response of the material may affect ordinary and extraordinary optical axes differently. In EAGLE XG® glass, a decrease of the birefringence with increasing temperature has been observed. Although typically a weaker effect compared to stress-induced contributions, this dependence can be exploited as a fine-tuning mechanism. In practice, by slightly varying the operating temperature of the circuit, the accumulated phase mismatch over the interferometer imbalance can be adjusted, thus improving interference visibility. Also in this case, bi-directional tunability is allowed by either heating or

cooling the circuit with respect to room-temperature conditions.

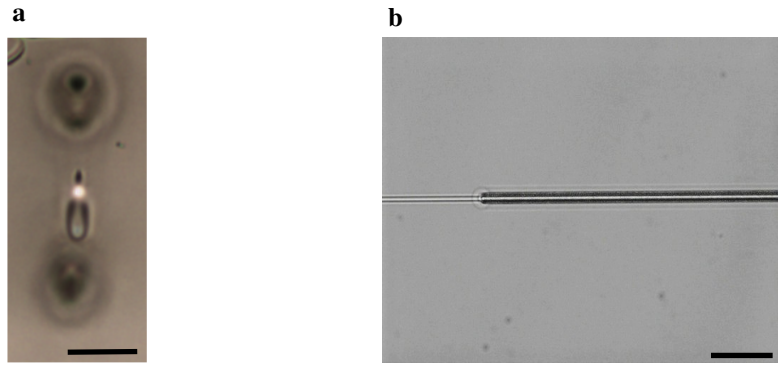

Figure 4.3: *Microphotograph of the stress track.* **a** *Cross-section showing the waveguide with the top and bottom stress tracks.* **b** *Top view of the waveguide and stress track. Scale bar:* 20 μm.

4.1.6 Fabrication and characterization of the device

Waveguides optimization

The optimization of the fabrication process was carried out by scanning the main inscription parameters to identify the combination that minimizes the overall circuit losses. In particular, the geometry of the inscribed waveguides was chosen to reproduce that of the final device, allowing a direct estimate of the expected insertion loss, which is the most relevant parameter. The optimization involved the inscription of several straight waveguides as well as concentric U-bends, while varying parameters such as the translation velocity (5, 7, and 9 mm/s) and the laser power (from 480 to 520 mW in 20 mW steps). Each U-bend is formed by 1 cm of straight waveguide, a semicircular bend with the indicated radius, and another 1 cm straight section, with input and output on the same side of the chip. The results are reported in Figure 4.4. Given the particular layout, we investigated the differences between waveguides inscribed in the forward and backward directions (Fig. 4.4a and 4.4b, respectively), arising from the quill effect [79]. Furthermore, tests were performed for bending radii between 22 and 15 mm to assess the robustness of the parameters across different geometries (see Fig. 4.4c). Waveguides were inscribed 50 μm beneath the surface of a 1 mm-thick alumino-borosilicate

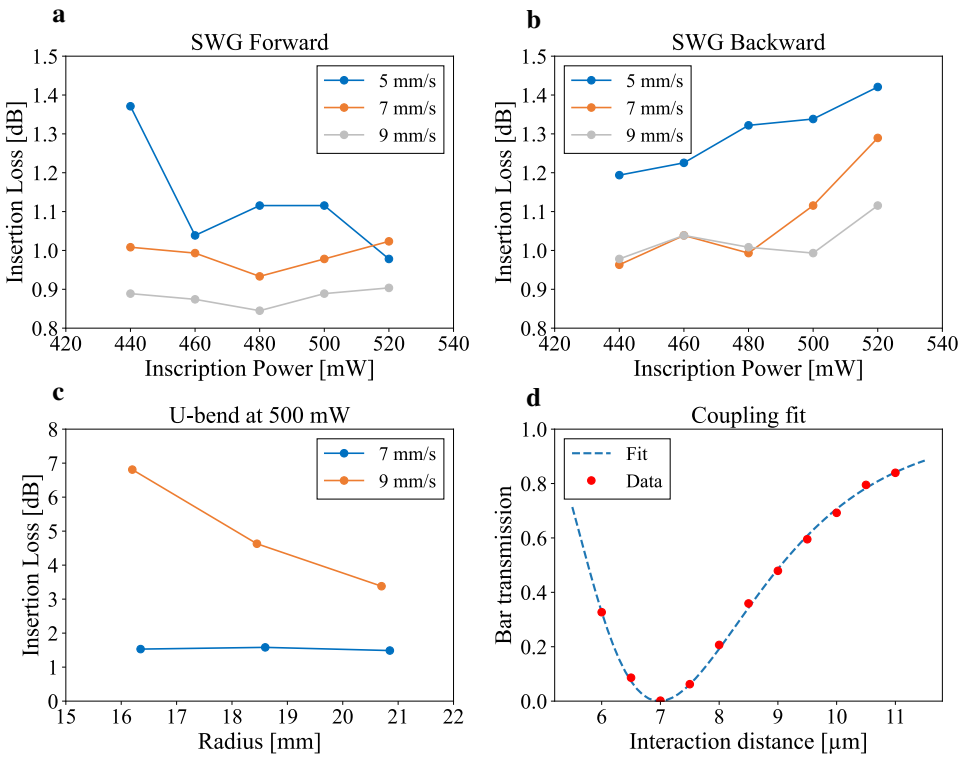

Figure 4.4: *Waveguide optimization.* **a** *and* **b** *Insertion losses (IL) of straight waveguides (SWG) inscribed in the forward and backward directions, respectively, as a function of the inscription power, for different translation velocities, measured over a sample length of 5 cm.* **c** *Insertion losses of U-bend waveguides at 500 mW, identified as the optimal power for this geometry since it provided the most robust performance with lower losses compared to other tested powers, plotted as a function of the bending radius.* **d** *Optimization of the DC, reporting the normalized bar transmission as a function of the interaction distance.*

glass substrate (EAGLE XG®). The process was carried out using a Pharos femtosecond laser system (repetition rate 1 MHz, wavelength 1030 nm), focused through a 0.5 NA water-immersion microscope objective. Among the tested conditions, the U-bend measurements indicated that a laser power of 500 mW produced the most robust structures, with lower insertion losses than at other powers (Fig. 4.4c), thus representing the best optical performance. Using these optimized parameters, pulse energy of 500 nJ, translation speed of 7 mm/s, and four consecutive scans, straight waveguides exhibited insertion losses of about 1 dB over a 5 cm length, with a mode-field size of $7.4 \times 7.6\ \mu m^2$. The waveguides were subsequently thermally annealed, as described in Sect. 3.1. We then investigated the evanescent coupling between adjacent waveguides to determine the optimal geometry for directional couplers capable of achieving the desired splitting ratios. To minimize the footprint of the circuit, the study was restricted to couplers with $L_C = 0$, thus exploiting the evanescent interaction within the S-bends. To identify the separation ensuring a balanced splitting, several directional couplers with different interaction lengths were fabricated and their reflectivities measured (Fig. 4.4d). By fitting the experimental data, the optimal coupling distance for a 50:50 coupler was found to be $d = 9.1\ \mu m$. For the unbalanced coupler, after estimating a propagation loss of about 0.14 dB/cm from previous optimizations, the splitting ratio, calculated using (4.1a), was found to be 56:44, corresponding to an interaction length of $d = 9.25\ \mu m$.

Stress-track optimization

To optimize the stress-track parameters, we systematically investigated the influence of several inscription settings, including scan velocity (0.5 and 1 mm/s), writing power (300 and 500 mW), pulse duration (180 fs, 1 ps, 2 ps), and the relative distance of the track from the top and bottom of the waveguide (ranging from 23 to 37 μm). The final optimized recipe was found to be: scan velocity of 0.5 mm/s, power of 500 mW, pulse duration of 2 ps, with the stress track positioned at 33 μm below and 25 μm above the waveguide. This configuration was selected to maximize the birefringence modification while avoiding additional propagation losses. Figure 4.5 shows the measured insertion losses as a function of the distance of the lower stress track from

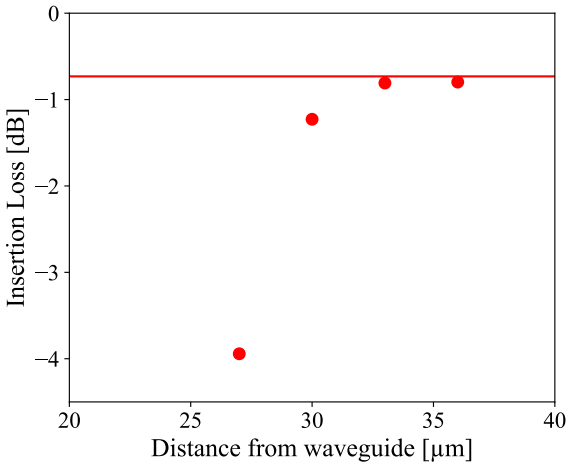

Figure 4.5: *Insertion losses of a waveguide with stress tracks inscribed beneath it, shown as a function of the vertical distance between the track and the waveguide. The red line represents the reference waveguide without a stress track, highlighting the additional losses induced by the track.*

the waveguide, highlighting the trade-off between induced birefringence and optical loss.

To calibrate the contribution of stress tracks to birefringence tuning, we first measured the intrinsic birefringence of reference waveguides (without stress track) using the method described in Sec. 3.2.4. We then inscribed bottom and top tracks using the optimized recipe, and re-measured the birefringence. Both 1 cm and 2 cm long stress tracks were tested, and the birefringence was compared before and after inscription. The total waveguide length is 8 cm, matching the unbalance length, which allows a direct comparison of the induced phase shift. The modification can be interpreted as an average birefringence over stressed and unstressed regions.

The results, summarized in Table 4.1, show that both top and bottom tracks lead to a noticeable increase in birefringence. In particular, the top tracks correspond to an average induced phase shift exceeding 2.27 rad/cm. While exact quantification is limited by fabrication tolerances, the practical goal is to achieve a net dephasing close to a multiple of 2π, leaving only fine tuning to be performed via temperature control.

	Before stress track	After bottom track	After top track
Waveguide 1 (1 cm)	Phase: 2.15 rad $\Delta n = 2.34 \times 10^{-5}$	Phase: 2.50 rad $\Delta n = 2.44 \times 10^{-5}$	Phase: 4.89 rad $\Delta n = 3.08 \times 10^{-5}$
Waveguide 2 (2 cm)	Phase: 2.32 rad $\Delta n = 2.38 \times 10^{-5}$	Phase: 2.74 rad $\Delta n = 2.50 \times 10^{-5}$	Phase: 7.17 rad $\Delta n = 3.73 \times 10^{-5}$

Table 4.1: *Measured birefringence and phase before and after stress track inscription. Waveguide 1 corresponds to a 1 cm track, while Waveguide 2 corresponds to a 2 cm track. For each case, the effect of bottom and top tracks is reported separately.*

Realization of the final device

After optimizing the design and inscription parameters, the full optical circuit was fabricated according to the scheme in Fig. 4.2. To match as closely as possible Alice's delay of 406.3 ps, three sets of devices were inscribed with straight path lengths of 40.038 mm and ±0.1 mm. The average delay length was chosen on the basis of preliminary measurements carried out in Geneva on earlier fabricated devices. Thanks to the three-dimensional capabilities of FLM, the different devices could be written concentrically, one inside the other, thereby fitting multiple layouts in the same substrate. Within each set, three additional devices were written with slightly different interaction distances for the unbalanced directional coupler, enabling precise tuning of the splitting ratio and an effective balancing of the losses between the interferometer arms. Preliminary characterization in Geneva confirmed the accuracy of the fabrication: for the group designed with 40.038 mm, the measured delay was 405.96 ps, only 0.34 ps different from Alice. The birefringence of the waveguides was then measured, together with the visibility.

It is worth noting that visibility was characterized using different input polarizations. When injecting purely horizontal or vertical polarization, the measurement primarily probes the compensation of losses introduced by the unbalanced coupler. In this case, since H and V polarizations propagate along a single birefringence axis and are not affected by polarization transformations, we measured visibilities exceeding 99% for both polarizations in the group of interest. This value represents the upper limit achievable once loss compensation is optimized. Conversely, injecting light polarized at 45° with respect to the birefringence axes provides the worst-case scenario, as it

is maximally sensitive to phase delays between the polarization components. To ensure true polarization insensitivity, birefringence must be tuned on the basis of this measurement. By inverting Eq. (4.11), we estimated the residual phase mismatch and determined the required stress track length to correct it. Stress tracks were then inscribed on a straight section of the longer arm, specifically in the group of devices with the smallest delay mismatch with Alice. After this correction, the visibility measured with 45° input polarization exceeded 96% across all three devices. The results before and after stress-track inscription are summarized in Table 4.2.

	Visibility before	**Stress track compensation**	**Visibility after**
Device 1	45.0%	2.1 cm (264°)	98.4%
Device 2	37.7%	2.0 cm (258°)	96.8%
Device 3	62.8%	2.2 cm (282°)	98.8%

Table 4.2: *Measured visibility before and after stress-track inscription entering with polarized light at 45°. Values in brackets indicate the estimated phase-compensation degree.*

Once the optical performance was verified, two TOPSs were fabricated on the balanced MZI, providing redundancy although only one is required for operation. The fabrication procedure followed the same approach described in Sec. 3.1.3, with the only difference that no trenches were inscribed. Since only a single resistor is used at a time, issues such as cross-talk or excessive power dissipation are not relevant in this case. In this configuration, a 2π phase shift was achieved with a driving power of 500 mW. The insertion losses were measured to be 3.2 dB for the X arm and 1.5 dB for the Z arm, measured by switching all the optical power into one path at a time using the thermo-optic phase shifters. Finally, the chip was pigtailed and mounted inside a custom aluminum housing, equipped with a Peltier element for active thermal control. The design was specifically conceived to ensure optimal temperature stabilization, which is essential for stable operation, particularly in the unbalanced section of the interferometer. A photograph of the final assembly is shown in Fig. 4.6.

The device was then brought to Geneva, where the birefringence was fine-tuned by adjusting the temperature, and the visibility was characterized as a function of temperature. A maximum visibility of 99.73% was achieved at 14.2°C. The device is currently still installed in Geneva as part of the complete

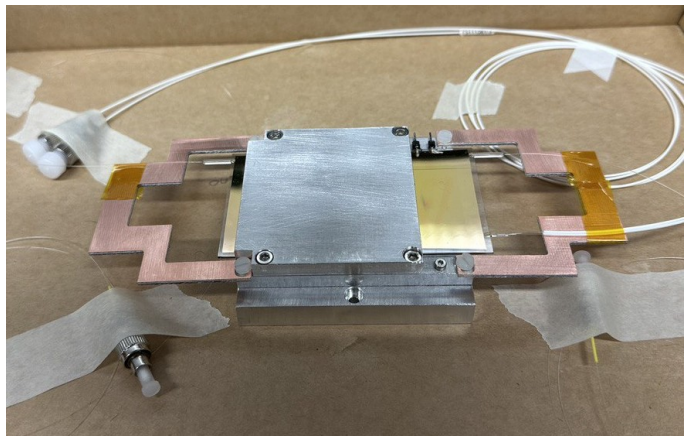

Figure 4.6: *Photograph of the fully assembled device. The chip is enclosed within the metal plate, and the copper tabs are used to keep the fiber arrays aligned and prevent them from bending.*

QKD setup, where it continues to operate and allows for experimental data collection.

4.1.7 Conclusions and future perspectives

We demonstrate a time-bin QKD receiver, fabricated using FLM to guarantee low optical losses and intrinsic polarization robustness. While FLM waveguides naturally exhibit very low birefringence, the highly unbalanced interferometer path makes even small residual effects non-negligible. For this reason, a dedicated post-fabrication correction was implemented, exploiting the flexibility of FLM to tune the birefringence and achieve full polarization insensitivity. The receiver exhibits insertion losses of 3.2 dB and 1.5 dB for the X and Z paths, respectively, and achieves a visibility of 99.73% for all input polarizations. Moreover, the measured time-bin delay matches Alice's with only 0.34 ps difference. Whereas [132] demonstrated a proof-of-principle integrated photonics system, we have engineered a fully field-deployable prototype suitable for real-world QKD applications. The chip is currently deployed in Geneva, where it is integrated into a complete QKD setup. It is being used for secret key exchange experiments over various emulated distances through standard single-mode fibers, as well as in field trials over the deployed fibers of the Geneva Quantum Network. The results

of these measurements are still under analysis and will be published soon.

4.2 Heterodyne receiver for quantum information processing

4.2.1 Motivation

In recent years, quantum information processing has rapidly advanced, particularly in QRNG and QKD. QRNG provides true randomness, while QKD enables secure communication over untrusted channels. Both can be implemented using either discrete-variable (DV) or continuous-variable (CV) protocols, depending on the exploited degrees of freedom. CV schemes, based on coherent detection, are especially attractive due to their high performance and compatibility with telecommunication standards: CV-QRNGs can reach multi-Gbps rates, while CV-QKD offers higher key rates than DV systems, albeit over shorter distances.

Coherent detection relies on an optical front-end and an electrical back-end implementing balanced homodyne or heterodyne detection. Considerable efforts have focused on miniaturizing such systems using integrated photonics, enabling scalable and mass-producible PICs. Miniaturization alone is not sufficient: minimizing optical losses is equally crucial, particularly at the receiver side of QKD, where each photon lost results in permanent loss of information.

In this work, we present FLM on borosilicate glass as an alternative platform for integrated coherent receivers. Although limited in terms of miniaturization due to the relatively low index contrast, FLM offers low propagation losses, efficient fiber coupling, cost-effective fabrication, and enhanced modularity. Its intrinsic polarization insensitivity, arising from polarization-independent directional couplers and negligible birefringence, allows multiple devices to be interconnected without active polarization control, in contrast to other platforms. These features have already proven advantageous in several quantum information processing tasks. The device provides seamless interfacing with commercial fiber-based lasers and balanced detectors, while integrated thermo-optic elements allow precise phase control and balancing. This tunability not only optimizes the performance of the electronic back-end but also ensures operation under conditions that match

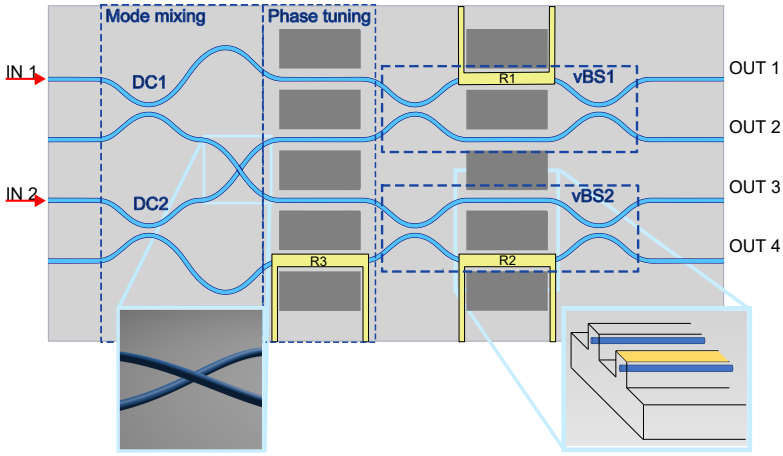

Figure 4.7: *Schematic layout of the FLM-fabricated photonic device. The dashed rectangle on the left indicates the mode-mixing region, where the two central modes exchange positions by crossing over one another (see left inset), enabled by the three-dimensional writing capabilities of FLM. The central dashed rectangle marks the region where the thermal phase shifter adjusts the $\Delta\theta_{LO}$ phase shift. The two dashed rectangles on the right denote the positions of the variable beam splitters (vBSs), realized as reconfigurable MZI, which are employed to balance the device outputs. The TOPSs, associated with resistors R1, R2, and R3, are shown in yellow, while the dark gray rectangles represent the trenches fabricated by FLM alongside the waveguides to enhance thermal insulation (see right inset), thereby reducing the power consumption of each micro-heater and minimizing thermal cross-talk.*

the requirements of CV protocols. In the broader framework of quantum communications, this device serves as the front-end of coherent receivers for CV-QRNG and CV-QKD, where shot-noise-limited detection is essential for achieving either secure key distribution or high-rate randomness generation.

4.2.2 Design and fabrication of the circuit

As illustrated in Fig. 4.7, the PIC implements a tunable optical hybrid comprising two 50:50 DCs, a controllable phase shifter $\Delta\theta_{\mathrm{LO}}$, and two variable beam splitters (vBSs) based on MZIs. When $\Delta\theta_{\mathrm{LO}} = \pi/2$ and the vBSs are balanced, the circuit functions as a 90° optical hybrid, a key element for both quantum and classical coherent detection. The overall layout is shown in Fig. 4.7.

The device was fabricated using the same waveguide parameters described in Section 4.1, resulting in a low-loss, single-mode waveguide operating at

Inscription Parameters	
Substrate	EAGLE XG®
Laser system	Pharos
Wavelength	1030 nm
Repetition Rate	1 MHz
Objective	20× 0.5 NA (Water Imm.)
Inscription depth	35 μm-50 μm
Pulse Energy	500 nJ
Translation speed	5-7 mm s^{-1}
Number of scans	4

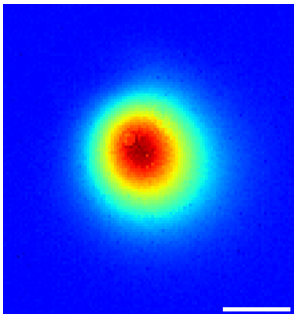

Table 4.3: *Inscription parameters for low-loss, single-mode waveguides at 1550 nm. The inset shows the waveguide mode profile. Scalebar is 5 μm.*

a wavelength of 1550 nm. The corresponding parameters are reported in Table 4.3. It occupies a footprint of 1.5 cm × 3.7 cm, with the main specifications summarized in Table 4.4. The measured fiber-to-fiber insertion losses are 1.05 dB (IN1) and 1.28 dB (IN2), with polarization dependence below 1%. These values include propagation and bending losses in the waveguides, coupling mismatch between fiber and guided modes, and connector losses.

All directional couplers were designed for a nominal 50:50 splitting ratio. Their reflectivity, reported in Table 4.4 for horizontal (H) and vertical (V) polarizations, confirms polarization-insensitive behavior with deviations below 1 %. To realize the hybrid, we exploited the 3D capabilities of FLM: as shown in Fig. 4.7, the two central waveguides cross at different depths with a vertical separation of 15 μm, eliminating crosstalk. Phase control, essential for tuning the vBSs and ensuring the correct $\pi/2$ phase offset of the LO, is achieved via integrated TOPSs. These are fabricated following the procedure explained in 3.1.3. A 2π phase shift is obtained with approximately 70 mW of dissipated power. The heaters are contacted through conductive epoxy to a custom PCB and driven by an external voltage source.

The PIC is designed for phase-diverse heterodyne coherent detection, where the quantum signal must interfere with a strong local oscillator (LO) field, treated classically due to its high intensity. The optical routing of the chip, combined with precise heater control, ensures this condition. In practice, the quantum signal and LO are injected into IN1 and IN2, split by the two 50:50 DCs, and subsequently combined in the vBSs. By properly

tuning R1 and R2, the vBSs act as balanced couplers, achieving a common-mode rejection ratio (CMRR) exceeding 73 dB, comparable or superior to bulk-optics solutions. While R3 introduces the required $\pi/2$ phase shift in one LO branch.

The optical outputs of the vBSs are then directed off-chip to balanced photodiodes (BPDs), enabling simultaneous measurement of the two quadratures of the input state at the shot-noise limit. Fine adjustment of the TOPSs ensures suppression of common-mode noise and optimized LO coupling, ultimately maximizing detection performance. This flexible design allows accurate control of the hybrid's operation and ensures robust coherent detection.

DEVICE SPECIFICATIONS		
Insertion Losses		
IN1	1.05 dB	
IN2	1.28 dB	
DC Reflectivities		
Polarization	DC1	DC2
H	0.502	0.506
V	0.502	0.502
Power Dissipation		
2π phase shift	70 mW	

Table 4.4: *FLM-written PIC specifications. Summary of insertion losses for IN1 and IN2 (see Fig. 4.7), reflectivity of the directional couplers for horizontal (H) and vertical (V) polarization, and electrical power required to induce a 2π phase shift.*

4.2.3 Conclusions and future perspectives

This work presents a glass-based PIC designed as a versatile coherent receiver for CV quantum information protocols. Thanks to FLM fabrication, the device seamlessly interfaces with commercial off-the-shelf components such as lasers and wide-band detectors, providing a cost-effective solution for CV quantum communications. Its high tunability, enabled by integrated TOPSs, ensures adaptability to different operating conditions. After calibration, the receiver successfully implements a heterodyne detection scheme with precise $\pi/2$ quadrature phase shift and high common-mode rejection ratio (CMRR $>$ 73 dB). These performance levels enable optimal operation in both CV-

QRNG and CV-QKD protocols, with detailed results reported in [131]. Furthermore, the device exhibited excellent operational stability over extended use, confirming its reliability for practical quantum communication scenarios. Table 4.5 summarizes the comparison between commercially available hybrid devices and PIC-based implementations.

Technology	Hybrid type (deg)	IL (dB)	Detector efficiency (%)	Overall efficiency (%)	Phase deviation (deg)	Ref.
Micro-optics	90	1 (typ.)	N/A	N/A	±5	Exail COH90
Silicon	90	3.19	80 (typ. Ge)[b]	38.4	±7.5	Finisar CPRV
Silicon	180	5.1	64[b]	20	N/A	[138]
Silicon	180	5	73 (inferred)[b]	49.8	N/A	[139]
Silicon	90	2.5	88[b]	44	NR	[140]
Silicon	180	4	64[b]	22.7	N/A	[141]
GaInAsP/InP	90	7.4	N/A	N/A	±5	[142]
Si_3N_4[a]	90	NR	N/A	N/A	<8	[143]
Silicon	180	5.1	80[b]	26	N/A	[144]
FLM	90	1.05	75 (avg.)	59.3	±0.9	This work

Table 4.5: *Comparison between commercially available and PIC-based hybrid devices. IL denotes insertion losses. "N/A" indicates the parameter is not applicable, and "NR" means the value was not reported.*

Finally, the compactness of the design, combined with the inherent robustness of FLM-fabricated devices, makes these receivers particularly suited for real-world deployment, even in harsh environments such as those encountered in space applications [145]. Together, these results highlight the versatility and practicality of FLM as a fabrication platform for next-generation quantum communication technologies.

CHAPTER 5

Scalable photonic system for quantum information processing

In this chapter, we present two distinct projects, both aimed at advancing scalable photonic integrated systems for quantum applications. The first project concerns the direct interfacing of a FLM-PIC with a Single-Photon Avalanche Diode (SPAD). This work was carried out in collaboration with the group of Prof. Giulia Acconcia at the Department of Electronics of Politecnico di Milano. My contribution focused on the design and fabrication of the FLM-PIC, the direct coupling between the PIC and the SPAD, as well as the acquisition and analysis of the experimental data. This work has been published in *Light: Science & Applications* [146].

The second project involves the realization of a reconfigurable three-arm interferometer designed to test Born's rule. This study was conducted in collaboration with the group of Prof. Tobias Vogl, initially at the University of Jena and later at the Technical University of Munich. In this case, my contribution was the fabrication of the PIC, followed by its characterization,

calibration, and validation with classical light.

5.1 Direct coupling of a laser-written PIC to a SPAD array

5.1.1 Motivation

Quantum photonics experiments generally rely on three fundamental stages: the generation of quantum states, their manipulation, often through interferometric PICs and their final detection. In DV quantum photonics, detection plays a crucial role, as it enables non-Gaussian operations via single-photon detectors. Most current implementations employ PICs coupled to either off-chip or on-chip Superconducting Nanowire Single-Photon Detectors (SNSPDs), which deliver excellent Photon Detection Efficiency (PDE), ultralow Dark Count Rates (DCR), and no afterpulsing. Nevertheless, the cost, footprint, and cryogenic requirements of SNSPDs limit their scalability and hinder applications in resource-constrained scenarios, such as satellites. Moreover, coupling through single-mode fiber arrays introduces additional losses and constrains the geometry of the PIC outputs.

A major step toward scalable quantum hardware is the integration of single-photon detectors directly into PICs operating at or near room temperature. In this context, SPADs represent a promising alternative, thanks to their solid-state nature, compactness, and potential for seamless integration. Recent demonstrations have shown the integration of SPADs with waveguide circuits both in the visible and in the telecom band. However, achieving System Detection Efficiencies (SDE), including both circuit and detector contributions, above 10% in fully integrated solutions remains highly challenging.

One promising approach to overcome these limitations is the heterogeneous integration of complementary photonic technologies within a single system. Following this strategy, we demonstrate the direct coupling of a four-mode glass PIC, fabricated via FLM, with an array of thin silicon SPADs manufactured using a custom planar process. By exploiting optimized fabrication for each technology and eliminating bulky optical interconnections, we achieve unitary coupling efficiency and report a SDE as high as 41.0% at 561 nm, the highest value obtained so far for both directly coupled and het-

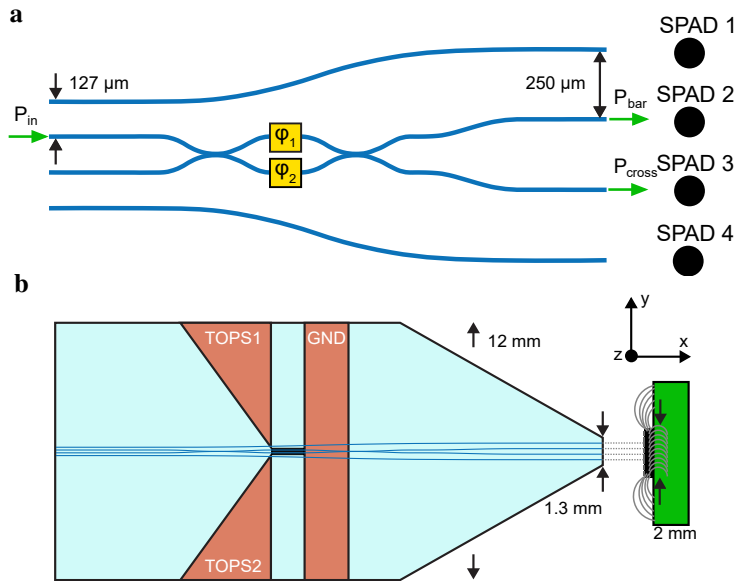

Figure 5.1: **a** *Waveguide layout showing the coupling scheme with the SPAD detectors; the two TOPSs are depicted as yellow rectangles. The input waveguides are spaced by 127 µm to match the fiber array, while the output waveguides are separated by 250 µm to match the SPAD pitch.* **b** *Illustration of the reconfigurable PIC coupled to the SPAD array. The photonic chip has a footprint of 25 mm × 12 mm, and its output facet is tapered to 1.3 mm to avoid interference with the bonding wires along the sides of the SPAD array.*

erogeneous/hybrid integrated PIC–SPAD systems. Together, these platforms provide all the technological degrees of freedom required to realize compact, scalable, and high performance quantum photonic systems, paving the way toward cost-effective solutions based on two-dimensional SPAD arrays and three-dimensional reconfigurable processors.

5.1.2 Design and fabrication of the PIC

The PIC (Fig. 5.1a) consists of four planar waveguides, designed to directly interface with a silicon SPAD array of 8 × 8 pixels, of which four were selected for this work (Fig. 5.2b) The input facet has a pitch of 127 μm, matching standard fiber arrays for convenient optical injection, while the output facet is expanded to 250 μm to coincide with the pixel spacing of the SPAD array. The two outer waveguides are independent and serve both to characterize the PDE of individual SPAD pixels and to optimize the global

alignment of the PIC with the array. In contrast, the two central waveguides form a reconfigurable MZI, composed of two nominally balanced directional couplers linked by straight arms, each equipped with an integrated TOPS. For proper integration with the wire-bonded SPAD array, the PIC output facet was tapered from 12 mm to 1.3 mm, as shown schematically in (Fig. 5.1b), preventing interference with the bonding wires. A dedicated active alignment procedure ensures simultaneous and efficient coupling of all four optical modes into their corresponding SPAD pixels.

The fabrication of the PIC consisted of two main stages: the inscription of the optical circuit and the realization of the TOPSs. For the optical circuit, the laser beam was focused through a 20× Zeiss water-immersion objective with numerical aperture 0.5 into a 1 mm-thick Corning Eagle XG borosilicate glass substrate, at a depth of 35 μm from the bottom surface. The inscription employed pulses at 1030 nm wavelength, with a repetition rate of 1 MHz and pulse duration of 180 fs. The process was optimized for single-mode guidance at 561 nm, using 220 mW average power, a translation speed of 20 mm/s, and 6 overlapping scans per waveguide. The parameter are summarized in Table 5.1. After laser writing, the sample underwent thermal annealing [88], resulting in waveguides with propagation losses of about 0.11 dB/cm and mode dimensions of 3.1×3.4 μm^2 (at $1/e^2$).

To minimize thermal cross-talk in the reconfigurable MZI, isolation trenches were introduced by laser ablation along the central arms. These trenches, 1 mm long, 40 μm wide, and 300 μm deep, provided thermal insulation and reduced the power required to operate the phase shifters.

Once the optical layer was completed, resistive microheaters were realized following the process described in [147]. A two-step photolithography sequence was employed: chromium was used for the resistive elements, while copper defined interconnections and contact pads. Two heaters were fabricated, one on each MZI arm (Fig. 5.2), with measured electrical resistances of 440 Ω (top) and 448 Ω (bottom).

After fabrication, the substrate was diced to reduce the facet size for direct interfacing with the SPAD array. The PIC was then mounted on an aluminum support together with two printed circuit boards (PCBs) hosting electrical connectors. Wire bonding with aluminum wires was used to connect the PIC

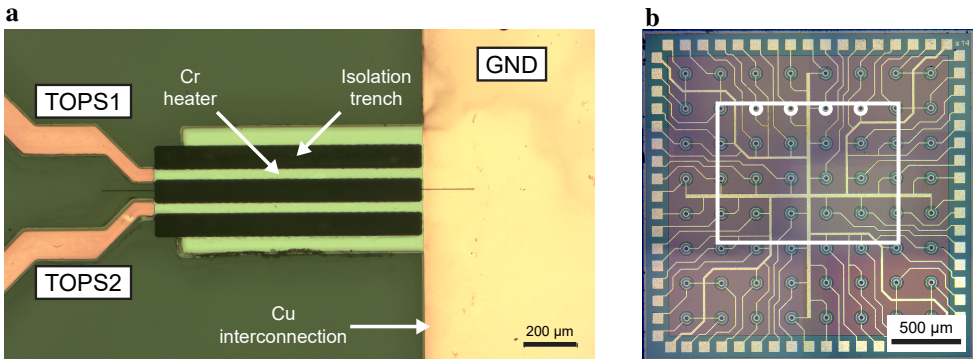

Figure 5.2: **a** *Micrograph of the two TOPSs fabricated on the arms of the reconfigurable MZI.* **b** *Micrograph of the 8×8 SPAD array. The white rectangle indicates the footprint of the PIC output facet (1.3 × 1 mm^2). The white circles highlight the SPADs selected for the coupling process (SPAD 1 to SPAD 4, from left to right).*

Inscription Parameters

Substrate	EAGLE XG®
Laser system	Pharos
Wavelength	1030 nm
Repetition Rate	1 MHz
Objective	20× 0.5 NA (Water Imm.)
Inscription depth	35 μm
Pulse Energy	220 nJ
Translation speed	20 mm s^{-1}
Number of scans	6

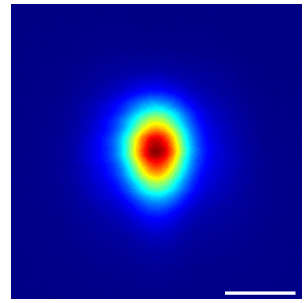

Table 5.1: *Inscription settings yielding low-loss, single-mode waveguides at 561 nm. Inset: guided mode of the waveguide. Scalebar is 3 µm.*

to the PCBs. A fiber array was subsequently aligned and glued to the input facet, ensuring stable optical access. After pigtailing, the device transmission reached 81.6%, corresponding to insertion losses of 0.9 dB.

5.1.3 Experimental setup and data acquisition

The experimental setup, adapted from Ref. [148] and shown schematically in Fig. 5.3, used a free-space 561 nm laser fiber-coupled to a Variable Optical Attenuator (VOA). The beam was then split by a 3 dB Fiber Splitter (FS): one arm was monitored with a Powermeter (PM), while the other was further attenuated with a Fiber Attenuator (FA) and divided again to simultaneously inject light into two input waveguides of the PIC. To calibrate the number

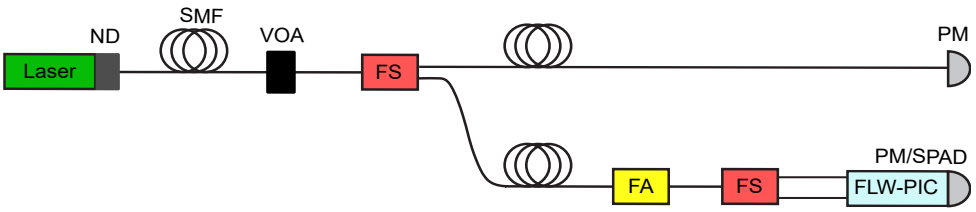

Figure 5.3: *The laser beam is first coupled into a single-mode fiber (SMF), then attenuated using a variable optical attenuator (VOA). A fiber splitter (FS) divides the beam into two paths: one directed to a powermeter (PM) for reference, and the other further attenuated by a fiber attenuator (FA) before being split again to feed two input waveguides of the PIC simultaneously. The PIC output is either monitored with a second PM for calibration or coupled to the SPAD array.*

of photons at the PIC output, the transmitted beam was collimated with an aspherical lens (NA = 0.55) and measured on a second PM. Sweeping the VOA power and fitting the data yielded attenuation values of 60.0 and 59.7 dB for the outputs coupled to SPAD 1 and SPAD 4, respectively, after correcting for lens transmission (94.5%).

Subsequently, the PIC output was directly coupled to the SPAD array, mounted on a custom PCB and aligned with sub-micrometric precision using automated hexapod stages (Fig. 5.4). Neutral density filters ensured photon rates compatible with the SPADs' dynamic range while maintaining sufficient signal to noise ratio on the monitor. Alignment was optimized by maximizing count rates on SPAD 1 and SPAD 4, which simultaneously guaranteed alignment of the central interferometer arms. Data acquisition involved monitoring the reference power to estimate photon numbers and recording SPAD count rates with a frequency meter in gated mode (1 s gate, 1 V threshold, 50 Ω input). Since the SPADs have a dead time of 55 ns, the measured counts N_{det} were corrected to account for this effect. The true photon rate N_{phot} was obtained as

$$N_{\text{phot}} = \frac{N_{\text{det}}}{1 - N_{\text{det}} T_{\text{dead}}}. \tag{5.1}$$

This correction ensured accurate estimation of the photon detection efficiency, crucial for benchmarking the performance of the directly coupled PIC-SPAD system.

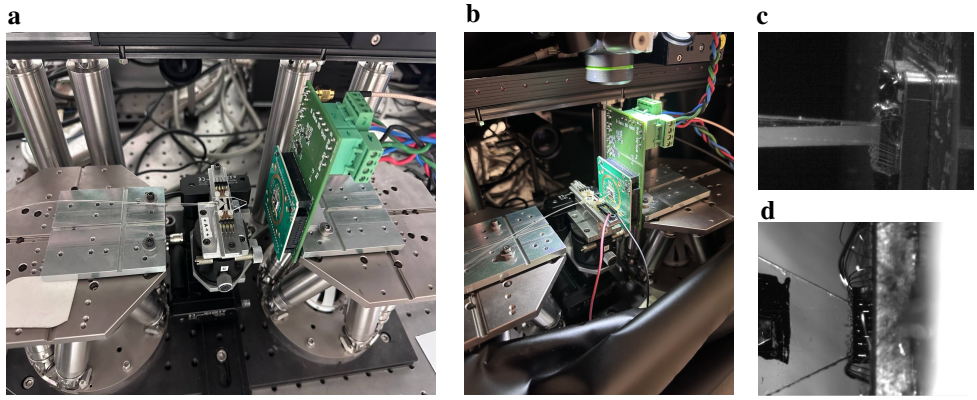

Figure 5.4: **a** *Photograph of the automated stages used for coupling. The PIC is mounted on the fixed stage, while the SPAD array is mounted on the hexapod.* **b** *Photograph of the PIC–SPAD coupling.* **c** *Side view of the coupling, acquired from one of the alignment cameras.* **d** *Top view of the coupling, acquired from the second alignment camera.*

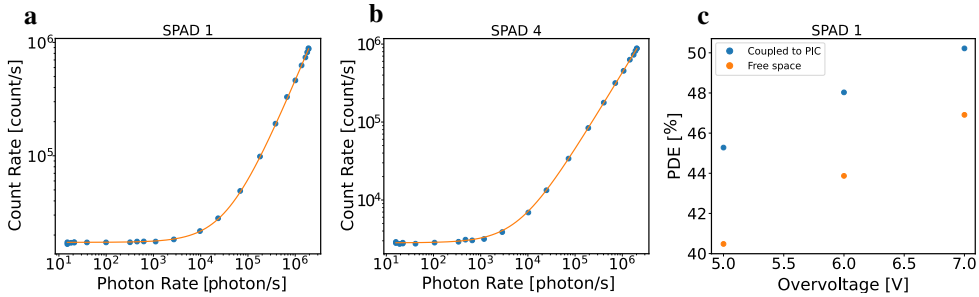

Figure 5.5: **a**, **b** *Linearity measurements of SPAD 1 and SPAD 4, acquired at different laser intensities.* **c** *Photon detection efficiency (PDE) as a function of the overvoltage.*

5.1.4 Validation of the PIC–SPAD coupling

The characterization of the PIC–SPAD assembly was carried out through three complementary measurements, each aimed at validating a different aspect of the system performance.

Linearity

First, linearity tests were performed on SPAD 1 and SPAD 4, coupled to the two outer waveguides, by sweeping the photon rate at the PIC output over five orders of magnitude. A Python-controlled setup regulated the input power via the VOA, and the resulting SPAD count rates were fitted with

linear regression models including the measured DCR as a fixed intercept, as showed in Fig 5.5. At 561 nm and 5 V we obtain PDE = 45.3% (SPAD 1) and 42.4% (SPAD 4). For comparison, we also performed a preliminary characterization of the SPAD array using a standard free-space setup [149], which yielded PDE values of 40.5% and 41.1%, respectively. The small discrepancy with respect to the waveguide-coupled measurements can be fully ascribed to the intrinsic non-uniformity of the PDE across the SPAD active area, as further discussed below, confirming unitary coupling efficiency between the PIC and the SPAD array. Varying the overvoltage confirms the expected trend: for SPAD 1 the PDE rises from 45.3% (5 V) to 50.2% (7 V) while DCR increases from 16.6 to 25.4 kcps; for SPAD 4 the PDE reaches 49.6% at 7 V with DCR from 2.9 to 4.5 kcps. Including PIC losses yields a system detection efficiency (SDE) improving from 37.0% $\rightarrow$ 41.0% (SPAD 1) and 34.6% $\rightarrow$ 40.5% (SPAD 4) when raising the overvoltage from 5 to 7 V.

PDE as a function of the PIC displacement

The second measurement aims to verify the robustness of the optical coupling, by mapping (always focusing on the two outermost waveguides) the PDE across the SPAD active area and as a function of the PIC–SPAD distance. The maps reported in Fig. 5.6a,b (and the corresponding cross-sections for $z = 0$ in Fig. 5.6c,d) were acquired simultaneously. The hexapod, controlled via a custom Python interface, enabled automated spatial scans of the PDE across SPAD 1 and SPAD 4. A 30×30 map over a 40×40 μm^2 area was acquired by sequentially moving the PIC facet in steps of ~ 1.3 μm. Since the laser intensity was kept fixed, PDE values were directly obtained from a single acquisition, with an integration time of 1 s per acquisition. The PDE distribution across the SPAD surface, delimited by the red circle indicating the 25 μm active area, clearly shows reduced efficiency at the edges compared to the center. This behavior is consistent with the weaker electric field near the detector boundaries, which lowers the triggering probability. In addition, since the scan was performed with a waveguide mode of 3.1×3.4 μm^2 $(1/e^2)$, displacements beyond the active area further reduce the PDE as part of the optical spot falls outside the detector. Remarkably, even for lateral

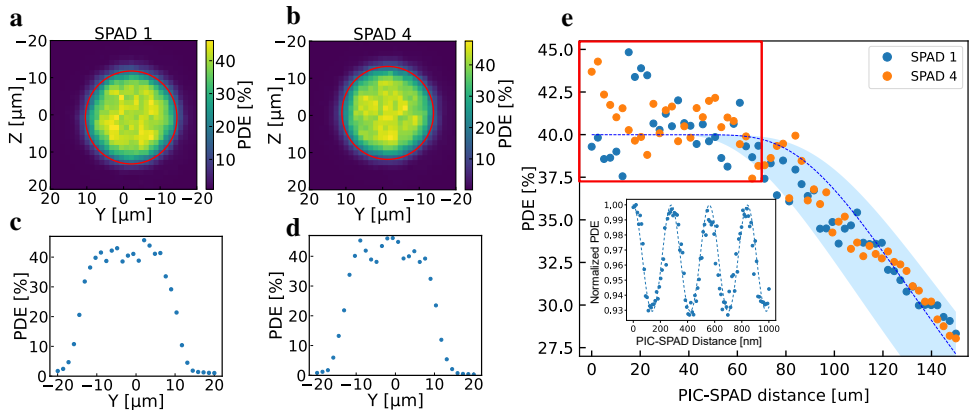

Figure 5.6: *PDE maps on the SPAD surface for* **a** *SPAD 1 and* **b** *SPAD 4. The red circle with a diameter of 25 µm indicates the physical boundary of the SPAD active area.* **c** *and* **d** *Corresponding profiles where the PDE is reported for $z = 0$.* **e** *PDE as a function of the distance between PIC and SPAD. The red rectangle highlights the region within $S = 70$ µm, where the PDE remains on average close to the values preliminarily measured with the free-space setup. The blue dashed line shows a PDE simulation, while the shaded area represents the uncertainty range. Inset (bottom left): normalized PDE fluctuations, attributed to the cavity between the SPADs and the waveguides, measured on a finer scale. The blue dashed line corresponds to the best sinusoidal fit.*

displacements as large as ±10 μm, the PDE remains essentially unchanged, highlighting the robustness of the coupling. Within the active region, the PDE is not perfectly uniform, reaching local maxima of 46.1% and 47.6% for SPAD 1 and SPAD 4, respectively. Averaging over the 20 μm diameter active area gives 39.9%±3.3% and 40.4%±3.6% for the two detectors. These values are consistent with those obtained in free-space measurements, with the small differences well within the uncertainty of the different methods.

Successively we investigated the dependence of PDE on the distance between the PIC facet and the SPAD surface. The waveguides were first aligned to the SPAD centers at about 1 μm separation, and the distance was varied up to 150 μm (Fig. 5.6e). Within the first 70 μm, PDE fluctuated between 37.5% and 45.0%, reflecting the intrinsic nonuniformity of the SPAD response, while the average values of 40.3 ± 1.8% (SPAD 1) and 40.7 ± 1.5% (SPAD 4) remained consistent with free-space characterizations. Beyond 70 μm the PDE decreased, as the diverging waveguide mode extended beyond the SPAD active area.

To interpret the data, we simulated the system by modeling the SPAD as a 25 μm-diameter circular detector with flat response inside the active area, and the waveguide output as an elliptical Gaussian beam with waists $w_x = 3.1$ μm and $w_y = 3.4$ μm. The normalized beam intensity was multiplied by the detector response and integrated at varying distances. Shaded regions in Fig. 3e correspond to uncertainties from $\delta = \pm 3$ μm lateral misalignment and $\Delta w = \pm 0.3$ μm errors in the mode dimensions, while the dashed blue curve shows the ideal case ($\delta = 0$, $\Delta w = 0$). From the experimental trend, we could also extract an effective numerical aperture of ~ 0.14, in good agreement with the low index contrast typically induced by the FLM process. A finer scan with 10 nm steps revealed weak oscillations in the PDE, with a fringe period of 280.5 nm and amplitude $\sim 3.2\%$, attributable to interference effects from the air gap between PIC and SPAD. Finally, we assessed angular misalignment by rotating the SPAD array: PDE decreased by less than 10% for tilts below 3°, confirming the robustness of the coupling.

Operation of the reconfigurable MZI

Finally, the operation of the reconfigurable MZI integrated in the PIC was demonstrated by injecting light into one input and recording the normalized count rates at SPAD 2 (bar) and SPAD 3 (cross) while sweeping the power dissipated by the upper microheater (0–30 mW, step 0.5 mW) using a source meter (Keysight B2902A). The experimental data followed the expected sinusoidal behavior, modeled by Eqs. (2)–(3),

$$N_{\text{bar}} = B_{\text{bar}} + A \sin^2\left(\frac{\varphi_0 + \alpha P}{2}\right), \tag{5.2}$$

$$N_{\text{cross}} = B_{\text{cross}} + A \cos^2\left(\frac{\varphi_0 + \alpha P}{2}\right), \tag{5.3}$$

which account for background contributions (B_{bar}, B_{cross}), nonunitary fringe amplitude A, an initial fabrication phase offset φ_0, and a linear tuning coefficient α. From the fit, we obtained $\varphi_0 = 5.06$ rad and $\alpha = 241.65$ rad/W, corresponding to a power of 26.0 mW for a 2π shift. The fitted background values ($B_{\text{bar}} = 0.0595$, $B_{\text{cross}} = 0.0374$) indicate incomplete extinction, at-

tributed to non-ideal directional couplers.

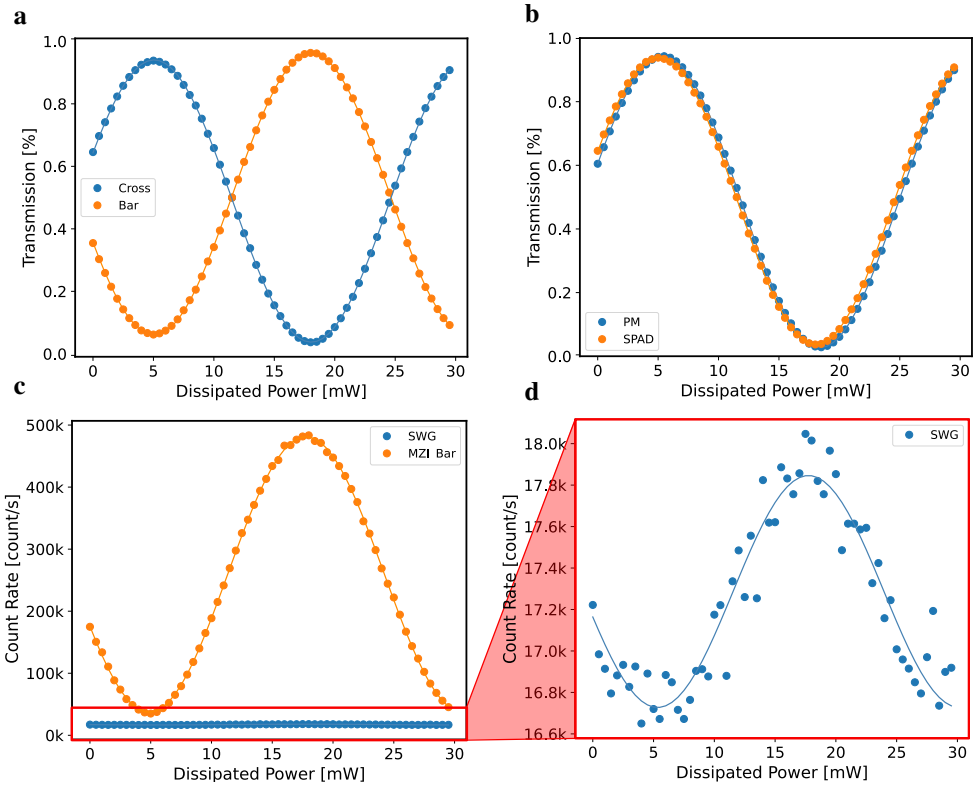

Figure 5.7: **a** *Normalized powers of the Bar (orange) and Cross (blue) outputs, measured with SPAD 2 and SPAD 3.* **b** *Comparison between measurements acquired with a SPAD (orange) and with a powermeter (blue), with the two curves superimposed. Despite small discrepancies due to different detector calibrations, the two results are in good agreement.* **c** *Measurement of optical cross-talk: when light is injected only into the MZI, count rates are observed from SPAD 2 (orange, corresponding to the Bar output of the MZI) and from SPAD 1 (blue, corresponding to the straight waveguide without light propagation).* **d** *Magnified view of the 16,600–18,000 count rate region, highlighting the optical cross-talk effect between the two SPADs.*

To confirm measurement consistency, the same sweep was repeated with standard powermeters, yielding compatible results for amplitude, phase, and tuning coefficient (Fig. 5.7b). Finally, possible crosstalk was assessed by monitoring SPAD 1, coupled to an adjacent independent waveguide, during the phase sweep. While no modulation was visible at the main scale (Fig. 5.7c), a closer inspection (Fig. 5.7d) revealed a weak sinusoidal trend with an amplitude of 0.31% (−25 dB), consistent with the intrinsic optical

crosstalk typically observed in SPAD arrays of the same generation.

5.1.5 Conclusions and future perspectives

In this work, we presented the direct coupling of a PIC with a SPAD array. Both devices were fabricated using custom technologies, providing full freedom to optimize their performance in the respective photonic tasks of manipulation and detection. Importantly, each device can be independently optimized, as the coupling imposes no technological constraints. The reported measurements confirm unitary coupling efficiency with negligible crosstalk, achieving a PDE of 50.2% at 561 nm and an SDE of 41.0%, the highest value among integrated PIC–SPAD systems. This performance even surpasses the best visible-range waveguide-integrated SNSPDs, confirming coupled systems as a practical route for scalable quantum experiments without compromising efficiency. Moreover, since the platform operates at wavelengths compatible with room-temperature single-photon sources, it enables the integration of generation, manipulation, and detection within laser-written circuits, paving the way for compact, cryogenics-free quantum technologies suitable for both terrestrial and space applications. To better contextualize these results, Table 5.2 presents a comparison with state-of-the-art photonic detector technologies, including heterogeneous, hybrid, and directly coupled solutions operating across different material platforms and wavelength regimes. The comparison highlights key performance metrics such as system detection efficiency (SDE), dark count rate (DCR), operating temperature, and photonic circuit technology, providing a comprehensive benchmark against existing integrated and coupled implementations.

Ref.	Technology	Photonic circuit	Detector	Temperature (K)	Wavelength (nm)	SDE (%)	DCR (count/s)
[150]	Het	SiN	SNSPD	1.4	532/1550	22/60	25–350
[151]	Hybrid	Si	InGaAs/InAlAs SPAD	220	1550	0.02	860k
[152]	Het	Si	Ge-on-Si SPAD	78	1310	13	279k
[153]	Het	SiN	Si SPAD	RT	488/532	10/6	107k
[154]	Het	SiON	Si SPAD	RT	850	5	100
[155]	Coupling	Polymer	Si SPAD	RT	785	2	5–30
This work	Coupling	Glass	Si SPAD	RT	561	41	4.5k–25.4k

Table 5.2: *Comparison with state-of-the-art photonic detector technologies, including heterogeneous, hybrid, and directly coupled solutions. (RT = room temperature, Het = Heterogeneous; SDE values account for PIC propagation and coupling losses, except for [153], which does not report these data.)*

Additional PDE measurements across the SPAD active area and as a function of the PIC–SPAD distance demonstrate micrometric tolerance in both lateral alignment and spacing, ensuring efficient coupling without the need for nanometric positioning. This renders the system compatible with compact and cost-effective micropositioners. A potential limitation is the air cavity at the interface, which introduces sensitivity to nanometric displacements; however, this effect can be mitigated using index-matching oil or permanent bonding with optical adhesives, further enhancing robustness and compactness. Finally, we successfully characterized a reconfigurable MZI coupled to the SPAD array. This is an important step toward the integration of SPAD arrays with FLW reconfigurable processors, in both planar and three-dimensional implementations.

5.2 Reconfigurable Integrated photonic chip to test Born's rule

5.2.1 Motivation

This project aims to experimentally test the Born's rule by realizing a three-path interferometer integrated on a glass-based chip. Verifying Born's rule requires isolating and measuring all interference terms, a task that is extremely challenging in free-space implementations due to the difficulty of maintaining phase stability across multiple arms. Similar experiments have already been performed in bulk optics [156–158], but those systems suffer from limited phase stability and stringent alignment requirements, making long-term, high-precision measurements very demanding.

An integrated photonic approach overcomes these limitations, providing improved phase stability, compactness, straightforward control, and alignment-free operation. FLM in particular offers a powerful solution, enabling three-dimensional, rapid-prototyping fabrication of compact interferometers with intrinsically phase-stable paths. The micrometric size of FLM-written waveguides, combined with the sub-micrometric precision of the inscription process, enables highly accurate control of the spacing between coupled waveguides. In fact, the relatively low index contrast of FLM waveguides makes the coupling distance less sensitive to fabrication tolerances compared to silicon photonics platforms, where even nanometric

deviations strongly affect the coupling ratio. As a result, FLM allows the reliable realization of directional couplers with the desired splitting ratios, enabling MZI switches with extinction ratios exceeding 35 dB. In addition, optimized FLM processes ensure low propagation losses (< 0.14 dB/cm at 561 nm), further enhancing device performance. Furthermore, FLM waveguides have been qualified for space applications [145].

Beyond the realization of a three-path interferometer for fundamental tests, this project was conceived with a broader perspective: the development of a fully integrated quantum photonic system. Indeed, a copy of the chip has been fabricated with integrated photon sources and detectors, creating a complete platform, source, interferometer, and detection, within CubeSat-compatible dimensions [159]. This enables experimental verification of Born's rule not only on Earth but also in space and under microgravity conditions, demonstrating the scalability and versatility of FLM for compact and robust quantum technologies.

5.2.2 Testing Born's rule with multi-path interferometry

According to Born's rule [160], the probability density of detecting a quantum particle at a position r and time t is given by the square modulus of its wavefunction,

$$P(r,t) = |\Psi(r,t)|^2. \tag{5.4}$$

Let us consider an interferometer comprising multiple independent paths $k = A, B, C, \ldots$, which recombine at the output port. The resulting wavefunction at the output can be written as $\Psi = \sum_k \Psi_k$. According to Born's rule, the detection probability becomes

$$P = \sum_k |\Psi_k|^2 + \sum_{k<l} I_{kl}, \tag{5.5}$$

where the terms $I_{kl} = \Psi_k^* \Psi_l + \Psi_l^* \Psi_k$ represent the two-path interference contributions. A direct implication of Born's rule is that only such two-path terms appear, any genuine three-path (or higher) interference is strictly excluded.

Sorkin formalized this by introducing a hierarchy of interference terms

[161]. For a three-arm interferometer, the second-order contribution is defined as

$$I^{(3)}_{ABC} = P_{ABC} - P_{AB} - P_{AC} - P_{BC} + P_A + P_B + P_C - P_0, \tag{5.6}$$

where P_{AB} is the detection probability with only paths A and B open, and P_0 denotes the background with all arms closed. Standard quantum mechanics predicts $I^{(3)}_{ABC} = 0$ under all conditions. A non-zero result would indicate physics beyond standard quantum mechanics, providing evidence for generalized theories that permit higher-order interference [162].

In experiments, probabilities are estimated from the measured particle fluxes p, leading to the observable

$$\epsilon = p_{ABC} - p_{AB} - p_{AC} - p_{BC} + p_A + p_B + p_C - p_0. \tag{5.7}$$

For comparison across setups, one introduces the normalized parameter

$$\kappa^{(3)} = \frac{\epsilon}{\delta_3}, \qquad \delta_3 = |I_{AB}| + |I_{AC}| + |I_{BC}|, \tag{5.8}$$

with $I_{AB} = p_{AB} - p_A - p_B + p_0$ representing the experimentally determined two-path interference. Quantum theory requires $\kappa^{(3)} = 0$, and higher-order parameters $\kappa^{(n)}$ can be analogously defined for interferometers with more than three paths.

A range of Sorkin-type experiments, including optical interferometers [156–158, 163] and NMR systems [164] have consistently reported results compatible with $\kappa^{(3)} = 0$, with the most stringent bounds reaching the 10^{-5} level [157]. Ultimately, the precision of such null tests is limited mainly by the stability of the interferometer phase and by detector nonlinearities.

5.2.3 Design and fabrication of the three-arm interferometer

The circuit layout is shown in Fig. 5.8. To test Born's rule, we require a three-path interferometer in which each path can be individually switched on or off. The input beam is first divided into three equal-amplitude paths using a cascade of two directional couplers. Specifically, the light first encounters a 33:66 coupler, which splits the input into one third (bar port) and two

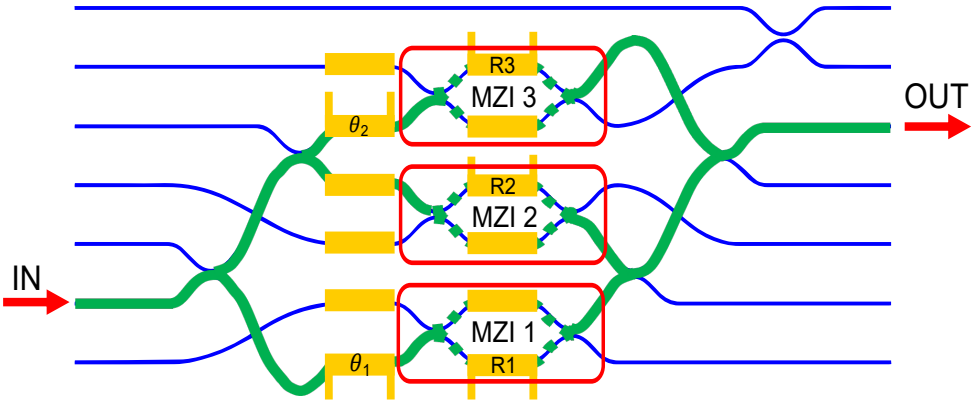

Figure 5.8: *Born's chip circuit layout. Top view of the device, where the green line traces the optical path followed by the light, aiding the visualization of the three-arm interferometer layout. Light enters from the left (red arrow) and is split into three nominally equal-intensity paths by two cascaded directional couplers with splitting ratios of 33:66 and 50:50, respectively. Each path contains an MZI acting as an optical switch (highlighted by red rectangles). The paths are then recombined at the output through the same two couplers in reverse order (50:50 followed by 33:66). Yellow rectangles indicate the TOPSs fabricated on both the internal and external arms of each MZI. Although all TOPSs were fabricated, since their inclusion does not significantly affect the fabrication cost, only those with yellow pins exiting the rectangles are used in the experiment. Specifically, the internal TOPSs labeled R1, R2, and R3 act as resistive heaters controlling the optical switches within each MZI, while the external TOPSs labeled θ_1 and θ_2 are employed to tune the relative phases between the three interferometer paths. Layout not to scale.*

thirds (cross port). The one-third portion directly defines one arm of the interferometer, while the remaining two-thirds are further divided into two equal parts by a 50:50 coupler, thus forming the other two arms. As shown in Fig. 5.8, the green line traces the optical path followed by the light, helping to visualize the three-arm interferometer layout.

Each of the three arms is equipped with a reconfigurable MZI, acting as an optical switch that allows us to selectively enable or disable the corresponding path. Resistive heaters were fabricated on both internal arms of each MZI for redundancy; however, only one heater per MZI is required and used in the experiment, specifically those labeled R_1, R_2, and R_3. In this way, we can independently study single-path, two-path, and full three-path interference contributions. After propagation, the three arms are recombined through the reverse sequence of couplers, first a 50:50 coupler, then the 33:66 coupler, mirroring the splitting stage.

Additional TOPSs are integrated along the arms of the three-arm interferometer to finely tune its operating point to an interference maximum in the phase diagram. All the resistive heaters implemented on the chip are shown in Figure 5.8; however, only the two TOPSs labeled θ_1 and θ_2 are actively used to perform this phase tuning operation. Finally, in the top-right part of the circuit of Fig. 5.8, an extra 50:50 directional coupler is included, enabling $g^{(2)}$ measurements of the single-photon source. In this chip, reference waveguides are placed at the input of the chip, specifically in modes 1, 2, 4, and 6 (counting waveguides from the bottom). As shown in Fig. 5.9a, these references are implemented exploiting the 3D capabilities of FLM, using vertical 90:10 directional couplers, designed to tap a small fraction of light. This allows us to continuously monitor a reference signal, thus compensating for coupling fluctuations and reducing measurement errors. The couplers were fabricated by optimizing the horizontal coupling distance, as in Fig. 5.9b, yielding a 90:10 splitting ratio at 6.4 μm. One arm is then routed vertically, displaced by 80 μm. A sectional view of the vertical coupler is shown in Fig. 5.9c.

Achieving a high extinction ratio is crucial for the success of the experiment, as it ensures that unwanted residual light is suppressed, avoiding spurious contributions when measuring different interference terms. For this reason, an important feature of the circuit layout is that each MZI is implemented in the cross configuration. In this scheme, the output path is routed through the cross port, since this configuration guarantees high extinction ratios even when the two directional couplers are not perfectly balanced at 50:50. This can be verified by evaluating the transfer matrix of a MZI composed of two identical directional couplers with transmission coefficient ε, separated by a phase shifter introducing a relative phase ϕ:

$$\begin{aligned} H(\phi,\varepsilon) &= \frac{1}{\sqrt{2}}\begin{bmatrix} \sqrt{\varepsilon} & i\sqrt{1-\varepsilon} \\ i\sqrt{1-\varepsilon} & \sqrt{\varepsilon} \end{bmatrix}\begin{bmatrix} e^{i\phi} & 0 \\ 0 & 1 \end{bmatrix}\begin{bmatrix} \sqrt{\varepsilon} & i\sqrt{1-\varepsilon} \\ i\sqrt{1-\varepsilon} & \sqrt{\varepsilon} \end{bmatrix} \\ &= \begin{bmatrix} \varepsilon e^{i\phi} - (1-\varepsilon) & i\sqrt{\varepsilon(1-\varepsilon)}(e^{i\phi}+1) \\ i\sqrt{\varepsilon(1-\varepsilon)}(e^{i\phi}+1) & (1-\varepsilon)e^{i\phi} - \varepsilon \end{bmatrix}. \end{aligned} \tag{5.9}$$

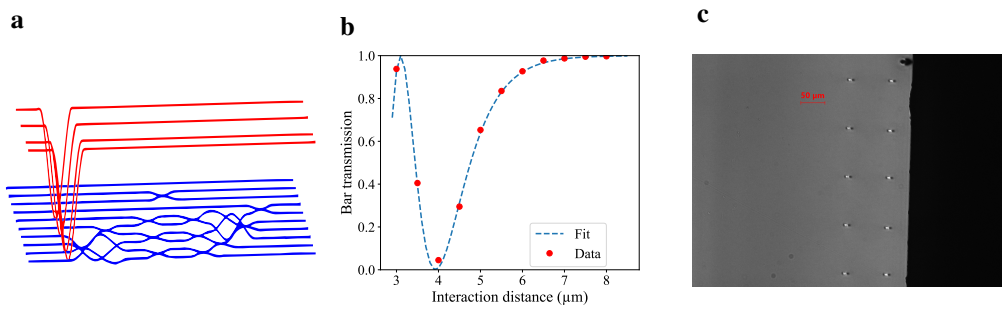

Figure 5.9: *Vertical coupler exploiting 3D FLM.* **a** *Side view highlighting the three-dimensional reference waveguide and the 3D crossing waveguide of the circuit.* **b** *Coupler transmission as a function of interaction distance.* **c** *Micrograph of the coupler section.*

By computing the square moduli of the matrix elements, it is clear that when light is injected into the upper port, the bar output corresponds to the top-left element, i.e.,

$$P_{\text{bar}} = |H_{11}(\phi, \varepsilon)|^2 , \tag{5.10}$$

which never vanishes completely unless $\varepsilon = 0.5$. Similarly, the cross output corresponds to the bottom-left element, i.e.,

$$P_{\text{cross}} = |H_{21}(\phi, \varepsilon)|^2 , \tag{5.11}$$

which goes exactly to zero for $\phi = \pi$, independently of the splitting ratio. Specularly, when light enters from the lower port the relevant amplitudes correspond to the second column of the matrix: the cross output (top-right element) can still reach perfect extinction, while the bar output (bottom-right element) remains sensitive to deviations from the ideal 50:50 condition. This observation justifies the choice of implementing all MZIs in the cross configuration, since it guarantees robust extinction even in the presence of fabrication imperfections.

The waveguides were fabricated following the same procedure described in 5.1.2, ensuring low-loss single-mode operation at 561 nm. The final device exhibits a total insertion loss of about 2 dB, with the directional couplers showing splitting ratios of 51:49 and 34:66, in close agreement with the design values. The TOPSs were realized using the process detailed in 3.1.3,

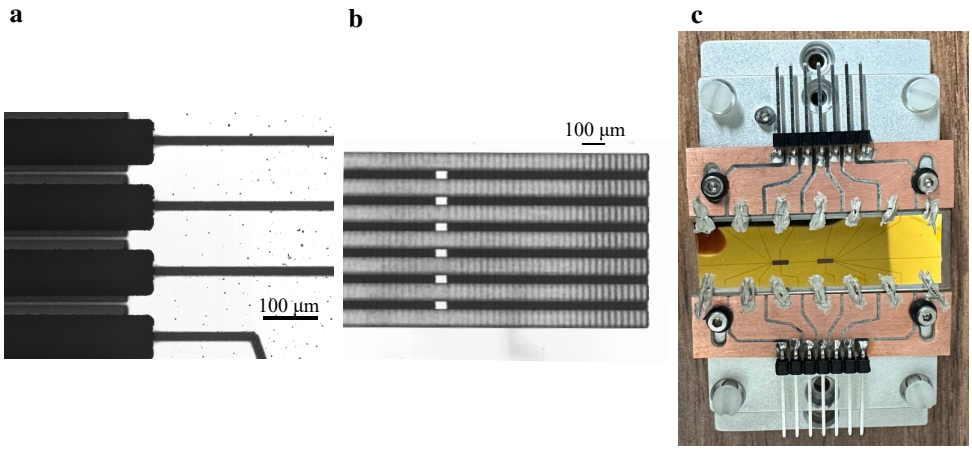

Figure 5.10: *TOPS and final assembly.* **a** *Micrograph of the microheater (thin gold strip on the left) and the gold contact pads (right).* **b** *Top-view micrograph of the trenches, where the characteristic pillar of the U-trenches is visible.* **c** *Photograph of the fully assembled device mounted on an aluminum plate, with the PCB connected to the pins.*

here implemented with U-shaped trenches 3 mm long and 70 µm wide (see Fig. 5.10a). The resistors, patterned with the same length as the trenches and a width of 9 µm, exhibited resistances of about 150 Ω (see Fig. 5.10b). We fabricated a total of 12 resistors, 6 associated with the internal phases of the MZIs and 6 placed externally at the MZIs. Since adding additional heaters comes at no extra fabrication cost, the layout was designed with redundancy.

The chip was then mounted on an aluminum plate for thermal stabilization, next to a custom PCB. Electrical connections between the gold pads and the PCB were established using conductive epoxy glue. The output waveguides are spaced by 127 µm, and the overall footprint of the device is 1.5×5 cm^2.

5.2.4 Validation of the device

To characterize the device, we employed a coherent laser source at 561 nm. The output beam, linearly polarized, was first steered by two mirrors, then passed through a half-wave plate and a polarizer, allowing us to perform measurements for both H and V polarizations. FLM devices are known to be intrinsically polarization insensitive; however, when measuring high extinction ratios (ER), small differences between the two polarizations can still be observed. The light was then coupled into the chip in an end-

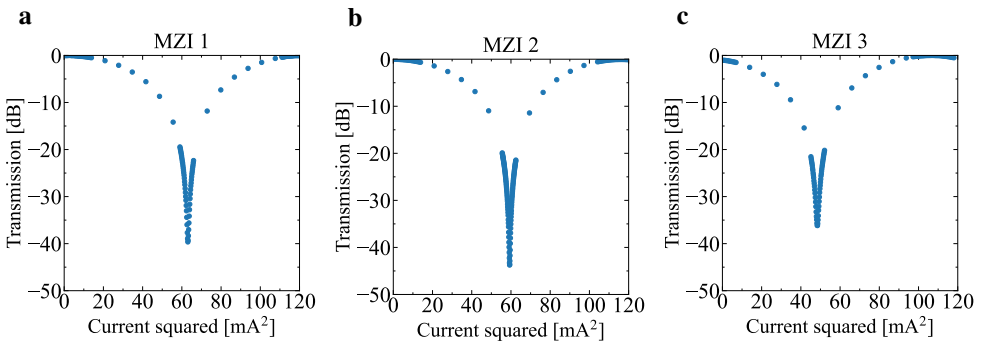

Figure 5.11: *Extinction ratio measured for MZI 1, MZI 2, and MZI 3.*

fire configuration using an aspheric lens with NA = 0.14, chosen to match the numerical aperture of the waveguides. At the output, the signal and the reference light were collimated by an aspheric lens with NA = 0.4 and directed to a powermeter. The TOPSs were driven by high-precision electronic drivers (Qontrol Q8iv).

To assess the performance of the three-arm interferometer, we first characterized the optical switches by measuring the ER of each MZI individually. This was done by injecting light into the input corresponding to each interferometer (inputs 1, 4, and 6 for MZI 1, 2, and 3, respectively) and collecting the signal at the cross port. The current applied to the corresponding TOPS was scanned while recording the output power, which was normalized to the reference channel. The ER was then calculated as

$$\mathrm{ER} = 10 \log_{10} \left(\frac{P_{\min}}{P_{\max}} \right), \tag{5.12}$$

where $P_{\min}$ and $P_{\max}$ denote the minimum and maximum powers, normalized to the peak value, respectively. The measurement was repeated for both H and V polarizations, showing slightly better performance in the H case. Figure 5.11 reports the ER as a function of the squared current for the three MZIs under H polarization.

All three MZIs exhibit extinction ratios above 35 dB in absolute value, confirming their high efficiency as optical switches. One of them reaches a maximum value of 46 dB. The small variations observed among the three

MZIs can be ascribed to fabrication imperfections. After verifying the quality of the individual MZIs, we calibrated the device to operate all three switches simultaneously, taking into account thermal crosstalk. This calibration enables the realization of all eight possible configurations of the interferometer, corresponding to the eight interference terms in Eq. (5.7), which are required for evaluating the second-order interference contribution.

Calibration

When operating multiple MZIs, the activation of one element can thermally affect the others, shifting their operating points and thus compromising proper switching. To reliably turn the switches ON or OFF, a calibration procedure is therefore required. In this framework, the ON/OFF operation of a switch corresponds to setting the MZI in one of its two fundamental configurations. The CROSS state is defined as the ON state, in which the light remains confined within the three-arm interferometer. This condition is achieved when the internal phase difference between the arms is set to 0 (mod 2π). Conversely, the BAR state represents the OFF state, where the light is routed out of the three-arm interferometer. This occurs when the internal phase difference equals π (mod 2π). As clearly shown in Fig. 5.12a, by scanning the dissipated current on the TOPS it is possible to switch the device from the ON state to the OFF state. This behavior can be accurately described by the following fitting relation:

$$P_{cross}(I) = BG + A \cdot \cos^2\left(\frac{\phi_0 + \beta I^2\left(1 + \epsilon I^2\right)}{2}\right). \tag{5.13}$$

In this expression, BG accounts for the background light, A is a proportionality factor related to the amplitude, ϕ_0 represents a residual static phase in the MZI arising from fabrication imperfections, β is the tuning coefficient, and ϵ models the self-dependence of the heater resistance on temperature. This formulation describes the case of a single MZI. However, when multiple MZIs are operated simultaneously, the phase–current relation must be generalized to a matrix form that accounts for the thermal cross-talk induced by neighboring heaters:

$$\begin{bmatrix} \phi_1 \\ \phi_2 \\ \phi_3 \end{bmatrix} = \begin{bmatrix} \phi_{01} \\ \phi_{02} \\ \phi_{03} \end{bmatrix} + \hat{\beta} \begin{bmatrix} I_1^2 \left(1 + \epsilon_1 I_1^2\right) \\ I_2^2 \left(1 + \epsilon_2 I_2^2\right) \\ I_3^2 \left(1 + \epsilon_3 I_3^2\right) \end{bmatrix}, \tag{5.14}$$

where the matrix $\hat{\beta}$, referred to as the *cross-talk matrix*, describes the thermal influence of each heater on the considered MZI.

The calibration was carried out in two stages. First, the transmission of each MZI was measured as a function of the current applied to its own heater, allowing the extraction of the diagonal elements of $\hat{\beta}$ (Fig. 5.12b). During this step, the parameters BG, A, ϕ_0, and ϵ were also determined and stored, with ϵ being a property of the resistor rather than the interferometer itself. In the second stage, the transmission of each i-th MZI was recorded while activating neighboring j-th heaters. The fitting was then repeated with only the cross talk term $\beta_{i,j}$ as a free parameter, while all other quantities were kept to the values inferred from the fits of the diagonal elements. This procedure enabled the determination of the off-diagonal elements of $\hat{\beta}$, thus providing a complete characterization of thermal cross-talk, and allowing their compensation during device operation.

To verify the effectiveness of the calibration, all eight possible ON/OFF configurations were tested. For each configuration, the transmission of each MZI was measured, and the ER between the ON and OFF states was extracted. This was achieved by scanning all configurations using an automated Python script. The results, shown in Fig. 5.13, demonstrate that the worst-case ON/OFF ER across all configurations and all MZIs remains above 32.5 dB. This confirms the reliability of the calibration procedure and ensures a high level of light extinction in the optical paths.

After calibrating the switches, the three-arm interferometer itself must also be calibrated. In order to maximize the signal-to-noise ratio, the experiment needs to be performed at a maximum point of the phase-space diagram. To retrieve this diagram, a current scan was applied to two microheaters of the three-arm interferometer (corresponding to the external resistors of the MZIs), while all three MZIs were kept in the ON configuration. The output intensity of the three-arm interferometer was then recorded. The resulting

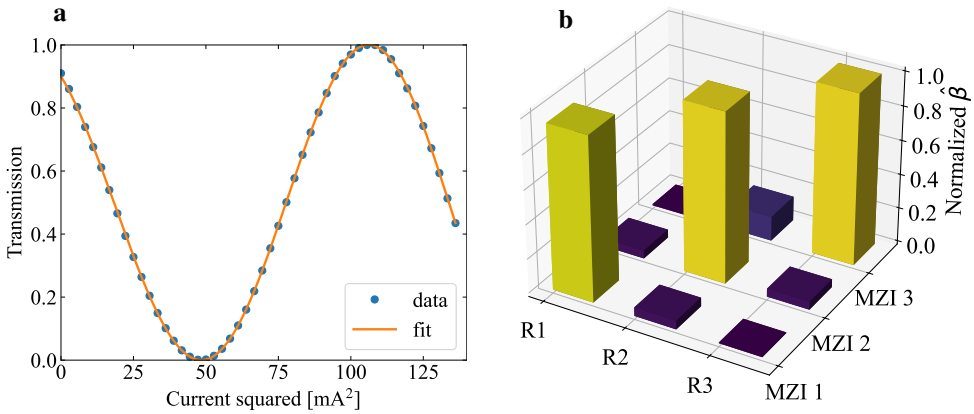

Figure 5.12: **a** *Transmission of an MZI as a function of the current flowing through its heater resistor (measured curve). The ON state corresponds to the condition where the light remains confined within the three-arm interferometer, achieved when the internal phase difference between the arms is set to* 0 *(mod* 2π*). Conversely, the BAR state represents the OFF condition, in which the light is routed out of the three-arm interferometer, and occurs when the internal phase difference equals* π *(mod* 2π*). In the plotted curve, a transmission value of* 1 *corresponds to the ON state, while a transmission of* 0 *indicates the OFF state.* **b** *3D histogram representing a normalized version of matrix* $\hat{\beta}$ *from Eq. (5.14), used to map the crosstalk between MZIs. Diagonal bars correspond to self-modulation (each MZI actuated by its own heater), while off-diagonal bars quantify the crosstalk induced by heaters of the other MZIs.*

phase-space map is shown in Fig. 5.14a, with a magnified view in Fig. 5.14b. From this representation, the maximum was extracted by means of a bi-quadratic fit, thus providing the optimal operating point for the experiment. The ER of the three-arm interferometer was also evaluated, yielding a value of 32.5 dB as extracted from the phase-space diagram data.

It is worth noting that the MZIs themselves act as heat sources within the three-arm interferometer. As a consequence, when different ON/OFF configurations are applied, the thermal load changes and the maximum point of the phase-space diagram for the two-arm interferences drifts accordingly. This correction is required only for the three configurations (ON–ON–OFF, ON–OFF–ON, and OFF–ON–ON), where two arms are active and interfere, while in the other cases only a single optical path is present and no interference occurs. To account for this drift, we measured the output intensity of the three-arm interferometer for each of the three two-arm interference configurations

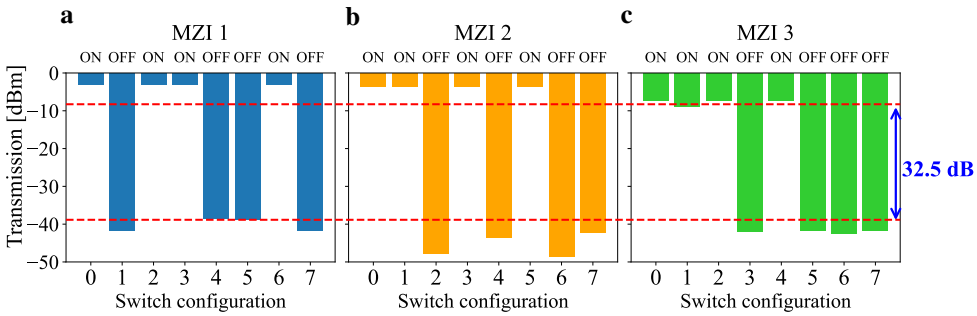

Figure 5.13: *Transmission of MZI 1 (***a***), MZI 2 (***b***) and MZI 3 (***c***) for each switch configuration. After calibration, a high extinction ratio (32.5 dB) is still achieved, as indicated by the blue arrow between the worst-case OFF and ON states (delimited by the two red dashed lines), confirming the effectiveness of the applied calibration procedure.*

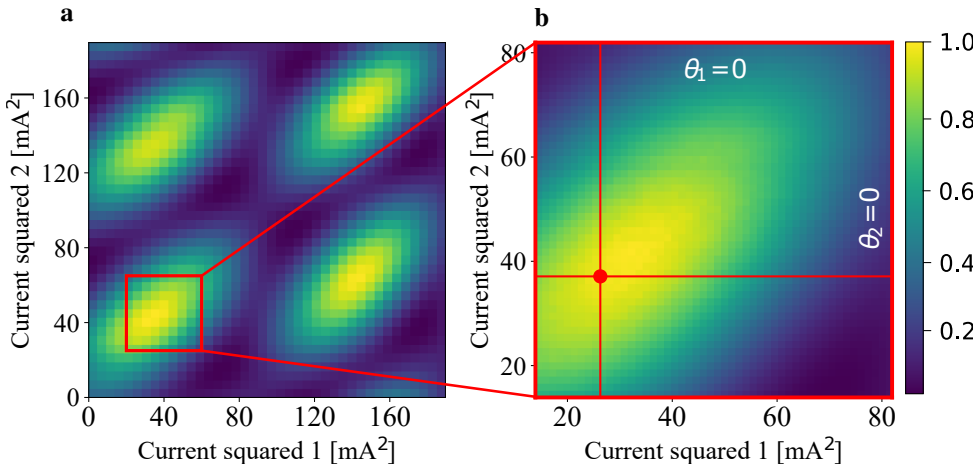

Figure 5.14: *Phase space of the three-arm interferometer.* **a** *Normalized output intensity of the device as a function of the current squared applied to the two external microheaters. The red square highlights the region of interest around one interference lobe.* **b** *Magnified view of the selected region, shown with the same red frame. The red lines connect the highlighted area in* **a** *with the zoomed region in* **b**. *The red dot indicates the maximum operating point extracted from a bi-quadratic fit, which defines the optimal bias condition for the experiment.*

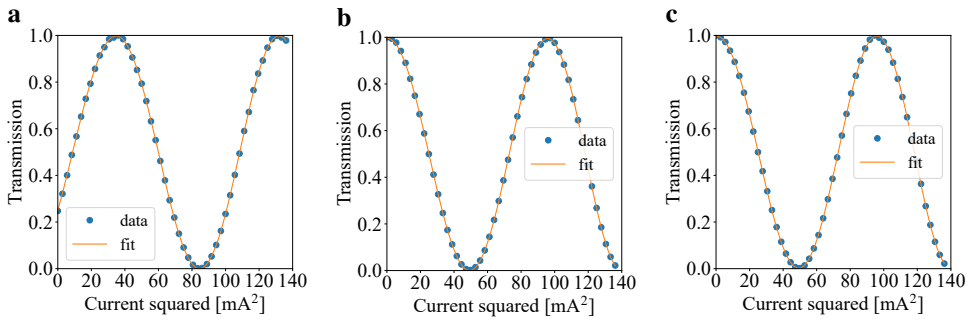

Figure 5.15: *Calibration curves of the three-arm interferometer for the three two-arm interference configurations: ON–ON–OFF (***a***), ON–OFF–ON (***b***), and OFF–ON–ON (***c***). In these cases, two arms are simultaneously active and interfere. For each configuration, the output intensity was measured as a function of the heater current squared, and the corresponding maximum point was extracted.*

and determined the corresponding maximum point, as shown in Fig. 5.15. These values were then used to correct the operating condition during the experiments, ensuring that the system consistently operates at the optimal interference point.

Experiment with classical light

After completing the calibration, the experiment was performed using coherent classical light. An automated Python script was employed to carry out 100 measurements, each corresponding to a data point in Fig. 5.16. Each point represents the measured intensity for all eight ON/OFF configurations, from which the normalized three-path interference term $\kappa^{(3)}$ of Eq. (5.8) was calculated. From these measurements, we obtained a mean value of $\kappa^{(3)} = -4.68 \times 10^{-4}$ with a standard deviation of 8.39×10^{-4}, which is compatible with a theory predicting $\kappa^{(3)} = 0$, with a comparable state-of-art accuracy achieved with classical light [156–158, 163]. This classical validation represents only a preliminary step, as the final experiment will be performed using single-photon sources based on color centers in the two-dimensional material hexagonal boron nitride (hBN), aiming to suppress detector nonlinearity and shot noise, and thus achieve improved performance.

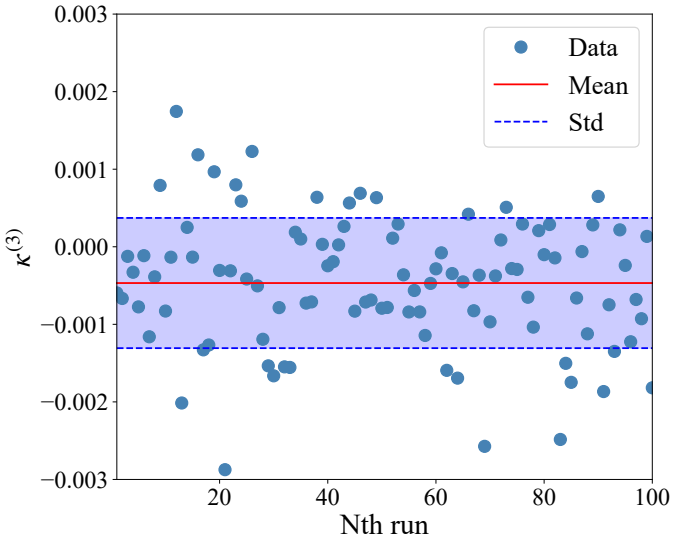

Figure 5.16: *Normalized three-path interference term measurement. A total of 100 consecutive measurements were performed, each corresponding to a data point in the figure. Each point represents the extracted value of the normalized three-path interference term* $\kappa^{(3)}$ *of Eq. (5.8), obtained from the measured intensities of all eight ON/OFF configurations. The red line indicates the mean value, while the blue dashed lines represent the standard deviation interval, with the shaded area highlighting this range. From these measurements, we obtained a mean value of* $\kappa^{(3)} = -4.68 \times 10^{-4}$ *with a standard deviation of* 8.39×10^{-4}.

5.2.5 Conclusions and future perspectives

We report on the realization of an integrated three-arm interferometer developed to test Born's rule. In this section, we have shown how FLM can play an important role in such a project by simplifying the design of the interferometer through its 3D fabrication capabilities, while at the same time enabling the realization of high-extinction-ratio MZIs and the integration of vertical directional couplers used as references. After fabrication, a complete calibration procedure was carried out in order to correctly implement all switching configurations and to determine the optimal operating point that maximizes the signal-to-noise ratio during the experiment. From this calibration, we measured extinction ratios above 32.5 dB for both the individual configurations and the three-arm interference, confirming the accuracy of the procedure and ensuring high extinction of the light.

The first validation experiment was then performed with classical coherent light. From 100 automated measurements we obtained a mean value of $\kappa^{(3)} = -4.677\times10^{-4}$ with a standard deviation of 8.394×10^{-4}, which is comparable to the current state of the art achieved with classical light [156–158, 163]. However, the ultimate goal of this project is to perform the test using genuine quantum particles. For this reason, the device has been sent to Munich, where the group of Prof. Vogl will carry out the measurements using single-photon sources based on color centers in the two-dimensional material hexagonal boron nitride. This approach is expected to suppress detector non-linearity and shot noise, thus potentially achieving even better results.

Finally, it is worth mentioning that a copy of this device was launched into space in June 2025 as part of the QUICK^3 space mission [159]. There, the same experiment will be performed under microgravity conditions, while at the same time demonstrating the feasibility of a complete quantum processor capable of generating, manipulating, and detecting quantum information at room temperature in a compact form factor, paving the way toward scalable quantum technologies. Although I did not participate directly in the fabrication of this device, I was responsible for its packaging. This involved gluing special input fibers with hBN flakes positioned on the fiber tips to generate single photons directly within the PIC, as well as gluing the output fiber, a

custom fiber incorporating a Bragg grating designed to block the pump light while transmitting the single-photon emission. The mission was fully successful: communication with the chip worked as expected, the chip behaved according to design, and a complete dataset was acquired.

CHAPTER 6

Photonic integrated circuit for heralded Bell's state generation

In this chapter, we present the realization of a device for the generation of heralded Bell states. Such a component represents a key enabler for advancing quantum technologies, as the ability to generate entangled photonic states is essential for a wide range of quantum protocols and applications. In this project, I contributed to both the fabrication and the characterization of the photonic chip, activities that were carried out in the laboratories of Politecnico di Milano. A second part of the research was conducted in collaboration with the group of Andrew White at the University of Queensland (Australia), where I spent a five-month research period. During this time, I was directly involved in the development of a demultiplexer setup, which constitutes a key component of the overall experimental apparatus.

6.1 Motivation

The heralded generation of Bell states plays a crucial role in implementing advanced quantum information protocols. Their unique correlations, which violate local realism and Bell-type inequalities, make them fundamental for applications ranging from fault-tolerant quantum computation [31, 165, 166] to device-independent quantum key distribution [44–46, 167], super-dense coding [168], and quantum-enhanced metrology [169].

In photonic platforms, the generation of such states is particularly challenging due to the negligible photon–photon interactions. However, Hong-Ou-Mandel interference [170], enables effective indirect interactions and the subsequent creation of entanglement between indistinguishable single photons. Heralded schemes exploit this mechanism to probabilistically generate entangled pairs while providing an event-ready signal that confirms their presence without consuming the state, in contrast to postselection techniques.

In integrated photonic circuits, qubits are typically encoded in the dual-rail (path) degree of freedom, where the quantum information is represented by the presence of the photon in one of two optical waveguides. This encoding naturally fits interferometric architectures, allowing for stable and precise control of phase shifts and interference between optical modes on-chip.

However, dual-rail encoding is generally unsuitable for free-space transmission, as the two modes propagate along physically distinct paths. In a turbulent medium such as the atmosphere, these paths experience independent optical path fluctuations, introducing an unknown relative phase between the modes. This leads to decoherence and makes the reliable transmission of dual-rail encoded qubits through free space impractical.

Since Bell states play a central role in many quantum communication protocols, such as quantum teleportation, entanglement swapping, and quantum key distribution, it is highly desirable to generate and transmit them efficiently. In particular, their use is crucial for long-distance quantum communication, which typically relies on free-space optical links to distribute entanglement over large distances. For this reason, we have integrated a path-to-polarization (P2P) converter on the chip, which enables the transition from the on-chip dual-rail encoding to a polarization encoding at the

output. Polarization encoding is much more practical for free-space channels, as both polarization modes experience the same optical path and remain stable even in the presence of atmospheric turbulence.

This design choice allows our platform to combine the robustness and scalability of dual-rail encoding for on-chip quantum state manipulation with the practicality of polarization encoding for long-distance quantum communication.

6.2 Preparation of heralded Bell states on photonic integrated circuits

Two-qubit maximally entangled states, commonly known as Bell states, constitute the simplest and most studied class of entangled quantum states. They are defined as

$$\begin{aligned} |\Phi^{\pm}\rangle &= \frac{1}{\sqrt{2}} \left(|00\rangle \pm |11\rangle\right), \\ |\Psi^{\pm}\rangle &= \frac{1}{\sqrt{2}} \left(|01\rangle \pm |10\rangle\right). \end{aligned} \tag{6.1}$$

These states form an orthonormal basis for the two-qubit Hilbert space. As mentioned in Section 1.1, since photons do not naturally interact with one another, entanglement in photonic platforms is generated by employing linear optical circuits together with the inherent nonlinearity of quantum measurement, which enables the probabilistic creation of entangled states. In particular, this work focus on a linear optical circuit implementing heralded entanglement generation rather than postselected schemes. Postselection only allows one to verify the presence of an entangled state a posteriori, at the cost of consuming the photons during detection, making the approach unsuitable for scalable architectures [171]. Heralding, on the other hand, provides an event-ready signal that confirms the successful generation of the desired Bell state without destroying it, thereby allowing its use in subsequent stages of a quantum protocol [172]. This feature is crucial for fusion-based and measurement-based models of photonic quantum computation, where small entangled resource states are combined into larger cluster states.

In general, linear heralded schemes are probabilistic and require significant experimental overheads, such as additional photons that are destroyed

during the heralding detection, and extra spatial modes where the heralding takes place. Different schemes can be distinguished by their success probability p, the total number of photons P, and the total number of spatial modes M. Among the best-known designs, some implementations of the 4P8M circuit can achieve a success probability of $p = 3/16$ [165, 173], depending on the adopted protocol, whereas the 4P6M layout reaches $p = 2/27$ [174]. An even more compact option is the 4P5M scheme, which attains $p = 1/9$ [175]. A 5P5M design based on a discrete Fourier transform achieves $p = 12/125$ [176]. Each of these architectures highlights a trade-off between circuit size, heralding probability, and detector requirements, motivating the development of integrated and resource-efficient solutions.

In this work, we focus on heralded Bell state generation using the 4P8M scheme, inspired by the design proposed in [172, 173]. This architecture achieves a generation probability of $p = 1/16$ for a fixed Bell's state and was chosen for its relative simplicity in fabrication. In fact, it does not require precise phase control between each component, which would require the fabrication of thermal shifters and complex calibration embedded within the chip. Furthermore, all directional couplers are implemented with 50:50 splitting ratios. Moreover, depending on the heralding outcomes, the same circuit is in principle capable of generating all four Bell states, thus providing a versatile resource.

6.3 Chip layout and working principle

The scheme of the device is reported in Fig. 6.1. It consists of eight waveguides, where qubits are encoded in pairs of modes using the path degree of freedom: a photon propagating in the upper (lower) waveguide of a pair represents the logical state $|0\rangle$ ($|1\rangle$). In this configuration, modes $(1, 2)$ and $(7, 8)$ define the two output qubits, while modes $(3, 4, 5, 6)$ serve as heralding channels. For instance, the state $|10101010\rangle$ in path encoding corresponds to the logical state $|0000\rangle$, where the central qubits are heralding and the external ones constitute the entangled pair.

The circuit is composed of a sequence of balanced 50:50 DCs and mode-swapping.

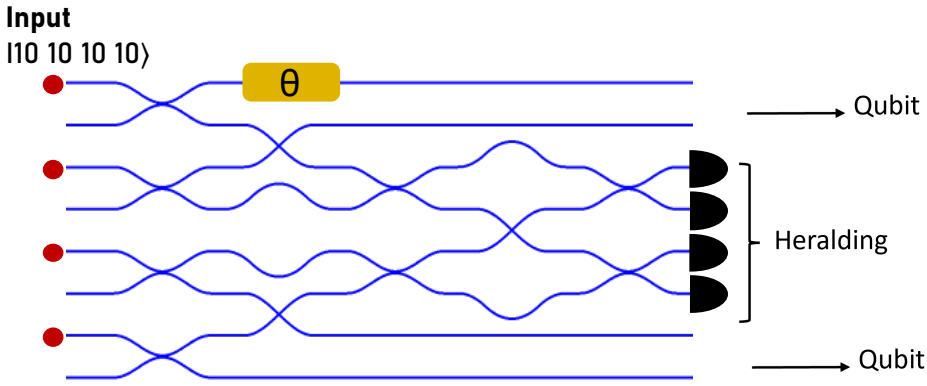

Figure 6.1: *Scheme for entangled Bell-state generation. The layout of the optical pathways is shown, where the two pair of external waveguides at the output represent the qubits, while the four central modes act as the heralding channels. A TOPS is highlighted in the yellow rectangle, enabling the control of the phase θ in the device.*

Each balanced DC acting on a pair of modes is described by the unitary

$$M_{\mathrm{DC}(i,j)} = \begin{bmatrix} \ddots & & & & \\ & \frac{1}{\sqrt{2}} & \frac{j}{\sqrt{2}} & & \\ & \frac{j}{\sqrt{2}} & \frac{1}{\sqrt{2}} & & \\ & & & \ddots & \end{bmatrix}, \tag{6.2}$$

where the 2×2 block acts on modes (i, j), while the identity is applied on all the remaining modes. Similarly, permutations are implemented by swap matrices of the form

$$M_{\mathrm{swap}(i,j)} = \begin{bmatrix} \ddots & & & & \\ & 0 & 1 & & \\ & 1 & 0 & & \\ & & & \ddots & \end{bmatrix}, \tag{6.3}$$

where the 2×2 block exchanges modes (i, j). In the implemented device, the first permutation swaps $(2, 3)$ and $(6, 7)$, while a second permutation exchanges $(4, 5)$.

The operation of the circuit can be summarized as follows. The input

state $|10101010\rangle$ is first initialized by four parallel DCs acting on all mode pairs $(1,2)$, $(3,4)$, $(5,6)$, and $(7,8)$. The photons then undergo the first permutation, given by $M_{\text{swap}(2,3)}$ and $M_{\text{swap}(6,7)}$. A second stage follows, in which DCs are applied on the central heralding modes $(3,4)$ and $(5,6)$. After this, the permutation $M_{\text{swap}(4,5)}$ is performed, and finally the same pair of DCs on $(3,4)$ and $(5,6)$ is repeated, completing the interferometric transformation.

In addition, a TOPS is placed on mode (1), represented by

$$M_{\text{phase}(1)} = \begin{bmatrix} e^{-j\theta} & 0 & \cdots & 0 \\ 0 & 1 & \cdots & 0 \\ \vdots & & \ddots & \vdots \\ 0 & 0 & \cdots & 1 \end{bmatrix}, \tag{6.4}$$

which provides tunable control of the phase of the generated entangled state.

Among all possible detection outcomes on the heralding modes, only four patterns lead to maximally entangled Bell states of the output qubits. In particular, detection events (1010) and (0101) on the four herald modes project the output qubit states onto

$$\Phi^{\theta} = \frac{1}{\sqrt{2}}\Big(|00\rangle + e^{j\theta}\,|11\rangle \Big), \tag{6.5}$$

whereas the patterns (1001) and (0110) project onto

$$\Psi^{\theta} = \frac{1}{\sqrt{2}}\Big(|01\rangle + e^{j\theta}\,|10\rangle \Big). \tag{6.6}$$

Each of the four successful heralding patterns occurs with a probability of $1/32$. Two of these patterns correspond to the same Bell-state projection, leading to an overall success probability of $1/16$ for the generation of that specific Bell state. By tuning the phase θ, the relative sign of the Bell state (e.g., $|\Phi^{+}\rangle$ or $|\Phi^{-}\rangle$) can be selected.

After the generation of the path-encoded Bell state, a P2P converter is mounted at the end facet of the PIC, as illustrated in Fig. 6.2. One converter

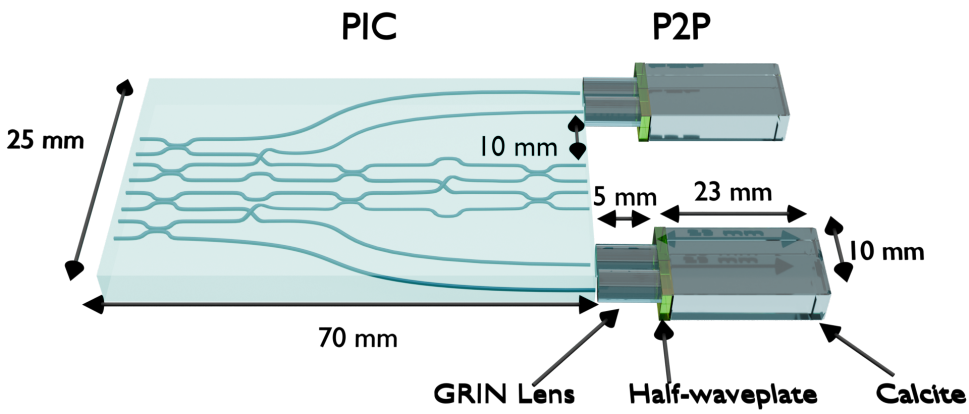

Figure 6.2: *Layout of the fully assembled device, including the integrated optical circuit and the path to polarization (P2P) converter. From the image, the overall footprint of the device and the three-dimensional nature of the waveguide crossing can be inferred.*

is used for each qubit and is aligned with modes $(1, 2)$ and $(7, 8)$. The device consists of two gradient-index (GRIN) lenses that collimate the light emerging from the waveguides, followed by a pair of half-wave plates (HWPs). The optical axis of the HWP corresponding to one mode is oriented at $0°$, preserving the input polarization, while the other is rotated by $45°$, thereby rotating the polarization by $90°$. In this way, the two spatial modes are mapped into orthogonal polarizations.

Subsequently, a calcite crystal is inserted. Owing to its high birefringence, the crystal is engineered with a length precisely chosen to compensate the spatial walk-off between the two beams, recombining them into a single spatial mode. As a result, at the output of the calcite, the photon emerges in a single spatial mode with a polarization state being identical (up to a global phase factor) to the qubit state in path encoding at inside the chip, enabling the use of the generated Bell state in free-space quantum communication experiments.

Inscription Parameters	
Substrate	EAGLE XG®
Laser system	Pharos
Wavelength	1030 nm
Repetition Rate	1 MHz
Objective	20× 0.5 NA (Water Imm.)
Inscription depth	35 μm
Pulse Energy	340 nJ
Translation speed	10 mm s^{-1}
Number of scans	3

Table 6.1: *Inscription parameters for the fabrication of the photonic chip.*

6.4 Chip fabrication and characterization

6.4.1 Optical circuit and TOPS

The realization of the device started with the optimization of the femtosecond laser writing conditions, with the goal of fabricating low-loss waveguides supporting single-mode operation at 925 nm, matching the emission of the quantum dot single-photon sources employed in the experiment. Waveguides were inscribed 35 µm beneath the surface of a 1 mm-thick aluminoborosilicate glass substrate (EAGLE XG®). The process was carried out using a Pharos femtosecond laser system (1 MHz repetition rate, 1030 nm wavelength), focused through a 0.5 NA water-immersion microscope objective. Remaining parameters were optimized, yielding propagation losses as low as 0.15 dB/cm for waveguides written with 340 nJ pulse energy, a translation speed of 10 mm/s, and three consecutive scans. Mode characterization confirmed single-mode guiding with a 5×5 μm^2 mode field. Bending losses remained negligible (< 0.1 dB/cm) for radii above 30 mm. The design of the directional couplers was subsequently optimized to achieve a balanced 50:50 splitting ratio. The waveguides were brought into proximity with an interaction distance d_{int} through sinusoidal S-bends. By setting the interaction length to zero, the footprint of the couplers was minimized, while the splitting ratio could be tuned by varying d_{int}. A balanced response was obtained for a bending radius of $R = 30$ mm and $d_{\text{int}} = 5.8$ μm. Experimental measurements confirmed that the fabricated couplers exhibited splitting ratios consistent with the target values. Three-dimensional crossings were

also engineered to limit additional insertion losses, using spline-shaped trajectories. At the crossing points, the waveguides were vertically displaced by ± 15 μm, a configuration that maintains smooth curvatures while suppressing optical cross-talk to levels below -50 dB, i.e., under the resolution of the measurement setup. The layout of the final optical circuit was conceived to be compatible with standard fiber-array interfacing. An inter-waveguide pitch of 127 µm was adopted at the input facet, matching the spacing of commercial V-groove arrays. Towards the output facet, the geometry was progressively expanded: the four outer modes corresponding to the two qubits were gradually displaced by spline trajectories to a distance of 1 cm from the central block of heralding waveguides (see Figure 6.2). This spacing was required to accommodate the path-to-polarization converters. In addition, the two qubit waveguides were further separated by 2 mm to match the 1 mm radius of the GRIN lenses. The use of spline profiles ensured smooth transitions, effectively suppressing bending-induced losses. As a result, the total length of the circuit was extended to 70 mm, leading to a final footprint of 70×25 mm^2. The four central heralding waveguides preserved the initial pitch of 127 µm along the entire device, allowing direct interfacing with commercial fiber arrays also at the output facet.

TOPSs are fabricated following the procedure described in 3.1.3, above the first and eighth waveguide near the end of the chip. Two microheaters were implemented for redundancy, each 6 mm long and 18 μm wide. The measured resistances were 150 Ω and 155 Ω for the heaters placed on the first and eighth waveguide, respectively. In this case no trenches were included, to simplify fabrication and because they were unnecessary: the large waveguide separation in the final section and the activation of only a single TOPS excluded risks of cross-talk or significant power dissipation.

Finally, 780-HP fiber arrays were glued to the input (8-mode, polarization-maintaining) and to the output (4-mode) facets of the device.

6.4.2 P2P converter

The P2P converter was then assembled from commercially available optical components. The pairs of GRIN lenses were optimized for 925 nm, premounted on a V-groove with a center-to-center spacing of 2.099 mm, 2 mm

diameter and 4.99 mm length. The remaining part of the module was supplied as a custom-assembled element, comprising two half-wave plates and a calcite beam-displacement rod. The calcite crystal featured a 10×10 mm^2 cross-section and a length of 20 ± 0.1 mm, with the optical axis oriented at $45° \pm 2°$ relative to the input/output facets, producing a beam separation parallel to the 10 mm edges. The crystal was cemented to a segmented low-order quartz retarder, providing a retardation of $1.5\,\lambda \pm \lambda/300$ at $\lambda = 925$ nm. The retarder was realized with two 10×5 mm^2 segments, with axes aligned at $0° \pm 0.1°$ and $45° \pm 0.1°$ to the polarization direction. The entire stack was enclosed between anti-reflection coated cover plates, resulting in a total length of 23.2 ± 0.1 mm. The specifications guaranteed a wavefront distortion in transmission below $\lambda/4$ and a beam deviation below 1'. The length of the calcite crystal was selected to precisely match the spatial walk-off corresponding to the displacement of the two optical modes. In practice, the GRIN lenses and the calcite rod were ordered first with the required specifications; based on these values, the spacing of the output waveguides was then calculated and fabricated accordingly. Finally, the two modules were precisely aligned using a six-axis hexapod stage and permanently fixed in place with adhesive. First, the two pairs of lenses were attached using an index-matching glue with the same refractive index as the glass. Subsequently, the calcite crystal was mounted onto the metallic support, which also hosted the PIC, and secured to the base with glue.

After assembly, the P2P module was characterized by measuring the spatial overlap between the two output modes, as shown in Fig. 6.3. This step proved to be nontrivial, as we observed that even a few micrometers of misalignment in the GRIN lenses resulted in slightly non-parallel beams, causing a residual divergence. Nevertheless, after a free-space propagation of 10 cm, the measured spatial overlap between the two modes reached 98.91% for the P2P assembly shown in Fig. 6.3a, and 87.41% for the configuration illustrated in Fig 6.3b. To achieve a perfect spatial superposition, a possible strategy would be to re-collect the beams into a single-mode fiber and subsequently re-collimate them into free space.

The overall losses were evaluated by injecting a calibrated optical power into each input and determining the ratio between the input power and the sum

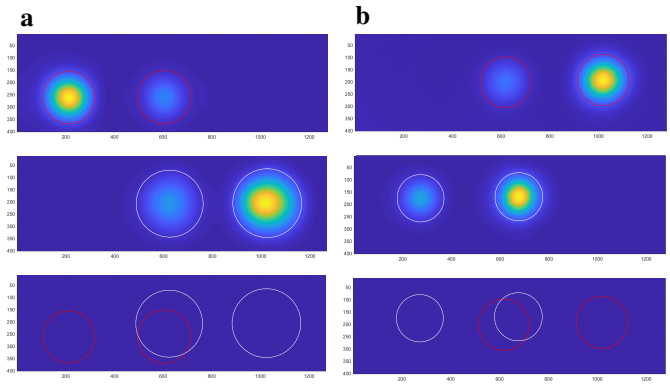

Figure 6.3: *Spatial mode characterization of the two P2P modules (***a** *and* **b***). The first row shows the output when light enters through the outermost qubit input pair. The second row corresponds to the output when light enters through the adjacent qubit pair. The third row represents only the overlap of the two previous modes, without any actual light, since the measurements were performed by illuminating one port at a time. The axes indicate the spatial positions x and y.*

of all output powers, including the four heralding outputs from the fibers and the two qubit free-space modes after the calcite. The average total loss from the fiber input to the outputs after the calcite/fiber stage was measured to be 2.1 ± 0.16 dB. These losses arise from fiber mating connections, propagation and bending within the chip, coupling losses due to mode mismatch, and additional contributions from the P2P assembly, mainly originating from the refractive index mismatch at the lens–air interface (only one such interface is considered, as the opposite side is glued directly to the chip with index-matching adhesive).

6.5 Experimental setup

Once the chip was assembled, I undertook a five-month secondment at the University of Queensland in Australia, under the supervision of Prof. Andrew White and Dr. Markus Rambach, to characterize the device and perform the experiments using true single photons.

The experimental setup used for this characterization is illustrated in Fig. 6.5 and can be divided into three main parts. The first stage comprises the single-photon source and the demultiplexing system. The source emits

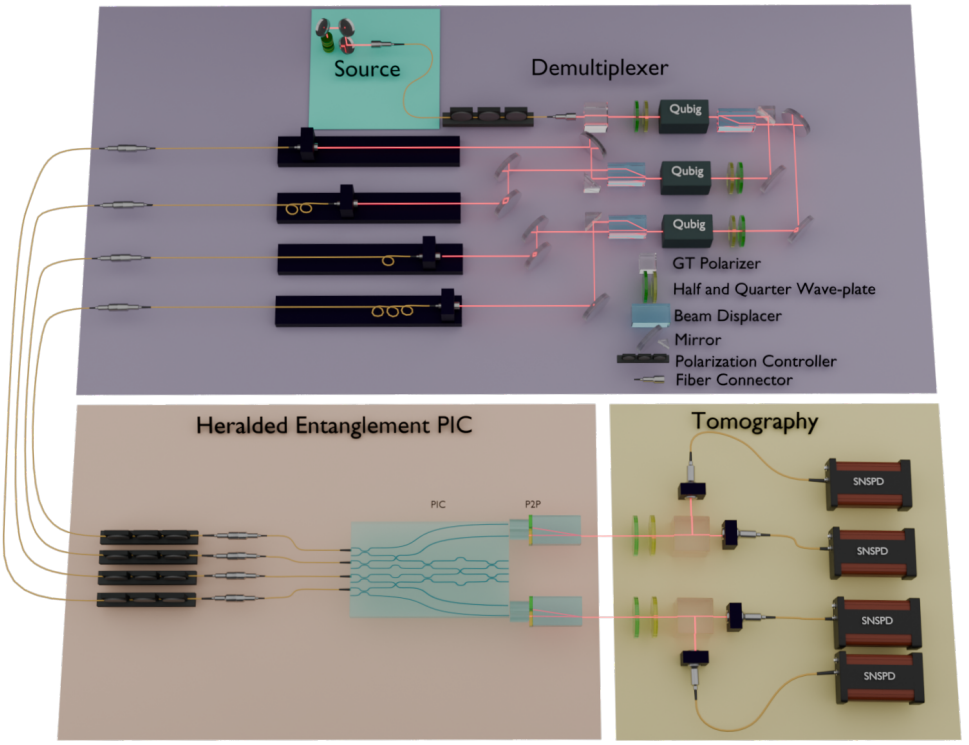

Figure 6.4: *Schematic of the overall experimental setup, consisting of three main stages: the source and demultiplexer (light blue and purple), the PIC for heralded entanglement generation (light brown), and the state tomography stage (yellow).*

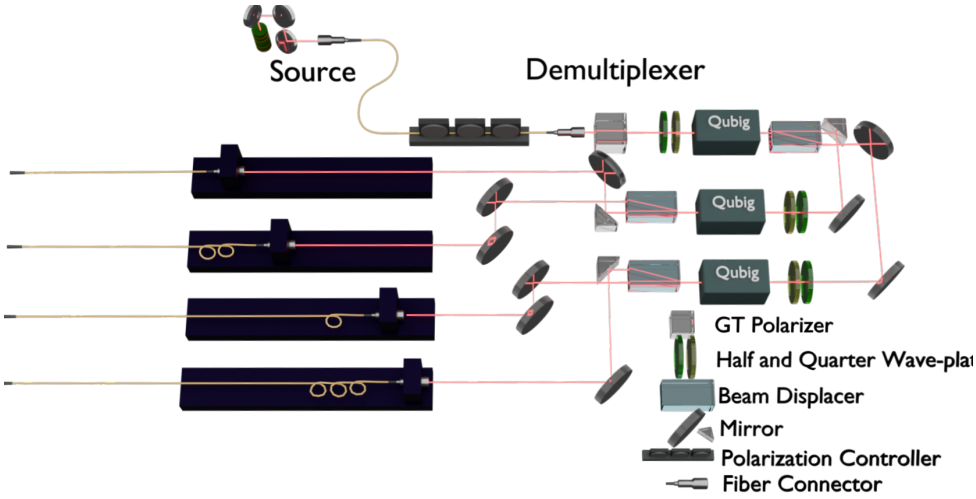

Figure 6.5: *Schematic of the source and demultiplexer stage. In this section, four temporally consecutive photons emitted by the QD are actively demultiplexed into four spatial modes, resulting in four photons simultaneously available in distinct optical paths. The label "Qubig" shown in the figure refers to the brand of the Pockels cells employed.*

photons sequentially in a single spatial mode with temporal separation, which are then redistributed by the demultiplexing stage into four distinct spatial modes, providing four photons simultaneously at the output to feed the PIC. In the second stage, the photonic device processes these inputs and generates two heralded entangled photons. The third and final stage is the tomography setup, which enables a complete characterization of the resulting quantum state.

6.5.1 Quantum dot and demultiplexing stage

The quantum dot device consists of self-assembled InGaAs structures embedded in an InAs wetting layer, surrounded by GaAs, and integrated into micropillar cavities with distributed Bragg reflectors to achieve Purcell enhancement. The devices are fabricated at Quandela and mounted on a photonic chip, which is maintained inside a cryostat at approximately 4 K. An applied electrical bias enables Stark tuning of the emission wavelength. The quantum dots are resonantly excited using a Ti:sapphire pulsed laser operating at 80 MHz, such that each pulse ideally generates a single photon. After collection and spectral filtering, the extracted single-photon stream is

delivered at a rate of about 1 MHz. The reduction from the original 80 MHz excitation rate is primarily due to the high coupling losses between the quantum dot and the collection fiber. The source exhibits excellent single-photon purity, with a measured second-order correlation value of $g^{(2)}(0) = 0.00536$. Our demultiplexing stage, shown in Fig. 6.5 and inspired by time-to-space photon routing schemes demonstrated in [177], operates as follows. Single photons emitted by the QD, one every 12.5 ns, are already coupled into a single-mode fiber equipped with a fiber polarization controller (FPC). After exiting the fiber, the photons are collimated into free space and pass through a Glan–Taylor polarizer. The combined use of the FPC and the Glan–Taylor ensures that the polarization of the photons is fully aligned with the transmission axis of the polarizer, thereby converting the entire signal into a well-defined polarization state without significant power loss. This stream of polarized single photons then enters a 40 MHz Pockels cell (from QUBIG), synchronized with the pulsed laser and driven by its dedicated driver, which alternately inverts the polarization of successive photons. A set of quarter- and half-wave plates is placed before the Pockels cell to ensure its correct operation. In particular, they align the polarization such that the driving signal modulates the crystal in the most effective way, approximating as closely as possible a square-wave modulation at 40 MHz, and thereby enabling the Pockels cell to switch the polarization state with high fidelity. The photons are then sent through a calcite beam displacer (BD), which spatially separates the two polarizations. Each of the resulting beams is directed by mirrors into a second, identical stage (Pockels cell + BD), this time driven at 20 MHz, thereby yielding four photons in four distinct spatial modes. The light is then coupled into single-mode fibers.

At this point the four photons are still temporally separated. To synchronize them, four delay lines are introduced. The fiber lengths are estimated using $\Delta L = \frac{c}{n}\Delta t$, where c is the speed of light, $n = 1.4568$ is the refractive index of the Thorlabs 780HP fiber, and $\Delta t = 12.5$ ns corresponds to the period between consecutive photons at an 80 MHz repetition rate. The fibers are cut and spliced to the appropriate lengths, and the delays are first verified using an optical time-domain reflectometer. Fine delay adjustments are then performed by mounting the fibers on 30 cm motorized translation

stages (Thorlabs LTS300).

6.5.2 PIC and tomography setup

After the demultiplexing stage, the four photons are guided through single-mode fibers, each equipped with a FPC to ensure identical polarization at the inputs of the PIC. This step is crucial to enable high-visibility quantum interference. The fibers are then connected to the heralded entanglement PIC. The four heralding modes are directly coupled to SPAD detectors, while the two polarization qubits are routed to a polarization tomography stage.

The tomography setup consists of a quarter-wave plate, a half-wave plate, and a polarizing beam splitter (PBS). This configuration allows projection of the qubits onto any basis of the Bloch sphere [178]. The transmitted and reflected outputs of the PBS are collected in single-mode fibers and detected with superconducting nanowire single-photon detectors (SNSPDs), enabling a complete reconstruction of the two-photon quantum state.

6.6 Conclusions and future perspectives

In this chapter, we have presented the design, fabrication, and characterization of a photonic integrated circuit for the heralded generation of Bell states, together with the experimental setups required for its operation. The chip, realized via FLM, exhibited an average overall insertion loss of about 2.1 dB from fiber to output. The integrated directional couplers achieved the targeted 50:50 splitting ratios, and the path-to-polarization converters were successfully implemented. Spatial mode characterization further confirmed a high overlap between the output beams, with measured values up to 98.9%, although a lower overlap of 87.4% was observed in the other qubit mode. Such imperfections could in principle affect the final fidelity of the generated entangled states, although quantifying this impact requires further investigation.

In addition to chip fabrication and testing in Milan, I also contributed to the development of the experimental setup in Australia, with a role in the construction of the demultiplexing stage and in the tomography stage. Together, these setups enable the delivery of four synchronized single photons to the

chip and provide the tools for reconstructing the generated states. As a future perspective, the next step will be the complete tomographic characterization of the output, which will establish the fidelity of the generated Bell states and fully validate the device.

CHAPTER 7

Tunable ring resonator via Femtosecond Laser Micromachining

In this last chapter, we report the first demonstration of a tunable ring resonator fabricated by FLM. This achievement marks the realization of a fundamental photonic component within the FLM platform, with potential applications in gyroscopes, optical filters, and sensing. The work has been carried out in collaboration with Prof. Marco Liscidini, from the Physics department of Università di Pavia. My contribution concerned both the fabrication and the characterization of the device, together with the master student Fabio Saretto, whom I supervise during this project.

7.1 Motivation

Optical resonators are among the most fundamental and versatile elements in integrated photonics, as they enable a broad range of applications spanning from filtering [179, 180] and modulation [181, 182] to sensing [183],

gyroscopy [184, 185], and nonlinear optics [186, 187]. A ring resonator consists of a waveguide curved into a closed loop, in which light can circulate multiple times. The resonant wavelengths are those for which the optical field completes an integer number of oscillations along the loop circumference, a condition set by the combined effect of the waveguide dispersion and the loop length. Coupling between the resonator and external circuits is typically achieved through evanescent interaction with one or more nearby access waveguides. Their realization is strongly dependent on the refractive index contrast offered by the platform and on the fabrication technology adopted. High-index-contrast systems such as silicon-on-insulator allow for compact rings with micrometer-scale radii, while in lower-contrast platforms such as silicon nitride, larger radii are required to suppress bending losses. In the case of FLM, the challenge becomes even more severe. Since FLM waveguides rely on a laser-induced refractive index change typically limited to 10^{-3}, very large bending radii on the order of millimeters or even centimeters are needed to preserve light confinement. Moreover, the inscription of a closed loop is particularly delicate: the writing beam must pass twice through the same region, creating an overlap zone that can introduce defects and additional scattering losses. These constraints have so far prevented the straightforward demonstration of FLM-based ring resonators, making their realization far from trivial. For these reasons, the successful fabrication of a tunable ring resonator in FLM represents a significant step forward in establishing this platform as a versatile technology. Our device not only demonstrates the feasibility of this fundamental building block, but also introduces tunability in both spectral response and coupling strength to the bus waveguides. This flexibility moves FLM resonators beyond simple proof-of-concept demonstrations, making them suitable for real applications and broadening their integration potential, not only within photonic circuits but also in other FLM-based systems such as microfluidic devices.

Inscription Parameters	
Substrate	EAGLE XG®
Laser system	Pharos
Wavelength	1030 nm
Repetition Rate	1 MHz
Objective	20× 0.5 NA (Water Imm.)
Inscription depth	50 μm
Pulse Energy	500 nJ
Translation speed	7 mm s^{-1}
Number of scans	4

Table 7.1: *Inscription parameters for low-loss, single-mode waveguides at 1550 nm for the integrated ring resonator. In the inset a microscope image of the cross-section of the waveguide. The scalebar corresponds to 30 µm.*

7.2 Design and fabrication

7.2.1 Chip layout

The peculiar design of the resonator is illustrated in Figure 7.1. As mentioned before, realize a resonator using FLM is not trivial, as the fabrication process inherently prevents writing closed loops: revisiting the same spatial location with the laser would compromise the previously modified material. To address this limitation, we adopted the layout shown in Fig. 7.1, which consists of a single waveguide that forms a racetrack loop and then couples back to itself through a MZI and then reaches the output by passing below the ring structure. Under this interpretation, light that couples into the loop effectively circulates within a resonant path, analogous to a traditional ring resonator. By controlling the thermal powers P_1 and P_2 dissipated on the TOPS it is possible to actively tune both the wavelength shift of the spectral resonances and the Q-factor of the device. This design leverages the three-dimensional capabilities of FLM to realize resonators formed by physically open waveguides, thereby avoiding the losses that may arise with the fabrication of fully closed loops through FLM.

7.2.2 Chip fabrication

Waveguide inscription was carried out using Pharos femtosecond laser system. The laser pulses, with a central wavelength of 1030 nm, a repetition

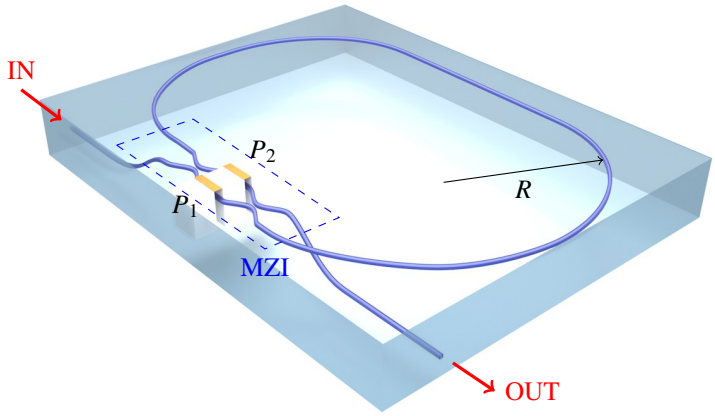

Figure 7.1: *Layout of the resonator. The waveguide, starting from the input port (IN) first forms a ring with a racetrack geometry, then couples back to itself through a MZI, and is finally brought to the output (OUT) port, passing underneath the ring structure. The MZI is equipped with two TOPS, one per each arm, consisting in metal resistors deposited and patterned on the substrate surface. Different electrical powers P_1 and P_2 can be dissipated on the resistors, enabling independent control on the MZI phases. To enhance thermal efficiency, U-trenches were ablated around the waveguide segments [98]. Total footprint* 5×6 cm^2.

rate of 1 MHz, and a pulse duration of 180 fs, were focused into a 1 mm-thick borosilicate glass substrate (Corning Eagle XG) through a 20× Zeiss water-immersion objective with a numerical aperture of 0.5. Furthermore, by exploiting the three-dimensionality of the waveguide paths, we also demonstrate the fabrication of several concentric resonators within the same glass chip: the straight sections of the waveguides are inscribed at a depth of 50 μm below the glass surface while the bent sections forming the rings are inscribed at 35 μm enabling vertical stacking without optical crosstalk. Figure 7.2 shows the geometric configuration used to concentrically inscribe multiple resonators. Specifically, two groups of ten resonators each were fabricated using two different fabrication recipes. The first recipe consists of a deposition energy of 500 nJ, a writing speed of 5 mm s^{-1}, and four overlapping scans. The second recipe is identical, except for the writing speed, which is increased to 7 mm s^{-1}. These two recipes were selected because both exhibited low propagation losses when guiding light at 1550 nm, both in straight and curved waveguides. Therefore, it was considered worthwhile to

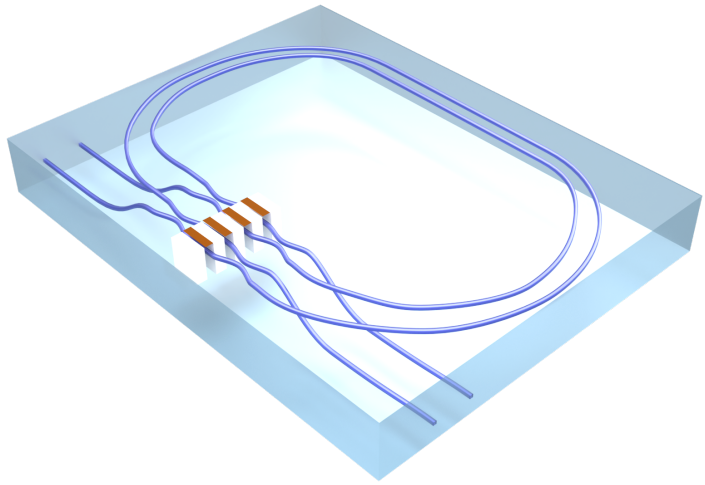

Figure 7.2: *Schematic representation of two concentric resonators, illustrating the geometry employed for the fabrication of multiple resonators arranged in a concentric configuration.*

test both approaches for the fabrication of the resonator loops. The first group was fabricated starting from a radius of 21 mm, with subsequent resonators created by reducing the radius in steps of 0.2 mm. Five of the resonators were inscribed using the first recipe, and the remaining five with the second. The second group was fabricated following the same procedure, but starting from a smaller initial radius of 18.6 mm. This design allows for the characterization of resonators fabricated under the same conditions as a function of the loop radius. After laser writing, the sample undergoes annealing in order to reduce the stress generated during laser writing and thus improving the optical properties of the waveguides [88]. Subsequently, in order to reconfigure the resonators, we fabricated TOPSs. As shown in Fig. 7.1, TOPS were placed on both arms of the MZI within the resonators. As shown in the picture 7.1 alongside each waveguide of the MZI, trenching was done using the FLM in order to thermally insulate the waveguide. This is necessary not only to reduce the power required to operate a MZI by almost an order of magnitude, but also to reduce thermal cross-talk [98].

The micro-heaters were fabricated by depositing a 100-nm-thick layer of chromium gold on the sample and subsequently patterning the shape of the resistors with the femtosecond laser [97]. In particular the TOPS of the MZI

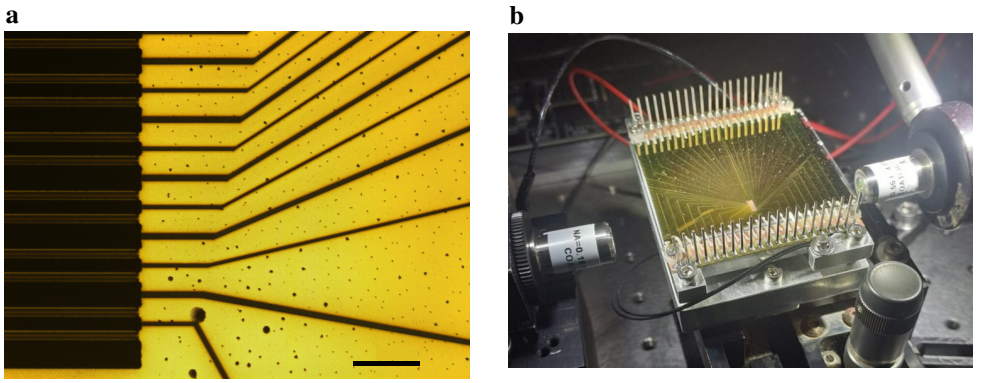

Figure 7.3: **a** *Photograph of the Cr+Au resistors and contact pads after femtosecond laser ablation. The scale bar corresponds to 200 µm.* **b** *Photograph of the fully assembled device, including the custom PCB and metal base.*

were fabricated for the entire length of the straight section of the MZI, i.e. 1.23 mm with a width of 24 µm. Finally, the gold pads were contacted to a custom-made PCB through conductive glue and the chip was glued onto a metal substrate, where a peltier is placed underneath it in order to maintain a stable temperature. The total footprint of the device is 5×6 cm.

7.3 Modeling of single waveguide resonator

We now describe in more detail the operating principles of the device sketched in Fig. 7.1. At its core lies an MZI that functions as a reconfigurable coupler, operating on the two distinct input waveguide modes a transformation described by the matrix $U = [u_{ij}]$. In particular, the coupling properties are governed by the phase shifts ϕ_1 and ϕ_2 accumulated in the two arms, which can be controlled by varying the corresponding TOPSs. In the ideal case of perfectly balanced (i.e. 50:50) directional couplers and negligible losses, the cross-coupling coefficient of the MZI is equal to (see Section 7.3.2):

$$u_{12} = u_{21} = te^{j\phi_{\mathrm{cm}}} = \cos\left(\frac{\Delta\phi}{2}\right) e^{j\phi_{\mathrm{cm}}}, \tag{7.1}$$

where $\phi_{\mathrm{cm}} = \frac{1}{2}(\phi_1 + \phi_2 + \pi)$ is the total phase accumulated in the MZI, and $\Delta\phi = \phi_1 - \phi_2$ is the phase difference between the two MZI arms. By taking into account the thermal crosstalk between the two TOPSs, the dependence

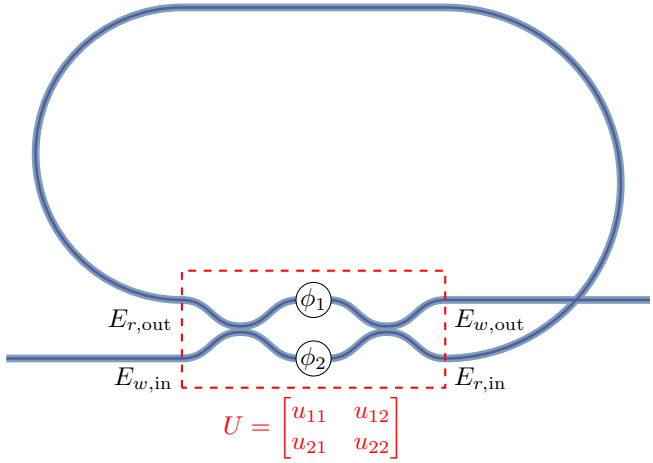

;

Figure 7.4: *Schematic representation (not to scale) of the FLM racetrack resonator. The MZI operates as a reconfigurable directional coupler implementing a transformation matrix U on the supported modes, controlled by the internal phase shifts ϕ_1 and ϕ_2 (highlighted in the figure). In this configuration, the input field from the input waveguide, $E_{w,in}$, enters the MZI, where it can be partially coupled to the port $E_{r,in}$, corresponding to the entrance of the ring resonator. After propagating along the racetrack section, the field $E_{r,out}$ is reinjected into the second input port of the MZI, leading to the output field from the waveguide, $E_{w,out}$.*

of ϕ_{cm} and $\Delta\phi$ on the dissipated electrical power P_1 and P_2 can be expressed as [97]:

$$\Delta\phi = \frac{2\pi}{\lambda_0}\left[a_1 P_1 + a_2 P_2 + \Delta L\right], \tag{7.2}$$

$$\phi_{\text{cm}} = \frac{2\pi}{\lambda_0}\left[b_1 P_1 + b_2 P_2 + L\right] + \frac{\pi}{2}, \tag{7.3}$$

where λ_0 is the light wavelength in vacuum, a_i and b_i are coefficients depending on the device geometry and material properties, L is an effective optical path length of the MZI (thus taking into account also the effect of the refractive index) and ΔL is the optical-length imbalance of the MZI arms introduced by fabrication tolerances.

The power transmission of the device is given by (see Section 7.3.1 and Ref. [188]):

$$\mathcal{T} = \frac{\alpha^2 + t^2 - 2\alpha t\cos(\theta_R + \phi_{\text{cm}})}{1 + \alpha^2 t^2 - 2\alpha t\cos(\theta_R + \phi_{\text{cm}})}, \tag{7.4}$$

where α is the amplitude transmission per round trip and θ_R is the phase accumulated per round-trip excluding the MZI section. Finally, it is convenient to associate the round-trip phase appearing in (7.4) with an effective total optical path length L_{tot} defined as

$$\theta_R + \phi_{cm} = \frac{2\pi}{\lambda_0} L_{\text{tot}}. \tag{7.5}$$

Since in our structure the round trip in the resonators includes the MZI, L_{tot} depends also on P_1 and P_2 (see (7.3)) and is not simply linked to the physical length of the device. Yet, as in the case of conventional ring resonators, a resonant wavelength $\lambda_{0,m}$ satisfies the relation $m\lambda_{0,m} = L_{\text{tot}}$, with m indicating the resonance order. Similarly, the device transmission shows dips that are, for a sufficiently small spectral range, periodic in wavelength with a free spectral range FSR $= \frac{\bar{\lambda}_0^2}{L_{\text{tot}}}$, where $\bar{\lambda}_0$ is the mean wavelength in vacuum in the interval of interest (here, it can safely be taken as $\bar{\lambda}_0 = 1550$ nm).

Another figure of merit characterizing the performance of optical resonators is the Q factor, defined as the ratio between the resonance frequency and the full width at half maximum (FWHM) of the corresponding spectral dip. In our case one can show that [189]:

$$Q = \frac{\lambda}{\text{FWHM}} = \frac{\pi L_{tot}}{\lambda} \left(\arccos \frac{2\alpha|t|}{1 + \alpha^2 |t|^2} \right)^{-1} \tag{7.6}$$

This parameter is intrinsically related both to the losses and to the optical length of the loop: lower losses and longer paths result in narrower resonances (i.e. smaller FWHM) and hence higher Q values.

Importantly, the common phase ϕ_{cm} basically determines a shift in the resonances. On the other hand the phase difference $\Delta\phi$ governs $|t|$ and thus modulates the depth of the transmission dips and the Q factor. Critical coupling is achieved when the MZI transmission equals the ring transmission, namely $|t| = \alpha$; in this condition complete destructive interference ($\mathcal{T} = 0$) is achieved at resonance.

7.3.1 The coupled-resonator transfer function

For completeness, we outline the derivation of (7.4). The coupling between the fields at the MZI ports is

$$\begin{bmatrix} E_{w,\text{out}} \\ E_{r,\text{in}} \end{bmatrix} = U \begin{bmatrix} E_{w,\text{in}} \\ E_{r,\text{out}} \end{bmatrix} = e^{j\phi} \begin{bmatrix} t & jk \\ jk^* & t \end{bmatrix} \begin{bmatrix} E_{w,\text{in}} \\ E_{r,\text{out}} \end{bmatrix}, \tag{7.7}$$

where E_w and E_r are the complex field amplitudes in the part of waveguide exiting directly the resonator and in the part of waveguide that travels the racetrack (see labels in Fig. 7.4), while t and k denote the transmission and reflection coefficients and ϕ is a phase term. The condition for U to be a unitary matrix implies $t^2 + kk^* = 1$.

The field circulating in the round-trip satisfies

$$E_{r,\text{out}} = \alpha\, e^{j\theta_R} E_{r,\text{in}}, \tag{7.8}$$

with $\alpha \in \mathbb{R}$ the round-trip amplitude transmission and $\theta_R \in \mathbb{R}$ the round-trip phase (excluding the MZI section). Substituting (7.8) in (7.7) we obtain:

$$E_{r,\text{in}} = jk^* e^{j\phi} E_{w,\text{in}} + te^{j\phi} E_{r,\text{out}} = jk^* e^{j\phi} E_{w,\text{in}} + t\alpha e^{j(\theta_R+\phi)} E_{r,\text{in}} \tag{7.9}$$

$$E_{r,\text{in}} = \frac{jk^* e^{j\phi}}{1 - t\alpha e^{j(\theta_R+\phi)}} E_{w,\text{in}} \tag{7.10}$$

and again exploiting (7.7):

$$\begin{aligned} E_{w,\text{out}} &= te^{j\phi} E_{w,\text{in}} + jke^{j\phi} E_{r,\text{out}} = te^{j\phi} E_{w,\text{in}} + jk\alpha e^{j(\theta_R+\phi)} E_{r,\text{in}} = \\ &= te^{j\phi} E_{w,\text{in}} - \frac{kk^*\alpha e^{j(\theta_R+2\phi)}}{1 - t\alpha e^{j(\theta_R+\phi)}} E_{w,\text{in}} = \frac{te^{j\phi} - t^2\alpha e^{j(\theta_R+2\phi)} - kk^*\alpha e^{j(\theta_R+2\phi)}}{1 - t\alpha e^{j(\theta_R+\phi)}} E_{w,\text{in}} = \\ &= \frac{te^{j\phi} - \alpha e^{j(\theta_R+2\phi)}}{1 - t\alpha e^{j(\theta_R+\phi)}} E_{w,\text{in}} \end{aligned} \tag{7.11}$$

The field transmission coefficient of the whole device is thus given by:

$$\tau = e^{j\phi} \frac{t - \alpha e^{j(\theta_R+\phi)}}{1 - t\alpha e^{j(\theta_R+\phi)}} \tag{7.12}$$

The power transmission coefficient on the other hand is the squared modulus

of the former, namely:

$$\mathcal{T} = \left| \frac{t - \alpha e^{j(\theta_R+\phi)}}{1 - t\alpha e^{j(\theta_R+\phi)}} \right|^2 = \frac{(t - \alpha e^{-j(\theta_R+\phi)})(t - \alpha e^{j(\theta_R+\phi)})}{(1 - t\alpha e^{-j(\theta_R+\phi)})(1 - t\alpha e^{j(\theta_R+\phi)})} =$$
$$= \frac{t^2 + \alpha^2 - t\alpha e^{j(\theta_R+\phi)} - t\alpha e^{-j(\theta_R+\phi)}}{1 + \alpha^2 t^2 - t\alpha e^{-j(\theta_R+\phi)} - t\alpha e^{j(\theta_R+\phi)}} = \frac{t^2 + \alpha^2 - 2\,\Re\{t\alpha e^{-j(\theta_R+\phi)}\}}{1 + \alpha^2 t^2 - 2\,\Re\{t\alpha e^{-j(\theta_R+\phi)}\}} \tag{7.13}$$

We observe that

$$\Re\{t\alpha e^{-j(\theta_R+\phi)}\} = t\alpha \cos(\theta_R + \phi) \tag{7.14}$$

therefore we can finally write:

$$\mathcal{T} = \frac{t^2 + \alpha^2 - 2\alpha t \cos(\theta_R + \phi)}{1 + \alpha^2 t^2 - 2\alpha t \cos(\theta_R + \phi)} \tag{7.15}$$

7.3.2 Coupling matrix for the MZI

We now derive (7.1). Consider an MZI with two identical (not necessarily balanced) DC and arm phases ϕ_1 and ϕ_2. Each coupler is described by

$$U_{DC} = \begin{bmatrix} \eta & j\sqrt{1-\eta^2} \\ j\sqrt{1-\eta^2} & \eta \end{bmatrix} \tag{7.16}$$

with η being a real parameter such that $0 \leq \eta \leq 1$. In fact, η^2 indicates the power transmission coefficient of the coupler on the same waveguide. The case of balanced couplers corresponds to $\eta = \sqrt{1-\eta^2} = \frac{\sqrt{2}}{2}$.

The matrix U describing the full interferometer is written as:

$$
\begin{aligned}
U &= \begin{bmatrix} 0 & 1 \\ 1 & 0 \end{bmatrix} \begin{bmatrix} \eta & j\sqrt{1-\eta^2} \\ j\sqrt{1-\eta^2} & \eta \end{bmatrix} \begin{bmatrix} e^{j\phi_1} & 0 \\ 0 & e^{j\phi_2} \end{bmatrix} \begin{bmatrix} \eta & j\sqrt{1-\eta^2} \\ j\sqrt{1-\eta^2} & \eta \end{bmatrix} = \\
&= \begin{bmatrix} j\eta\sqrt{1-\eta^2}(e^{j\phi_1}+e^{j\phi_2}) & \eta^2(e^{j\phi_1}+e^{j\phi_2}) - e^{j\phi_1} \\ \eta^2(e^{j\phi_1}+e^{j\phi_2}) - e^{j\phi_2} & j\eta\sqrt{1-\eta^2}(e^{j\phi_1}+e^{j\phi_2}) \end{bmatrix} = \\
&= e^{j\phi_{cm}} \begin{bmatrix} 2\eta\sqrt{1-\eta^2}\cos\left(\frac{\Delta\phi}{2}\right) & -\sin\left(\frac{\Delta\phi}{2}\right) - j(2\eta^2-1)\cos\left(\frac{\Delta\phi}{2}\right) \\ \sin\left(\frac{\Delta\phi}{2}\right) - j(2\eta^2-1)\cos\left(\frac{\Delta\phi}{2}\right) & 2\eta\sqrt{1-\eta^2}\cos\left(\frac{\Delta\phi}{2}\right) \end{bmatrix}
\end{aligned}
\tag{7.17}
$$

where:

$$
\Delta\phi = \phi_1 - \phi_2 \qquad\qquad \phi_{cm} = \frac{1}{2}\left(\phi_1 + \phi_2 + \pi\right),
$$

Note that the matrix $\begin{bmatrix} 0 & 1 \\ 1 & 0 \end{bmatrix}$ has been added in the multiplication to keep labeling of input and output fields consistent with Figure 7.4. Comparing the matrix in (7.7) with the one (7.17) we note that they have indeed the same form if we take:

$$
t = 2\eta\sqrt{1-\eta^2}\cos\left(\frac{\Delta\phi}{2}\right) \qquad\qquad \phi = \phi_{cm} \tag{7.18}
$$

.

In the case of ideal balanced couplers $\eta = \sqrt{2}/2$ we can write the cross-coupling coefficient of the MZI as:

$$
u_{12} = u_{21} = te^{j\phi_{cm}} = \cos\left(\frac{\Delta\phi}{2}\right)e^{j\phi_{cm}} \tag{7.19}
$$

7.4 Results

All the fabricated devices were characterized by recording their transmission spectra under different coupling conditions, i.e. for different values of $|t|$. Horizontally polarized coherent light from a tunable C-band laser source (Santec TLS-570) was coupled into the device input through an aspherical

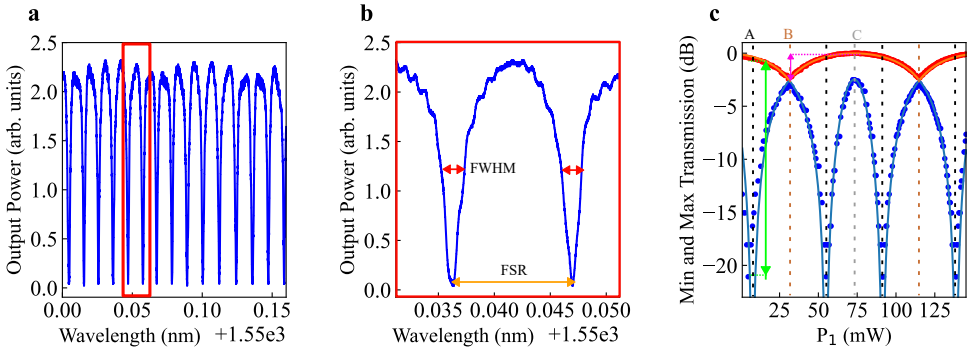

Figure 7.5: *Characterization of the spectral response of the resonator.* **a** *Optical power of the resonator as a function of wavelength under critical coupling conditions. Multiple resonance dips are visible over a span of 160 pm.* **b** *Zoom-in of the spectral region highlighted by the red rectangle in* **a**, *showing the shape and depth of individual resonance fringes, with the FWHM and FSR indicated by red and orange arrows, respectively.* **c** *Maximum (red line) and minimum (blue line) transmission values extracted from the spectra as the voltage applied to P_1 is varied, thereby tuning the coupling coefficient t. The dotted line labeled A (black), B (brown), C (grey) correspond to $|t| = \alpha$ (critical coupling condition), strong undercoupling ($|t| \sim 1$) and strong overcoupling ($|t| \sim 0$), respectively. The purple arrow indicates the internal losses of the ring, while the green arrow marks the extinction ratio achieved experimentally at critical coupling.*

lens (NA = 0.18). The transmitted signal was collected from the output port with another aspherical lens (NA = 0.4) and sent to an amplified photodiode (Thorlabs PDA10CS2).

7.4.1 Device characterization

The laser wavelength was continuously swept over a 160 pm range starting at 1550.000 nm, with a scanning speed of 1 nm/s and a wavelength resolution of 0.2 pm, while the photodiode output was simultaneously recorded with a digital oscilloscope. An example of the resulting transmission spectrum is reported in Fig. 7.5a. To investigate different coupling regimes, corresponding to different values of $|t|$, we varied the electrical power dissipated in the first thermo-optic phase shifter (P_1), while keeping $P_2 = 0$.

From each acquired spectrum, both the FWHM and the FSR of the resonance dips were extracted, as the averages of the linewidths and the separations of the dips across the scanned wavelength interval (see also Fig. 7.5b). In addition, we determined the minimum (V_{min}) and maximum (V_{max}) trans-

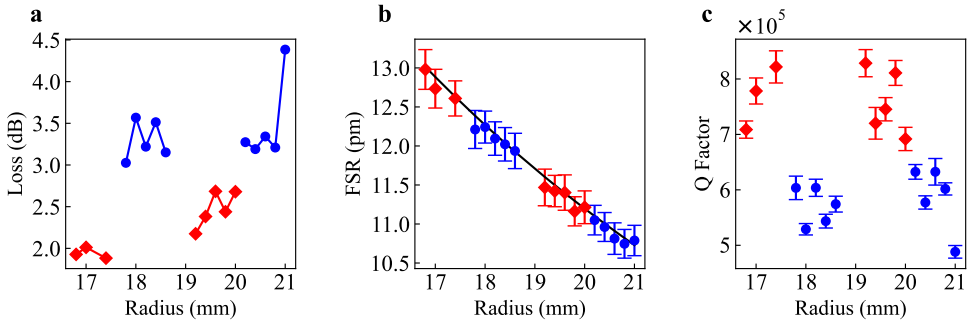

Figure 7.6: *Characterization of all resonators as a function of the ring radius, where blue dotted markers represent the values obtained with a writing speed of 5 mm s^{-1}, while red diamonds correspond to those fabricated at 7 mm s^{-1}.* **a** *Measured round-trip losses of the ring resonator.* **b** *Free Spectral Range (FSR), where the green line represents the theoretical prediction based on the relation FSR = $\frac{\bar{\lambda}^2}{L_{tot}}$, and the data points indicate measured values, calculated by averaging the separation between resonance dips detected over the scanned wavelength range.* **c** *Quality factor at critical coupling of each resonator, extracted from the FWHM under critical coupling conditions.*

mitted intensities from each spectrum. Figure 7.5c reports $V_{\min}$ and $V_{\max}$ as a function of P_1 (blue and red curves, respectively), in the case of the device with $R = 19.8$ mm. The extrema of the red curve correspond to the limiting cases of minimal coupling ($|t| \sim 1$) and maximal coupling ($|t| \sim 0$) into the ring.

These values allow us to estimate the internal round-trip losses of the resonator through the relation

$$\left.\frac{1}{\alpha^2}\right|_{\mathrm{dB}} = -10\log_{10}\left(\frac{\min\{V_{\max}\}}{\max\{V_{\max}\}}\right), \tag{7.20}$$

where α denotes the round-trip amplitude transmission.

The extracted losses are reported in Fig. 7.6a for all fabricated devices. The loss increases with the curvature radius, primarily because of the longer propagation length, indicating that waveguide propagation losses dominate over additional bending losses for the tested radii. Devices written at a speed of 7 mm/s show consistently improved performance, with overall losses below 3 dB. In particular, the device with $R = 17.4$ mm exhibits the lowest measured loss, about 1.9 dB, for a loop length of 127.6 mm.

The vertical separation between the red and blue curves in Fig. 7.5c

corresponds to the extinction ratio of the resonances for a given P_1. The maximum extinction ratio is observed at the critical coupling condition, where $|t| = \alpha$, resulting in complete destructive interference at resonance ($T = 0$). If the directional couplers of the MZI were perfectly balanced, by varying P_1 we would be able to scan the full interval of values of $|t|$ from 0 to 1 following precisely (7.1); in this ideal case, the maxima of the blue curve would touch the red curve, resulting from a flat transmission spectrum at those points. The distance between the curves still observed in those points indicates that $|t| = 0$ and $|t| = 1$ cannot be achieved precisely due to imperfections in the directional couplers of the MZI. In fact, we also report as a solid line the fit from a theoretical model which includes the possibility of unbalanced couplers (but still equal one to the other) composing the MZI. As shown in Fig. 7.5c, the experimental points are well reproduced by assuming 64:36 power splitting ratio of the individual couplers. This improved theoretical model would still predict vanishing transmission at the minima, whereas in practice a finite residual background is observed. This is likely due to the limited spectral bandwidth of the tunable laser; other small deviations between the data and the fitted curve are attributable to the non uniform wavelength scanning of the laser.

Figure 7.6b shows the measured FSR values for all devices, together with a theoretical curve calculated as

$$FSR = \frac{\bar{\lambda}^2}{nL},$$

with $n = 1.49$ [190] and L the nominal optical length of the loop, including both the racetrack and the MZI arms.

Finally, Fig. 7.6c reports the quality factor Q at critical coupling of all devices, extracted from the measured FWHM at critical coupling. Inverting Eq. (7.6) using these Q values provides an independent estimate of loop losses, in good agreement with the direct measurements. The best-performing device exhibits $Q \approx 8.3 \times 10^5$.

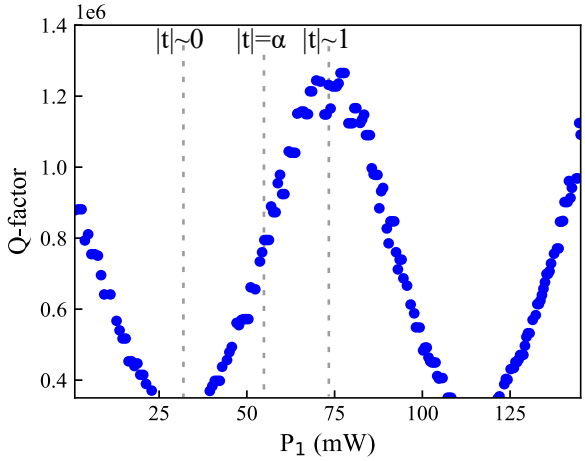

Figure 7.7: *Q factor as a function of dissipated power P_1, illustrating the transition between coupling regimes, from strong overcoupling ($|t| \sim 0$) to strong undercoupling ($|t| \sim 1$), passing from critical coupling ($|t| = \alpha$). The highest Q factor is observed in undercoupling regime. No data points are shown at the minima, as the transmission spectrum becomes flat in those regions, preventing the identification of a resonance dip and, consequently, the measurement of a meaningful FWHM.*

7.4.2 Tunability of Q factor and resonance shift

As expected, the Q factor depends on the coupling regime, which in our devices can be tuned actively through the MZI. Figure 7.7 shows the Q factor as a function of P_1 for the device with $R = 19.8$ mm. The plot highlights three regimes: critical coupling ($|t| = \alpha$), strong overcoupling ($|t| \approx 0$), and strong undercoupling ($|t| \approx 1$). The highest Q is achieved in the undercoupling regime. No data points are reported at the transmission minima, as the spectrum becomes flat in those regions, preventing a meaningful extraction of the resonance linewidth.

Moreover, we demonstrate that simultaneous actuation of both TOPSs enables tuning of the resonance positions. To this end, we varied the power P_2 on the second TOPS while adjusting P_1 according to

$$P_1 = P_{1,\mathrm{cc}} - \frac{a_2}{a_1} P_2, \tag{7.21}$$

where $P_{1,\mathrm{cc}}$ is the power required to reach critical coupling when $P_2 = 0$, i.e.

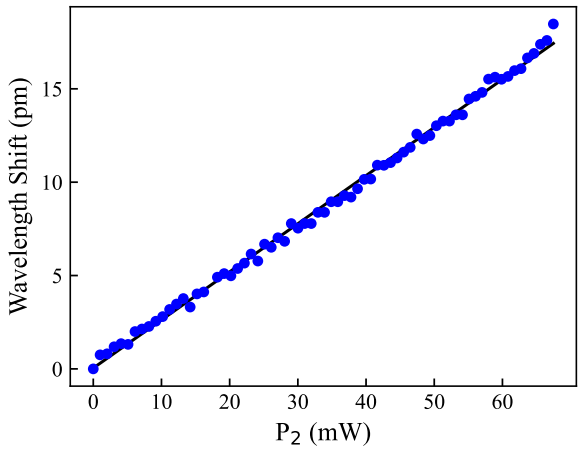

Figure 7.8: *Diagram showing the resonance shift as a function of the power dissipated P_2. The data show a clear linear trend, highlighted by the black linear fit.*

the condition satisfying

$$\frac{2\pi}{\lambda}(a_1 P_{1,\mathrm{cc}} + \Delta L_0) = \Delta\phi_{\mathrm{cc}}, \qquad |t| = \alpha.$$

In this way, the differential phase $\Delta\phi$ is kept constant, preserving the critical coupling condition, while the common-mode phase ϕ_{cm} is varied, effectively tuning the total phase accumulated in the loop. For each P_2, the transmission spectrum was measured and cross-correlated with a reference spectrum at $P_2 = 0$, in order to accurately extract the resonance shift. Results are shown in Fig. 7.8, together with a linear fit. A tuning range of more than 15 pm is achieved, i.e. exceeding one free spectral range (here ~11 pm), demonstrating full tunability of the resonance positions. The coefficients a_1 and a_2 were obtained from a prior calibration, performed by activating each TOPS individually and scanning the dissipated power, thereby tuning the coupling coefficient. Recalling (7.4) three operating points can be identified. The conditions $t = 1$ and $t = 0$ occur at $\Delta\phi = 0 + 2k\pi$ and $\Delta\phi = \pi + 2k\pi$ corresponding to the maximum and minimum of the off-resonance resonator transmission (B and C point of Fig. 7.5c). A third reference point is provided by the critical coupling condition, where the resonator is on resonance and the transmission reaches its minimum, referred to A in Figure 7.5c. In this case, $|t|^2 = \alpha^2$ and the corresponding MZI phase is $\Delta\phi = \pm 2\arccos(\alpha) + 2k\pi$.

From Fig.7.5c, we extract the powers P_0, P_π, and P_{cc} corresponding to these three phase values. Using these reference points, the dissipated power can be related to the differential phase through a linear regression, yielding

$$\Delta\phi(P_i) = a_i P_i + \Delta\phi_0, \qquad i = 1, 2. \tag{7.22}$$

The same procedure is then repeated for the second heater. Owing to the symmetric geometry of the two resistors located on opposite interferometer arms, one expects coefficients of comparable magnitude but opposite sign.

7.5 Conclusions and future perspectives

In this chapter we have demonstrated the first tunable integrated ring resonator fabricated with FLM, achieving a Q factor at critical coupling exceeding 8×10^5. By driving the two TOPSs, we achieved precise tuning of the resonance wavelength over more than one FSR, together with active control of the Q factor.

These results highlight the versatility of our device and its potential for applications requiring reconfigurable spectral responses, such as tunable optical filters, gyroscopes, and integrated sensing systems. Thanks to the intrinsically low thermo-optic coefficient of silica glass and the engineered heat confinement provided by our microstructured TOPSs, the platform may offers improved thermal stability compared to silicon-based technologies.

Overall, this work paves the way for a new class of integrated photonic devices that combine ring resonators with three-dimensional optical circuits and even hybrid optofluidic components, uniquely enabled by the flexibility of FLM technology.

CHAPTER 8

Conclusions

In this thesis, we have shown the potential of FLM as a valuable and versatile technique for the fabrication of PICs. This technology proves advantageous not only for research-oriented applications, thanks to its rapid prototyping capabilities, high design flexibility, and fabrication versatility, but also for real-world implementations, as demonstrated by its growing adoption in areas such as quantum communication. Throughout this study, we have exploited and emphasized the main advantages of this fabrication technique compared to other PIC technologies, namely, its intrinsic three-dimensional structuring capability, the ability to produce low and engineerable birefringence, and the implementation of efficient reconfigurable MZIs. In addition, FLM enables the fabrication of devices with low overall insertion losses, underscoring its suitability for integrated photonic quantum systems. Leveraging these advantages, we developed two photonic devices for quantum communication applications. The first was a time-bin QKD receiver, in which we also demonstrated how the birefringence of FLM-fabricated devices can be engi-

neered and controlled. The second was an heterodyne receiver developed for CV-QKD and CV-QRNG, where stable and reliable MZIs were exploited to achieve high-performance heterodyne detection.

Subsequently, we presented two devices aimed at inspiring and envisioning scalable photonic systems. The first focused on the efficient coupling of an FLM-fabricated PIC to a SPAD array, achieving high system detection efficiency through the combination of two custom technologies, each optimized to deliver the best possible performance. The second device consisted of an integrated three-arm interferometer used to test a fundamental principle of quantum mechanics, namely the Born rule. This device was implemented with efficient MZIs, exhibiting high optical extinction ratios, demonstrating the excellent performance achievable with FLM technology. This device also represents a step toward compact photonic systems integrating single-photon sources, interferometers, and detectors, as discussed at the end of that chapter.

Following this, we explored a system for the generation of heralded entangled Bell states. The complete system comprises a quantum dot source, a demultiplexing stage, and a photonic chip that converts four simultaneous photons into two entangled photons with two heralding signals. The PIC, which also integrates a path-to-polarization conversion section, is subsequently coupled to a polarization quantum-state tomography setup for the final state characterization.

Finally, we demonstrated the realization of a tunable ring resonator fabricated via FLM, thereby adding a resonant element to this platform. This work paves the way for a new class of integrated photonic devices that combine ring resonators with three-dimensional optical circuits and even hybrid optofluidic components, uniquely enabled by the flexibility of FLM technology. This work finds potential applications in systems requiring reconfigurable spectral functionalities, including tunable optical filters, optical gyroscopes, and integrated photonic sensing platforms.

Overall, these results clearly demonstrate the remarkable potential of FLM as a powerful and versatile platform for the realization of complex and high-performance integrated photonic devices, offering unprecedented design freedom, versatility, and performance for both classical and quantum applications.

Publications and Conferences

Publications

- G. Gualandi, S. Atzeni, M. Gardina, A. Caime, G. Corrielli, I. Labanca, A. Gulinatti, I. Rech, R. Osellame, G. Acconcia, F. Ceccarelli, "Laser-written reconfigurable photonic integrated circuit directly coupled to a single-photon avalanche diode array," *Light: Science & Applications*, 2025, DOI: 10.1038/s41377-025-01854-6.
- A. Peri[†], G. Gualandi[†], T. Bertapelle, M. Sabatini, G. Corrielli, Y. Piétri, D. G. Marangon, G. Vallone, P. Villoresi, R. Osellame, M. Avesani, "High-Performance Heterodyne Receiver for Quantum Information Processing in a Laser Written Integrated Photonic Platform," *Advanced Photonics*, 2026, DOI: 10.1117/1.AP.8.1.016009.
- G. Gualandi, F. Saretto, D. Pedroli, G. Corrielli, M. Liscidini, R. Osellame, A. Crespi, "Tunable integrated ring resonators by femtosecond laser micromachining,"
arXiv:2511.16490 (2025), DOI: 10.48550/arXiv.2511.16490.
- M. A. Pereira, G. Gualandi, R. Sax, A. Boaron, R. Houlmann, R. Osellame, R. Thew, H. Zbinden, "Quantum key distribution over a metropolitan network using an integrated photonics based prototype," *arXiv*: 2602.17227 (2026), DOI:10.48550/arXiv.2602.17227.

†These authors contributed equally to this work.

* Regarding the experiments on Born's rule and the Bell-state generation measurements are still ongoing, and manuscripts will be prepared as soon as the measurements are completed.

Conference presentations and proceedings

- G. Gualandi*, S. Atzeni, M. Gardina, A. Caime, G. Corrielli, I. Labanca, A. Gulinatti, R. Osellame, G. Acconcia, F. Ceccarelli, "Direct coupling of a laser-written photonic integrated circuit to a SPAD array," *International SPAD Sensor Workshop* (2024), Trento, Italy.
- G. Gualandi*, J. Krause, R. Osellame, T. Vogl, G. Corrielli, "Reconfigurable integrated photonic device to test Born's rule," in *Proceedings of SPIE* (Frontiers in Ultrafast Optics: Biomedical, Scientific, and Industrial Applications), San Francisco, CA, USA, 2025. DOI: 10.1117/12.3041781.
- G. Gualandi, S. Atzeni, M. Gardina, A. Caime, G. Corrielli, I. Labanca, A. Gulinatti, I. Rech, R. Osellame, G. Acconcia, F. Ceccarelli, "Interfacing a laser-written programmable photonic integrated circuit with a silicon SPAD array," in *Proceedings of SPIE* (SPIE Photonics West, Frontiers in Ultrafast Optics: Biomedical, Scientific, and Industrial Applications), San Francisco, CA, USA, 2025, DOI: 10.1117/12.3043740.

*personal oral contribution to the conference.

Ringraziamenti

Giunti alla fine di questa esperienza vorrei ringraziare chi mi ha aiutato durante questo percorso. Sono stati 3 anni intensi ma molto felici, ricchi di esperienze che mi hanno aiutato a crescere sia personalmente che lavorativamente. Penso che la scelta di intraprendere un dottorato sia stata fondamentale e decisiva per la persona che sono oggi e che mi abbia aperto le porte al futuro che desideravo, e per questo penso sia stata la scelta giusta e la rifarei altre infinite volte. Ritengo di essere stato molto fortunato ad essere entrato a far parte del gruppo del Dr. Roberto Osellame, che mi ha dato la possibilità di sviluppare diversi progetti e collaborare con diversi gruppi di ricerca e viaggiare per il mondo, facendomi vivere esperienze uniche. In particolare vorrei ringrazie Giacomo, mio relatore, che mi ha coinvolto in numerosi progetti, dato numerosi e preziosi consigli, ma soprattutto ha sempre trovato una parola di conforto nei momenti più giù di tono, che davvero mi alleggeriva il peso della giornata. E comunque anche grazie per tutto il lavoro di revisione della tesi. Vorrei inoltre ringraziare tutte le persone del gruppo degli "Osellami", soprattutto coloro con cui ho collaborato da più vicino, Andrea, mio tutor, e Francesco, che mi hanno aiutato nella stesura e pubblicazione dei miei primi articoli. Mi sono trovato molto bene a lavorare con tutti voi. Un ringraziamento speciale a tutte le persone del buon vecchio Lab Moke, ma anche agli Ephossini che si infiltravano in Moke e a

tutti coloro che passavano sempre da li per un caffè o per un cookies tasting, dove abbiamo condiviso diversi momenti di spensieratezza e ogni tanto anche scambio di idee e consigli. Vi ringrazio per tutti i momenti passati insieme per tutti i femto-aperitivi, le femto-hike, i menini Jesus, i diversi Photball giocati insieme, le partitelle di carte post-pranzo, ma soprattutto le partitelle a biliardino: anche se è durato poco ci ha regalato momenti indimenticabili di gioia e dolore, che anche i colleghi del piano di sotto si ricorderanno ancora. Ci tenevo a dirvi che mi sono divertito molto e mi sono trovato benissimo in questo grande gruppo, e infatti mi dispiace molto lasciarlo dopo questi anni, ma sono sicuro non ci perderemo.

A special thank also to all the people of the QT lab group, in particular to Andrew to give me the possibility to join his beautiful group, but also to Markus and Marcelo to supervise me, and a special thank to all the people that worked with me daily in the lab, but in particular to the people with which I spent time outside the lab, visiting a lot of new places, making a lot of new experience. A special thanks also to Abhishek and Nilesh, to which I spent most of the time during my stay in Australia, for all the trip together (especially in Tasmania) and for the cuisine culture sharing.

Vorrei inoltre ringraziare i miei amici di sempre, coloro che ci sono sempre stati dai banchi delle scuole superiori a oggi, grazie per tutti i weekend passati insieme. Un ringraziamento anche a tutti gli amici del mare e in particolare alla "gang del forto" per le varie serate spensierate passate insieme.

Un immenso grazie anche a Sara che la sua costante presenza in questi anni insieme è stata una delle cose più belle che mi siano capitate, nonostante il lavoro ci tenga fisicamente lontati, a volte con distanze superiori a 16.000 km con +9 ore di fuso orario, (adesso comunque meglio, giusto 10.000 km e -9 di fuso) ogni giorno siamo sempre più vicini. Grazie infatti anche per la pazienza.

Infine vorrei ringraziare la mia famiglia: i miei genitori, che hanno sempre creduto in me e sostenuto in ogni mia scelta e mio fratello imprescindibile compagno di vita. Vi ringrazio per essermi sempre vicino (anche nei luoghi più lontani), il vostro costante supporto è stato fondamentale in questo percorso e lo sarà in quelli a venire.

Bibliography

[1] A. Arriola, S. Gross, N. Jovanovic, N. Charles, P. G. Tuthill, S. M. Olaizola, A. Fuerbach, and M. J. Withford, "Low bend loss waveguides enable compact, efficient 3d photonic chips," *Optics Express*, vol. 21, no. 3, pp. 2978–2986, 2013.

[2] M. A. Nielsen and I. L. Chuang, *Quantum Computation and Quantum Information*. Cambridge: Cambridge University Press, 2002.

[3] D. Deutsch, "Quantum theory, the church–turing principle and the universal quantum computer," *Proceedings of the Royal Society of London. A. Mathematical and Physical Sciences*, vol. 400, no. 1818, pp. 97–117, 1985.

[4] D. P. DiVincenzo, "Quantum gates and circuits," *Proceedings of the Royal Society of London. Series A: Mathematical, Physical and Engineering Sciences*, vol. 454, no. 1969, pp. 261–276, 1998.

[5] K. Mattle, H. Weinfurter, P. G. Kwiat, and A. Zeilinger, "Dense coding in experimental quantum communication," *Physical Review Letters*, vol. 76, no. 25, pp. 4656–4659, 1996.

[6] A. K. Ekert, "Quantum cryptography based on bell's theorem," *Physical Review Letters*, vol. 67, no. 6, pp. 661–663, 1991.

[7] R. Jozsa and N. Linden, "On the role of entanglement in quantum-computational speed-up," *Proceedings of the Royal Society A: Mathematical, Physical and Engineering Sciences*, vol. 459, no. 2036, pp. 2011–2032, 2003.

[8] D. P. DiVincenzo, "The physical implementation of quantum computation," *Fortschritte der Physik: Progress of Physics*, vol. 48, no. 9-11, pp. 771–783, 2000.

[9] J. M. Martinis, "Superconducting phase qubits," *Quantum Information Processing*, vol. 8, no. 2-3, pp. 81–103, 2009.

[10] H. Häffner, C. F. Roos, and R. Blatt, "Quantum computing with trapped ions," *Physics Reports*, vol. 469, no. 4, pp. 155–203, 2008.

[11] D. Loss and D. P. DiVincenzo, "Quantum computation with quantum dots," *Physical Review A*, vol. 57, no. 1, pp. 120–126, 1998.

[12] M. Saffman, T. G. Walker, and K. Mølmer, "Quantum information with rydberg atoms," *Reviews of Modern Physics*, vol. 82, no. 3, pp. 2313–2363, 2010.

[13] R. Hanson, L. P. Kouwenhoven, J. R. Petta, S. Tarucha, and L. M. K. Vandersypen, "Spins in few-electron quantum dots," *Reviews of Modern Physics*, vol. 79, no. 4, pp. 1217–1265, 2007.

[14] E. Knill, R. Laflamme, and G. J. Milburn, "A scheme for efficient quantum computation with linear optics," *Nature*, vol. 409, no. 6816, pp. 46–52, 2001.

[15] P. G. Kwiat, "Quantum information and computation with photons," *Physica Scripta*, vol. T76, p. 115, 1998.

[16] P. G. Kwiat, K. Mattle, H. Weinfurter, A. Zeilinger, A. V. Sergienko, and Y. Shih, "New high-intensity source of polarization-entangled photon pairs," *Physical Review Letters*, vol. 75, no. 24, pp. 4337–4341, 1995.

[17] J. Brendel, N. Gisin, W. Tittel, and H. Zbinden, "Pulsed energy-time entangled twin-photon source for quantum communication," *Physical Review Letters*, vol. 82, no. 12, pp. 2594–2597, 1999.

[18] M. Kues, C. Reimer, P. Roztocki, L. R. Cortés, S. Sciara, B. Wetzel, Y. Zhang, A. Cino, S. T. Chu, B. E. Little, D. J. Moss, L. Caspani, J. Azaña, and R. Morandotti, "On-chip generation of high-dimensional entangled quantum states and their coherent control," *Nature*, vol. 546, no. 7660, pp. 622–626, 2017.

[19] L.-M. Duan and H. J. Kimble, "Scalable photonic quantum computation through cavity-assisted interactions," *Physical Review Letters*, vol. 92, no. 12, p. 127902, 2004.

[20] J. L. O'Brien, A. Furusawa, and J. Vučković, "Photonic quantum technologies," *Nature Photonics*, vol. 3, no. 12, pp. 687–695, 2009.

[21] N. Gisin, G. Ribordy, W. Tittel, and H. Zbinden, "Quantum cryptography," *Reviews of Modern Physics*, vol. 74, no. 1, pp. 145–195, 2002.

[22] M. G. Thompson, A. Politi, J. C. F. Matthews, and J. L. O'Brien, "Integrated waveguide circuits for optical quantum computing," *IET Circuits, Devices & Systems*, vol. 5, no. 2, pp. 94–102, 2011.

[23] J. P. Dowling and G. J. Milburn, "Quantum technology: the second quantum revolution," *Philosophical Transactions of the Royal Society A: Mathematical, Physical and Engineering Sciences*, vol. 361, no. 1809, pp. 1655–1674, 2003.

[24] A. Steane, "Quantum computing," *Reports on Progress in Physics*, vol. 61, no. 2, pp. 117–173, 1998.

[25] N. Gisin and R. Thew, "Quantum communication," *Nature Photonics*, vol. 1, no. 3, pp. 165–171, 2007.

[26] V. Giovannetti, S. Lloyd, and L. Maccone, "Quantum metrology," *Physical Review Letters*, vol. 96, no. 1, p. 010401, 2006.

[27] P. Kok, W. J. Munro, K. Nemoto, T. C. Ralph, J. P. Dowling, and G. J. Milburn, "Linear optical quantum computing with photonic qubits," *Reviews of Modern Physics*, vol. 79, no. 1, pp. 135–174, 2007.

[28] N. Imoto, H. A. Haus, and Y. Yamamoto, "Quantum nondemolition measurement of the photon number via the optical kerr effect," *Physical Review A*, vol. 32, no. 4, pp. 2287–2292, 1985.

[29] G. J. Milburn, "Quantum optical fredkin gate," *Physical Review Letters*, vol. 62, no. 18, pp. 2124–2127, 1989.

[30] R. Raussendorf and H. J. Briegel, "A one-way quantum computer," *Physical Review Letters*, vol. 86, no. 22, pp. 5188–5191, 2001.

[31] S. Bartolucci, P. Birchall, H. Bombín, H. Cable, C. Dawson, M. Gimeno-Segovia, E. Johnston, K. Kieling, N. Nickerson, M. Pant, F. Pastawski, T. Rudolph, and C. Sparrow, "Fusion-based quantum computation," *Nature Communications*, vol. 14, p. 912, 2023.

[32] D. E. Browne and T. Rudolph, "Resource-efficient linear optical quantum computation," *Physical Review Letters*, vol. 95, no. 1, p. 010501, 2005.

[33] D. Gottesman, "An introduction to quantum error correction and fault-tolerant quantum computation," in *Proc. Symp. Appl. Math.*, vol. 68, pp. 13–58, American Mathematical Society, 2010.

[34] A. G. Fowler, M. Mariantoni, J. M. Martinis, and A. N. Cleland, "Surface codes: Towards practical large-scale quantum computation," *Physical Review A*, vol. 86, no. 3, p. 032324, 2012.

[35] D. Litinski, "Blocklet concatenation: Low-overhead fault-tolerant protocols for fusion-based quantum computation," *arXiv preprint arXiv:2506.13619*, 2025.

[36] PsiQuantum team, "A manufacturable platform for photonic quantum computing," *Nature*, 2025.

[37] C. H. Bennett and G. Brassard, "Quantum cryptography: Public key distribution and coin tossing," in *Proceedings of IEEE International Conference on Computers, Systems and Signal Processing*, (Bangalore, India), pp. 175–179, IEEE, 1984.

[38] W. K. Wootters and W. H. Zurek, "A single quantum cannot be cloned," *Nature*, vol. 299, no. 5886, pp. 802–803, 1982.

[39] J. S. Bell, "On the einstein podolsky rosen paradox," *Physics Physique Fizika*, vol. 1, no. 3, pp. 195–200, 1964.

[40] A. Stefanov, N. Gisin, O. Guinnard, L. Guinnard, and H. Zbinden, "Optical quantum random number generator," *Journal of Modern Optics*, vol. 47, no. 4, pp. 595–598, 2000.

[41] M. Herrero-Collantes and J. C. Garcia-Escartin, "Quantum random number generators: a review," *Reviews of Modern Physics*, vol. 89, no. 1, p. 015004, 2017.

[42] C. Gabriel, C. Wittmann, D. Sych, R. Dong, W. Mauerer, U. L. Andersen, C. Marquardt, and G. Leuchs, "A generator for unique quantum random numbers based on vacuum states," *Nature Photonics*, vol. 4, no. 10, pp. 711–715, 2010.

[43] C. H. Bennett, G. Brassard, C. Crépeau, R. Jozsa, A. Peres, and W. K. Wootters, "Teleporting an unknown quantum state via dual classical and einstein–podolsky–rosen channels," *Physical Review Letters*, vol. 70, no. 13, pp. 1895–1899, 1993.

[44] M. Żukowski, A. Zeilinger, M. A. Horne, and A. K. Ekert, ""Event-ready-detectors" Bell experiment via entanglement swapping," *Physical Review Letters*, vol. 71, no. 26, pp. 4287–4290, 1993.

[45] H.-J. Briegel, W. Dür, J. I. Cirac, and P. Zoller, "Quantum repeaters: The role of imperfect local operations in quantum communication," *Physical Review Letters*, vol. 81, no. 26, pp. 5932–5935, 1998.

[46] S. Wehner, D. Elkouss, and R. Hanson, "Quantum internet: A vision for the road ahead," *Science*, vol. 362, no. 6412, p. eaam9288, 2018.

[47] V. Giovannetti, S. Lloyd, and L. Maccone, "Quantum-enhanced measurements: beating the standard quantum limit," *Science*, vol. 306, no. 5700, pp. 1330–1336, 2004.

[48] C. M. Caves, "Quantum-mechanical noise in an interferometer," *Physical Review D*, vol. 23, no. 8, pp. 1693–1708, 1981.

[49] I. A. Walmsley and M. G. Raymer, "Toward quantum-optical technologies for spectroscopy and measurement," *Science*, vol. 307, no. 5716, pp. 1733–1734, 2005.

[50] M. Genovese, "Real applications of quantum imaging," *Journal of Optics*, vol. 18, no. 7, p. 073002, 2016.

[51] A. W. Snyder and J. D. Love, *Optical Waveguide Theory*. London: Chapman and Hall, 1983.

[52] K. Okamoto, *Fundamentals of Optical Waveguides*. Academic Press, 2006.

[53] D. Marcuse, *Theory of Dielectric Optical Waveguides*. Academic Press, 1991.

[54] A. Yariv and P. Yeh, *Photonics: Optical Electronics in Modern Communications*. Oxford University Press, 6th ed., 2006.

[55] B. E. A. Saleh and M. C. Teich, *Fundamentals of Photonics*. Wiley, 1991.

[56] S. M. Eaton, M. L. Ng, J. Bonse, A. Mermillod-Blondin, H. Zhang, A. Rosenfeld, and P. R. Herman, "Low-loss waveguides fabricated in bk7 glass by high repetition rate femtosecond fiber laser," *Applied Optics*, vol. 47, pp. 2098–2102, Apr. 2008.

[57] K. Mittholiya, P. K. Anshad, A. K. Mallik, A. K. Mallik, A. Hegde, A. Bhatnagar, R. Bernard, J. A. Dharmadhikari, D. Mathur, and A. K. Dharmadhikari, "Inscription of waveguides and power splitters in borosilicate glass using ultrashort laser pulses," *Journal of Optics*, vol. 46, pp. 304–310, 2017.

[58] R. R. Gattass and E. Mazur, "Femtosecond laser micromachining in transparent materials," *Nature Photonics*, vol. 2, pp. 219–225, 2008.

[59] A. Ródenas, M. Gu, G. Corrielli, P. Paiè, S. John, A. K. Kar, and R. Osellame, "Three-dimensional femtosecond laser nanolithography of crystals," *Nature Photonics*, vol. 13, pp. 105–109, 2019.

[60] M. Emons, K. Obata, T. Binhammer, A. Ovsianikov, B. N. Chichkov, and U. Morgner, "Two-photon polymerization technique with sub-50 nm resolution by sub-10 fs laser pulses," *Optical Materials Express*, vol. 2, pp. 942–947, 2012.

[61] K. S. Lee, D. Y. Yang, S. H. Park, and R. H. Kim, "Recent developments in the use of two-photon polymerization in precise 2d and 3d microfabrications," *Polymers for Advanced Technologies*, vol. 17, no. 2, pp. 72–82, 2006.

[62] D. Du, X. Liu, G. Korn, J. Squier, and G. Mourou, "Laser-induced breakdown by impact ionization in sio$_2$ with pulse widths from 7 ns to 150 fs," *Applied Physics Letters*, vol. 64, no. 23, pp. 3071–3073, 1994.

[63] K. M. Davis, K. Miura, N. Sugimoto, and K. Hirao, "Writing waveguides in glass with a femtosecond laser," *Optics Letters*, vol. 21, pp. 1729–1731, Nov. 1996.

[64] R. Osellame, G. Cerullo, and R. Ramponi, *Femtosecond Laser Micromachining: Photonic and Microfluidic Devices in Transparent Materials*, vol. 123. Springer Science & Business Media, 2012.

[65] L. V. Keldysh, "Ionization in the field of a strong electromagnetic wave," *Soviet Physics JETP*, vol. 20, no. 5, pp. 1307–1314, 1965.

[66] C. B. Schaffer, A. Brodeur, and E. Mazur, "Laser-induced breakdown and damage in bulk transparent materials induced by tightly focused femtosecond laser pulses," *Measurement Science and Technology*, vol. 12, no. 11, p. 1784, 2001.

[67] M. Shimizu, M. Sakakura, M. Ohnishi, Y. Shimotsuma, T. Nakaya, K. Miura, and K. Hirao, "Mechanism of heat-modification inside a glass after irradiation with high-repetition rate femtosecond laser pulses," *Journal of Applied Physics*, vol. 108, no. 7, p. 073533, 2010.

[68] J. W. Chan, T. Huser, S. Risbud, and D. M. Krol, "Structural changes in fused silica after exposure to focused femtosecond laser pulses," *Opt. Lett.*, vol. 26, no. 21, pp. 1726–1728, 2001.

[69] P. Dekker, M. Ams, G. D. Marshall, D. J. Little, and M. J. Withford, "Annealing dynamics of waveguide bragg gratings: evidence of femtosecond laser induced colour centres," *Opt. Express*, vol. 18, no. 4, pp. 3274–3283, 2010.

[70] S. Kanehira, K. Miura, and K. Hirao, "Ion-exchange in glass using femtosecond laser irradiation," *Applied Physics Letters*, vol. 93, 2008.

[71] P. Paiè, F. Bragheri, R. M. Vazquez, and R. Osellame, "Straightforward 3d hydrodynamic focusing in femtosecond laser fabricated microfluidic channels," *Lab on a Chip*, vol. 14, no. 11, pp. 1826–1833, 2014.

[72] A. Ciriolo, R. M. Vázquez, V. Tosa, A. Frezzotti, G. Crippa, M. Devetta, D. Faccialá, F. Frassetto, L. Poletto, A. Pusala, *et al.*, "High-order harmonic generation in a microfluidic glass device," *Journal of Physics: Photonics*, vol. 2, no. 2, p. 024005, 2020.

[73] S. Juodkazis, K. Nishimura, S. Tanaka, H. Misawa, E. G. Gamaly, B. Luther-Davies, L. Hallo, P. Nicolai, and V. T. Tikhonchuk, "Laser-induced microexplosion confined in the bulk of a sapphire crystal: Evidence of multimegabar pressures," *Phys. Rev. Lett.*, vol. 96, p. 166101, 2006.

[74] E. N. Glezer, M. Milosavljevic, L. Huang, R. J. Finlay, T.-H. Her, J. P. Callan, and E. Mazur, "Three-dimensional optical storage inside transparent materials," *Opt. Lett.*, vol. 21, no. 24, pp. 2023–2025, 1996.

[75] S. Juodkazis, S. Matsuo, H. Misawa, V. Mizeikis, A. Marcinkevicius, H. B. Sun, Y. Tokuda, M. Takahashi, T. Yoko, and J. Nishii, "Application of femtosecond laser pulses for microfabrication of transparent media," *Applied Surface Science*, vol. 197–198, pp. 705–709, 2002.

[76] S. M. Eaton, H. Zhang, P. R. Herman, F. Yoshino, L. Shah, J. Bovatsek, and A. Y. Arai, "Heat accumulation effects in femtosecond laser-written waveguides with variable repetition rate," *Optics Express*, vol. 13, no. 12, pp. 4708–4716, 2005.

[77] S. M. Eaton, G. Cerullo, and R. Osellame, "Fundamentals of femtosecond laser modification of bulk dielectrics," in *Femtosecond Laser Micromachining*, pp. 3–18, Berlin, Heidelberg: Springer Berlin Heidelberg, 2012.

[78] R. Osellame, N. Chiodo, G. D. Valle, S. Taccheo, R. Ramponi, G. Cerullo, A. Killi, U. Morgner, M. Lederer, and D. Kopf, "Optical waveguide writing with a diode-pumped femtosecond oscillator," *Optics Letters*, vol. 29, no. 16, pp. 1900–1902, 2004.

[79] J. Guan, X. Liu, and M. J. Booth, "Ultrafast laser writing quill effect in low loss waveguide fabrication regime," *Optics Express*, vol. 26, pp. 30716–30723, Nov. 2018.

[80] M. Pont, R. Albiero, S. E. Thomas, N. Spagnolo, F. Ceccarelli, G. Corrielli, A. Brieussel, N. Somaschi, H. Huet, and et al., "Quantifying *n*-photon indistinguishability with a cyclic integrated interferometer," *Physical Review X*, vol. 12, no. 3, p. 031033, 2022.

[81] A. Crespi, R. Osellame, R. Ramponi, M. Bentivegna, F. Flamini, N. Spagnolo, N. Viggianiello, L. Innocenti, P. Mataloni, and F. Sciarrino, "Suppression law of quantum states in a 3d photonic fast fourier transform chip," *Nature Communications*, vol. 7, p. 10469, 2016.

[82] M. Gräfe, R. Heilmann, A. Perez-Leija, R. Keil, F. Dreisow, M. Heinrich, H. Moya-Cessa, S. Nolte, D. N. Christodoulides, and A. Szameit, "On-chip generation of high-order single-photon w-states," *Nature Photonics*, vol. 8, no. 10, pp. 791–795, 2014.

[83] K. Poulios, R. Keil, D. Fry, J. D. Meinecke, J. C. Matthews, A. Politi, M. Lobino, M. Gräfe, M. Heinrich, S. Nolte, and et al., "Quantum walks of correlated photon pairs in two-dimensional waveguide arrays," *Physical Review Letters*, vol. 112, no. 14, p. 143604, 2014.

[84] F. Hoch, S. Piacentini, T. Giordani, Z.-N. Tian, M. Iuliano, C. Esposito, A. Camillini, G. Carvacho, F. Ceccarelli, N. Spagnolo, A. Crespi, F. Sciarrino, and R. Osellame, "Reconfigurable continuously-coupled 3d photonic circuit for boson sampling experiments," *npj Quantum Information*, vol. 8, no. 55, 2022.

[85] L. Sansoni, F. Sciarrino, G. Vallone, P. Mataloni, A. Crespi, R. Ramponi, and R. Osellame, "Polarization entangled state measurement on a chip," *Physical Review Letters*, vol. 105, no. 20, p. 200503, 2010.

[86] G. Corrielli, A. Crespi, R. Geremia, R. Ramponi, L. Sansoni, A. Santinelli, P. Mataloni, F. Sciarrino, and R. Osellame, "Rotated waveplates in integrated waveguide optics," *Nature Communications*, vol. 5, no. 1, pp. 1–6, 2014.

[87] A. Crespi, R. Ramponi, R. Osellame, L. Sansoni, I. Bongioanni, F. Sciarrino, G. Vallone, and P. Mataloni, "Integrated photonic quantum gates for polarization qubits," *Nature Communications*, vol. 2, no. 1, pp. 1–6, 2011.

[88] G. Corrielli, S. Atzeni, S. Piacentini, I. Pitsios, A. Crespi, and R. Osellame, "Symmetric polarization-insensitive directional couplers fabricated by femtosecond laser writing," *Optics Express*, vol. 26, no. 12, pp. 15101–15109, 2018.

[89] A. M. Streltsov and N. F. Borrelli, "Fabrication and analysis of a directional coupler written in glass by nanojoule femtosecond laser pulses," *Optics Letters*, vol. 26, no. 1, pp. 42–43, 2001.

[90] G. Gualandi, "Femtosecond-laser-written wavelength division multiplexer for quantum photonics applications," Master's thesis, Politecnico di Milano, 2021. Tesi di Laurea Magistrale, POLITesi.

[91] W.-J. Chen, S. M. Eaton, H. Zhang, and P. R. Herman, "Broadband directional couplers fabricated in bulk glass with high repetition rate femtosecond laser pulses," *Optics Express*, vol. 16, pp. 11470–11480, Jul 2008.

[92] L. A. Fernandes, J. R. Grenier, P. R. Herman, J. S. Aitchison, and P. V. S. Marques, "Femtosecond laser fabrication of birefringent directional couplers as polarization beam splitters in fused silica," *Optics Express*, vol. 19, no. 13, pp. 11992–11999, 2011.

[93] K. Minoshima, A. M. Kowalevicz, E. P. Ippen, and J. G. Fujimoto, "Fabrication of coupled mode photonic devices in glass by nonlinear femtosecond laser materials processing," *Optics Express*, vol. 10, pp. 645–652, July 2002.

[94] A. Crespi, Y. Gu, B. Ngamsom, H. J. W. M. Hoekstra, C. Dongre, M. Pollnau, R. Ramponi, H. H. van den Vlekkert, P. Watts, G. Cerullo, and R. Osellame, "Three-dimensional mach-zehnder interferometer in a microfluidic chip for spatially-resolved label-free detection," *Lab on a Chip*, vol. 10, pp. 1167–1173, 2010.

[95] A. Crespi, R. Osellame, R. Ramponi, D. J. Brod, E. F. Galvao, N. Spagnolo, C. Vitelli, E. Maiorino, P. Mataloni, and F. Sciarrino, "Integrated multimode interferometers with arbitrary designs for photonic boson sampling," *Nature Photonics*, vol. 7, pp. 545–549, May 2013.

[96] M. C. Tichy, M. Tiersch, F. de Melo, F. Mintert, and A. Buchleitner, "Zero-transmission law for multiport beam splitters," *Physical Review Letters*, vol. 104, p. 220405, June 2010.

[97] F. Flamini, L. Magrini, A. S. Rab, N. Spagnolo, V. D'Ambrosio, P. Mataloni, F. Sciarrino, T. Zandrini, A. Crespi, R. Ramponi, and R. Osellame, "Thermally reconfigurable quantum photonic circuits at telecom wavelength by femtosecond laser micromachining," *Light: Science & Applications*, vol. 4, p. e354, 2015.

[98] F. Ceccarelli, S. Atzeni, C. Pentangelo, F. Pellegatta, A. Crespi, and R. Osellame, "Low power reconfigurability and reduced crosstalk in integrated photonic circuits fabricated by femtosecond laser micromachining," *Laser & Photonics Reviews*, vol. 14, no. 10, p. 2000024, 2020.

[99] G. Li, K. A. Winick, A. A. Said, M. Dugan, and P. Bado, "Waveguide electro-optic modulator in fused silica fabricated by femtosecond laser direct writing and thermal poling," *Optics Letters*, vol. 31, no. 6, pp. 739–741, 2006.

[100] P. C. Humphreys, B. J. Metcalf, J. B. Spring, M. Moore, P. S. Salter, M. J. Booth, W. S. Kolthammer, and I. A. Walmsley, "Strain-optic active control for quantum integrated photonics," *Optics Express*, vol. 22, no. 18, pp. 21719–21726, 2014.

[101] M. Spagnolo, R. Motta, R. Memeo, F. Pellegatta, A. Crespi, and R. Osellame, "Resonant opto-mechanical modulators and switches by femtosecond laser micromachining," *Optics Express*, vol. 28, no. 16, pp. 23133–23142, 2020.

[102] Z. Chaboyer, T. Meany, L. G. Helt, M. J. Withford, and M. J. Steel, "Tunable quantum interference in a 3d integrated circuit," *Scientific Reports*, vol. 5, p. 9601, 2015.

[103] E. Polino, M. Riva, M. Valeri, R. Silvestri, G. Corrielli, A. Crespi, N. Spagnolo, R. Osellame, and F. Sciarrino, "Experimental multiphase estimation on a chip," *Optica*, vol. 6, no. 3, pp. 288–295, 2019.

[104] I. V. Dyakonov, I. A. Pogorelov, I. B. Bobrov, A. A. Kalinkin, S. S. Straupe, S. P. Kulik, P. V. Dyakonov, and S. A. Evlashin, "Reconfigurable photonics on a glass chip," *Physical Review Applied*, vol. 10, no. 4, p. 044048, 2018.

[105] J. W. Silverstone, D. Bonneau, J. L. O'Brien, and M. G. Thompson, "Silicon quantum photonics," *IEEE Journal of Selected Topics in Quantum Electronics*, vol. 22, no. 6, pp. 390–402, 2016.

[106] J. Wang, F. Sciarrino, A. Laing, and M. G. Thompson, "Integrated photonic quantum technologies," *Nature Photonics*, vol. 14, pp. 273–284, 2020.

[107] PsiQuantum team, "A manufacturable platform for photonic quantum computing," *Nature*, vol. 641, pp. 876–883, Feb. 2025.

[108] A. Politi, M. J. Cryan, J. G. Rarity, S. Yu, and J. L. O'Brien, "Silica-on-silicon waveguide quantum circuits," *Science*, vol. 320, no. 5876, pp. 646–649, 2008.

[109] J. B. Spring, P. L. Mennea, B. J. Metcalf, P. C. Humphreys, J. C. Gates, H. L. Rogers, C. Söller, B. J. Smith, W. S. Kolthammer, P. G. R. Smith, and I. A. Walmsley, "Chip-based array of near-identical, pure, heralded single-photon sources," *Optica*, vol. 4, no. 1, pp. 90–96, 2017.

[110] S. Bidnyk, K. Yadav, S.-H. Liu, and A. Balakrishnan, "Enabling advanced photonic architectures using state-of-the-art silica-on-silicon planar lightwave circuit platform," in *Proceedings of SPIE OPTO, Integrated Optics: Devices, Materials, and Technologies XXVII*, vol. 12424, (San Francisco, California, United States), p. 1242406, Mar. 2023. Published: 17 March 2023.

[111] A. e. a. Melloni, "The role of index contrast in dielectric optical waveguides," *International Journal of Materials and Product Technology*, vol. 34, no. 4, pp. 421–437, 2009.

[112] N. Hoppe, A. V. Gladyshev, A. A. Danner, W. Freude, and C. Koos, "Ultra-efficient silicon-on-insulator grating couplers with backside metal mirrors," *IEEE Journal of Selected Topics in Quantum Electronics*, vol. 26, no. 2, pp. 1–8, 2019.

[113] Y. A. Vlasov and S. J. McNab, "Losses in single-mode silicon-on-insulator strip waveguides and bends," *Optics Express*, vol. 12, no. 8, pp. 1622–1631, 2004.

[114] G. T. Reed, G. Mashanovich, F. Y. Gardes, and D. J. Thomson, "Silicon optical modulators," *Nature Photonics*, vol. 4, pp. 518–526, 2010.

[115] X. Qiang, X. Zhou, J. Wang, C. M. Wilkes, T. Loke, S. O'Gara, J. C. Matthews, A. Laing, J. L. O'Brien, M. G. Thompson, and J. B. Wang, "Large-scale silicon quantum photonics implementing arbitrary two-qubit processing," *Nature Photonics*, vol. 12, no. 9, pp. 534–539, 2018.

[116] J. Wang, S. Paesani, Y. Ding, R. Santagati, P. Skrzypczyk, A. Salavrakos, J. Tura, R. Augusiak, L. Mancinska, D. Bacco, D. Bonneau, J. W. Silverstone, Q. Gong, A. Acín, K. Rottwitt, L. K. Oxenløwe, J. L. O'Brien, A. Laing, and M. G. Thompson, "Multidimensional quantum entanglement with large-scale integrated optics," *Science*, vol. 360, no. 6386, pp. 285–291, 2018.

[117] X. Zheng, N. Calandri, X. Zhu, J. A. Stern, X. Xie, S. G. Liao, H. Zhou, A. E. Dane, D. Zhu, D. E. Leaird, A. M. Weiner, K. Berggren, C. Sorace-Agaskar, and D. Englund, "Heterogeneously integrated, superconducting silicon-photonic platform for measurement-device-independent quantum key distribution," *Advanced Photonics*, vol. 3, no. 5, p. 056002, 2021.

[118] D. J. Moss, R. Morandotti, A. L. Gaeta, and M. Lipson, "New cmos-compatible platforms based on silicon nitride and hydex for nonlinear optics," *Nature Photonics*, vol. 7, no. 8, pp. 597–607, 2013.

[119] C. Lacava, S. Stankovic, A. Z. Khokhar, T. D. Bucio, F. Y. Gardes, G. T. Reed, D. J. Richardson, and P. Petropoulos, "Si-rich silicon nitride for nonlinear signal processing applications," *Scientific Reports*, vol. 7, no. 1, p. 22, 2017.

[120] Y. Zhao, Y. Okawachi, B. Y. Kim, C. Joshi, J. Kahl, and J. B. Spring, "Microresonator based discrete- and continuous-variable quantum sources on silicon-nitride," *Quantum*, vol. 2, p. QM4B.3, 2020.

[121] S. Gyger, J. Zichi, L. Schweickert, A. W. Elshaari, S. Steinhauer, S. F. C. da Silva, A. Rastelli, V. Zwiller, and C. Errando-Herranz, "Reconfigurable photonics with on-chip single-photon detectors," *Nature Communications*, vol. 12, no. 1, p. 1408, 2021.

[122] C. Schuck, W. H. P. Pernice, and H. X. Tang, "Nbtin superconducting nanowire detectors for visible and telecom wavelengths single photon counting on si_3n_4 photonic circuits," *Applied Physics Letters*, vol. 102, no. 5, p. 051101, 2013.

[123] Y. Hu, D. Zhu, S. Lu, X. Zhu, Y. Song, D. Renaud, D. Assumpcao, R. Cheng, C. J. Xin, M. Yeh, H. Warner, X. Guo, A. Shams-Ansari, D. R. Barton, N. Sinclair, and M. Lončar, "Integrated electro-optics on thin-film lithium niobate," *Nat. Rev. Phys.*, vol. 7, no. 5, pp. 237–254, 2025.

[124] B. Desiatov, A. Shams-Ansari, M. Zhang, C. Wang, and M. Lončar, "Ultra-low-loss integrated visible photonics using thin-film lithium niobate," *Optica*, vol. 6, no. 3, pp. 380–384, 2019.

[125] K. Luke, P. Kharel, C. Reimer, L. He, M. Lončar, and M. Zhang, "Wafer-scale low-loss lithium niobate photonic integrated circuits," *Opt. Express*, vol. 28, no. 17, pp. 24452–24458, 2020.

[126] J. Liu, J. Duan, P. Zhu, G. Xia, Q. Hong, K. Zhang, Z. Zhu, S. Qin, and P. Xu, "Modal phase-matching in thin-film lithium niobate waveguides for efficient generation of entangled photon pairs," *Opt. Express*, vol. 32, no. 23, pp. 40629–40639, 2024.

[127] F. Ceccarelli, S. Atzeni, A. Prencipe, R. Farinaro, and R. Osellame, "Thermal phase shifters for femtosecond laser written photonic integrated circuits," *Journal of Lightwave Technology*, vol. 37, no. 17, pp. 4275–4281, 2019.

[128] K. Chopra, L. Bobb, and M. Francombe, "Electrical resistivity of thin single-crystal gold films," *Journal of Applied Physics*, vol. 34, no. 6, pp. 1699–1702, 1963.

[129] D. Marcuse, "Curvature loss formula for optical fibers," *Journal of the Optical Society of America*, vol. 66, no. 3, pp. 216–220, 1976.

[130] W. A. Gambling, H. Matsumura, and C. M. Ragdale, "Curvature and microbending losses in single-mode optical fibres," *Optical and Quantum Electronics*, vol. 11, no. 1, pp. 43–59, 1979.

[131] A. Peri, G. Gualandi, T. Bertapelle, M. Sabatini, G. Corrielli, Y. Piétri, D. G. Marangon, G. Vallone, P. Villoresi, R. Osellame, and M. Avesani, "High-performance heterodyne receiver for quantum information processing in a laser written integrated photonic platform," *arXiv preprint arXiv:2506.08924*, 2025. Published 10 June 2025.

[132] R. Sax, A. Boaron, G. Boso, S. Atzeni, A. Crespi, F. Grünenfelder, D. Rusca, A. Al-Saadi, D. Bronzi, S. Kupijai, H. Rhee, R. Osellame, and H. Zbinden, "High-speed integrated qkd system," *Photonics Research*, vol. 11, no. 6, pp. 1007–1014, 2023.

[133] A. Boaron, B. Korzh, R. Houlmann, G. Boso, D. Rusca, S. Gray, M.-J. Li, D. Nolan, A. Martin, and H. Zbinden, "Simple 2.5 ghz time-bin quantum key distribution," *Applied Physics Letters*, vol. 112, no. 17, p. 171108, 2018.

[134] D. Rusca, A. Boaron, M. Curty, A. Martin, and H. Zbinden, "Security proof for a simplified bb84-like qkd protocol," *Physical Review A*, vol. 98, no. 5, p. 052336, 2018.

[135] L. A. Fernandes, R. D. R. B. Layman, J. R. Grenier, and P. R. Herman, "Stress induced birefringence tuning in femtosecond laser fabricated waveguides in fused silica," *Optics Express*, vol. 20, no. 22, pp. 24103–24114, 2012.

[136] V. R. Bhardwaj, E. Simova, P. P. Rajeev, C. Hnatovsky, R. S. Taylor, D. M. Rayner, and P. B. Corkum, "Stress in femtosecond-laser-written waveguides in fused silica," *J. Opt. Soc. Am. B*, vol. 21, no. 10, pp. 191–198, 2004.

[137] B. McMillen, P. R. Herman, G. A. Torchia, P. Kazansky, and W. Watanabe, "Femtosecond laser direct-write waveplates based on stress engineered retardance," *Optical Materials Express*, vol. 6, no. 12, pp. 3865–3876, 2016.

[138] F. Raffaelli, L. S. Costanzo, S. Donati, P. Villoresi, and R. Osellame, "A homodyne detector integrated onto a photonic chip for measuring quantum states and generating random numbers," *Quantum Sci. Technol.*, vol. 3, no. 2, p. 025003, 2018.

[139] G. Zhang, Q. Zhang, J. Wang, X. Wang, Y. Hu, H. Chen, Z. Zhang, H. Li, S. Yu, and M. Li, "An integrated silicon photonic chip platform for continuous-variable quantum key distribution," *Nat. Photonics*, vol. 13, no. 12, pp. 839–842, 2019.

[140] A. A. Hajomer, F. Raffaelli, M. Avesani, R. Osellame, and P. Villoresi, "Continuous-variable quantum key distribution at 10 gbaud using an integrated photonic-electronic receiver," *Optica*, vol. 11, no. 9, pp. 1197–1204, 2024.

[141] Y. Bian, X. Chen, L. Zhang, Q. Wang, and J. Liu, "Continuous-variable quantum key distribution over 28.6 km fiber with an integrated silicon photonic receiver chip," *Appl. Phys. Lett.*, vol. 124, no. 17, p. 174001, 2024.

[142] S.-H. Jeong and K. Morito, "Novel optical 90° hybrid consisting of a paired interference based 2 × 4 mmi coupler, a phase shifter and a 2 × 2 mmi coupler," *J. Lightwave Technol.*, vol. 28, no. 9, pp. 1323–1331, 2010.

[143] J. Yu, H. Li, X. Luo, and Y. Zhang, "High-performance 90° hybrids based on mmi couplers in si_3n_4 technology," *Opt. Commun.*, vol. 465, p. 125620, 2020.

[144] Y. Piétri, A. Peri, G. Gualandi, R. Osellame, P. Villoresi, and M. Avesani, "Experimental demonstration of continuous-variable quantum key distribution with a silicon photonics integrated receiver," *Optica Quantum*, vol. 2, no. 6, pp. 428–437, 2024.

[145] S. Piacentini, T. Vogl, G. Corrielli, P. K. Lam, and R. Osellame, "Space qualification of ultrafast laser-written integrated waveguide optics," *Laser & Photonics Reviews*, vol. 15, no. 2, p. 2000167, 2020.

[146] G. Gualandi, S. Atzeni, M. Gardina, A. Caime, G. Corrielli, I. Labanca, A. Gulinatti, I. Rech, R. Osellame, G. Acconcia, and F. Ceccarelli, "Laser-written reconfigurable photonic integrated circuit directly coupled to a single-photon avalanche diode array," *Light: Science & Applications*, vol. 14, no. 199, 2025.

[147] R. Albiero, C. Pentangelo, M. Gardina, S. Atzeni, F. Ceccarelli, and R. Osellame, "Toward higher integration density in femtosecond-laser-written programmable photonic circuits," *Micromachines*, vol. 13, no. 7, p. 1145, 2022.

[148] T. Gerrits, A. Migdall, J. C. Bienfang, J. Lehman, S. W. Nam, J. Splett, I. Vayshenker, and J. Wang, "Calibration of free-space and fiber-coupled single-photon detectors," *Metrologia*, vol. 57, no. 1, p. 015002, 2020.

[149] F. Ceccarelli, M. Ghioni, I. Rech, and A. Gulinatti, "Gigacount/second photon detection module based on an 8 × 8 single-photon avalanche diode array," *IEEE Photonics Technology Letters*, vol. 28, no. 9, pp. 1002–1005, 2016.

[150] M. A. Wolff, F. Beutel, J. Schütte, H. Gehring, M. Häußler, W. H. P. Pernice, and C. Schuck, "Broadband waveguide-integrated superconducting single-photon detectors with high system detection efficiency," *Applied Physics Letters*, vol. 118, p. 154004, 2021.

[151] J. Zhang, H. Xu, G. Zhang, Y. Chen, H. Wang, K. H. Tan, S. Wicaksono, C. Sun, Q. Kong, C. Wang, C. C. W. Lim, S. F. Yoon, and X. Gong, "Hybrid and heterogeneous photonic integrated near-infrared ingaas/inalas single-photon avalanche diode," *Quantum Science and Technology*, vol. 8, p. 025009, 2023.

[152] H. Wang, Y. Shi, Y. Zuo, Y. Yu, L. Lei, X. Zhang, and Z. Qian, "High-performance waveguide coupled germanium-on-silicon single-photon avalanche diode with independently controllable absorption and multiplication," *Nanophotonics*, vol. 12, pp. 705–714, 2023.

[153] A. Govdeli, J. N. Straguzzi, Z. Yong, Y. Lin, X. Luo, H. Chua, G.-Q. Lo, W. D. Sacher, and J. K. S. Poon, "Room-temperature waveguide-coupled silicon single-photon avalanche diodes," *npj Nanophotonics*, vol. 1, p. 2, 2024.

[154] F. Acerbi, M. Bernard, B. Goll, A. Gola, H. Zimmermann, G. Pucker, and M. Ghulinyan, "Monolithically integrated sion photonic circuit and silicon single-photon detectors for nir-range operation," *Journal of Lightwave Technology*, vol. 42, pp. 2831–2841, 2023.

[155] A. Trenti, M. Achleitner, F. Prawits, B. Schrenk, H. Conradi, M. Kleinert, A. Incoronato, F. Zanetto, F. Zappa, I. D. Luch, O. Cirkinoglu, X. Leijtens, A. Bonardi, C. Bruynsteen, X. Yin, C. Kiessler, H. Herrmann, C. Silberhorn, M. Bozzio, P. Walther, H. C. Thiel, G. Weihs,

and H. Hübel, "On-chip quantum communication devices," *Journal of Lightwave Technology*, vol. 40, no. 23, pp. 7485–7497, 2022.

[156] U. Sinha, C. Couteau, T. Jennewein, R. Laflamme, and G. Weihs, "Ruling out multi-order interference in quantum mechanics," *Science*, vol. 329, no. 5990, pp. 418–421, 2010.

[157] T. Kauten, R. Keil, T. Kaufmann, B. Pressl, C. Brukner, and G. Weihs, "Obtaining tight bounds on higher-order interferences with a 5-path interferometer," *New Journal of Physics*, vol. 19, no. 3, p. 033017, 2017.

[158] T. Vogl, Z. Tian, Y. Quek, A. Sharma, H. Vora, I. Aharonovich, M. Tomamichel, E. Curty, and S. Castelletto, "Bounding higher-order interference in a two-path interferometer," *Physical Review Research*, vol. 3, no. 4, p. 043029, 2021.

[159] N. Ahmadi, S. Schwertfeger, P. Werner, L. Wiese, J. Lester, E. D. Ros, J. Krause, S. Ritter, M. Abasifard, C. Cholsuk, R. G. Krämer, S. Atzeni, M. Gündoğan, S. Sachidananda, D. Pardo, S. Nolte, A. Lohrmann, A. Ling, J. Bartholomäus, G. Corrielli, M. Krutzik, and T. Vogl, "QUICK^3 – design of a satellite-based quantum light source for quantum communication and extended physical theory tests in space," *Advanced Quantum Technologies*, vol. 7, no. 4, p. 2300343, 2024.

[160] M. Born, "Zur quantenmechanik der stoßvorgänge," *Zeitschrift für Physik*, vol. 37, no. 12, pp. 863–867, 1926.

[161] R. D. Sorkin, "Quantum mechanics as quantum measure theory," *Modern Physics Letters A*, vol. 9, no. 33, pp. 3119–3127, 1994.

[162] H. Barnum, M. P. Müller, and C. Ududec, "Higher-order interference and single-system postulates characterizing quantum theory," *New Journal of Physics*, vol. 16, p. 123029, 2014.

[163] S. Gstir, E. Chan, T. Eichelkraut, A. Szameit, R. Keil, and G. Weihs, "Towards probing for hypercomplex quantum mechanics in a waveguide interferometer," *New Journal of Physics*, vol. 23, no. 6, p. 063019, 2021.

[164] D. K. Park, O. Moussa, and R. Laflamme, "Three path interference using nuclear magnetic resonance: a test of the consistency of born's rule," *New Journal of Physics*, vol. 14, p. 113025, 2012.

[165] S. Bartolucci, P. M. Birchall, M. Gimeno-Segovia, E. Johnston, K. Kieling, M. Pant, T. Rudolph, J. Smith, C. Sparrow, and M. D. Vidrighin, "Creation of entangled photonic states using linear optics," *arXiv preprint arXiv:2101.09310*, 2021.

[166] H. Bombin, I. H. Kim, D. Litinski, N. Nickerson, M. Pant, F. Pastawski, S. Roberts, and T. Rudolph, "Interleaving: Modular architectures for fault-tolerant photonic quantum computing," *arXiv preprint arXiv:2103.08612*, 2021.

[167] S.-K. Liao, W.-Q. Cai, W.-Y. Liu, L. Zhang, Y. Li, J.-G. Ren, J. Yin, Q. Shen, Y. Cao, Z.-P. Li, F.-Z. Li, X.-W. Chen, L.-H. Sun, J.-J. Jia, J.-C. Wu, X.-J. Jiang, J.-F. Wang, Y.-M. Huang, Q. Wang, Y.-L. Zhou, L. Deng, T. Xi, L. Ma, T. Hu, Q. Zhang, Y.-A. Chen, C.-Y. Lu, R. Shu, C.-Z. Peng, J.-Y. Wang, and J.-W. Pan, "Satellite-to-ground quantum key distribution," *Physical Review Letters*, vol. 120, no. 3, p. 030501, 2018.

[168] X.-M. Hu, Y. Guo, B.-H. Liu, Y.-F. Huang, C.-F. Li, and G.-C. Guo, "Beating the channel capacity limit for superdense coding with entangled ququarts," *Science Advances*, vol. 4, no. 10, p. eaat9304, 2018.

[169] V. Giovannetti, S. Lloyd, and L. Maccone, "Advances in quantum metrology," *Nature Photonics*, vol. 5, no. 4, pp. 222–229, 2011.

[170] C. K. Hong, Z. Y. Ou, and L. Mandel, "Measurement of subpicosecond time intervals between two photons by interference," *Physical Review Letters*, vol. 59, no. 18, pp. 2044–2046, 1987.

[171] I. Forbes, F. Ghafari, E. C. R. Deacon, S. P. Singh, E. Lavie, P. Yard, R. D. Shaw, A. Laing, and N. Tischler, "Heralded generation of entanglement with photons," *arXiv preprint arXiv:2502.00982*, 2025.

[172] R. D. Shaw, A. E. Jones, P. Yard, and A. Laing, "Errors in heralded circuits for linear optical entanglement generation," *arXiv preprint arXiv:2305.08452*, 2023.

[173] Q. Zhang, X.-H. Bao, C.-Y. Lu, X.-Q. Zhou, T. Yang, T. Rudolph, and J.-W. Pan, "Demonstration of a scheme for the generation of "event-ready" entangled photon pairs from a single-photon source," *Physical Review A*, vol. 77, no. 6, p. 062316, 2008.

[174] J. Carolan, C. Harrold, C. Sparrow, E. Martin-Lopez, N. J. Russell, J. W. Silverstone, P. J. Shadbolt, N. Matsuda, M. Oguma, M. Itoh, G. D. Marshall, M. G. Thompson, J. C. F. Matthews, T. Hashimoto, J. L. O'Brien, and M. A. Broome, "Universal linear optics," *Science*, vol. 349, no. 6249, pp. 711–716, 2015.

[175] S. A. Fldzhyan, N. N. Skryabin, M. A. Dryazgov, S. A. Zhuravitskii, A. S. Argenchiev, I. V. Kondratyev, L. A. Tsoma, K. I. Okhlopkov, M. Y. Saygin, S. P. Kulik, and S. S. Straupe, "Compact linear-optical schemes for heralded bell state generation," *arXiv preprint arXiv:2307.XXXXX*, 2023.

[176] S. Paesani, M. Borghi, R. Harris, A. W. Branczyk, M. D. Laing, M. G. Thompson, and A. Laing, "Generation and sampling of quantum states of light in a silicon chip," *Nature Physics*, vol. 15, pp. 925–929, 2019.

[177] H. Cao, L. M. Hansen, F. Giorgino, L. Carosini, P. Zahalka, F. Zilk, J. C. Loredo, and P. Walther, "Photonic source of heralded greenberger–horne–zeilinger states," *Physical Review Letters*, vol. 132, no. 13, p. 130604, 2024.

[178] D. F. V. James, P. G. Kwiat, W. J. Munro, and A. G. White, "Measurement of qubits," *Physical Review A*, vol. 64, no. 5, p. 052312, 2001.

[179] D. H. Geuzebroek and A. Driessen, "Ring-resonator-based wavelength filters," in *Wavelength Filters in Fibre Optics* (L. Cheng, ed.), vol. 123 of *Springer Series in Optical Sciences*, pp. 341–379, Springer, 2006.

[180] J. Xu, Y. Zhang, X. Guo, *et al.*, "High-performance integrated optical filters based on ring resonators," *Optics Letters*, vol. 46, no. 22, pp. 5575–5578, 2021.

[181] Y. Yuan, Y. Peng, W. V. Sorin, *et al.*, "Chip-scale programmable optical filters enabled by ring resonators," *Nature Communications*, vol. 15, p. 950, 2024.

[182] J. Hong, F. Qiu, X. Cheng, *et al.*, "Refractive index sensing using integrated ring resonators," *Scientific Reports*, vol. 7, p. 4682, 2017.

[183] A. K. Sarkaleh, B. V. Lahijani, H. Saberkari, and A. Esmaeeli, "Application of optical ring resonators in medical sensing," *Journal of Medical Signals and Sensors*, vol. 7, no. 3, pp. 185–191, 2017.

[184] Y. H. Lai, M. G. Suh, Y. K. Lu, *et al.*, "Earth-rotation sensing using optical microcomb ring resonators," *Nature Photonics*, vol. 14, pp. 345–349, 2020.

[185] P. P. Khial, A. D. White, and A. Hajimiri, "Nanophotonic optical gyroscope with a ring resonator," *Nature Photonics*, vol. 12, pp. 671–675, 2018.

[186] P. Tritschler, C. Schweikert, R. H. Klenk, *et al.*, "Nonlinear dynamics in integrated optical ring resonators," *Physical Review Letters*, vol. 134, no. 12, p. 123802, 2025.

[187] P. Tritschler, T. Ohms, C. Schweikert, *et al.*, "Advanced nonlinear effects in optical ring resonators," *arXiv preprint arXiv:2502.16278*, 2025.

[188] A. Yariv, "Universal relations for coupling of optical power between microresonators and dielectric waveguides," *Electronics Letters*, vol. 36, no. 4, pp. 321–322, 2000.

[189] Q. Yang, "Finesse of ring resonators," *AIP Advances*, vol. 13, no. 8, p. 085225, 2023.

[190] C. V. Cushman, B. A. Sturgell, A. C. Martin, B. M. Lunt, N. J. Smith, and M. R. Linford, "Eagle xg® glass, optical constants from 230 to 1690 nm (0.73 – 5.39 ev) by spectroscopic ellipsometry," *Surface Science Spectra*, vol. 23, no. 1, pp. 55–60, 2016.